Plasma Physics Reports, Vol. 30, No. 2, 2004, pp. 111–120. Translated from Fizika Plazmy, Vol. 30, No. 2, 2004, pp. 129–138.

PLASMA DIAGNOSTICS

Microwave Measurements of the Time Evolution of Electron Density in the T-11M Tokamak

V. G. Petrov, A. A. Petrov, A. Yu. Malyshev, V. K. Markov, and A. V. Babarykin

Troitsk Institute for Innovation and Fusion Research, Troitsk, Moscow oblast, 142190 Russia

Received July 24, 2003

Abstract—Unambiguous diagnostics intended for measuring the time behavior of the electron density and monitoring the line-averaged plasma density in the T-11M tokamak are described. The time behavior of the plasma density in the T-11M tokamak is measured by a multichannel phase-jump-free microwave polarization interferometer based on the Cotton–Mouton effect. After increasing the number of simultaneously operating interferometer channels and enhancing the sensitivity of measurements, it became possible to measure the time evolution of the plasma density profile in the T-11M tokamak. The first results from such measurements in various operating regimes of the T-11M tokamak are presented. The measurement and data processing techniques are described, the measurement errors are analyzed, and the results obtained are discussed. We propose using a pulsed time-of-flight refractometer to monitor the average plasma density in the T-11M tokamak. The refractometer emits nanosecond microwave probing pulses with a carrier frequency that is higher than the plasma frequency and, thus, operates in the transmission mode. A version of the instrument has been developed with a carrier frequency of 140 GHz, which allows one to measure the average density in regimes with a nominal T-11M plasma density of $(3–5) \times 10^{13}$ cm^{-3}. Results are presented from the first measurements of the average density in the T-11M tokamak with the help of a pulsed time-of-flight refractometer by probing the plasma in the equatorial plane in a regime with the reflection of the probing radiation from the inner wall of the vacuum chamber. © *2004 MAIK "Nauka/Interperiodica".*

1. INTRODUCTION

Physical experiments in existing tokamaks (specifically, the studies of disruptions, regimes with a rapid density growth due to pellet injection, MHD oscillations, long-pulse regimes, etc.) require reliable measurements of the plasma density. Conventional phase interferometers undergo so-called phase jumps. For this reason, it is important to develop reliable and simple methods for measuring the plasma density.

In this paper, we describe two methods for measuring the plasma density that have been elaborated at the Troitsk Institute for Innovation and Fusion Research. The common feature of these methods is that they are unambiguous. One of them uses a multichannel phase-jump-free polarization interferometer (MUPI) based on the Cotton–Mouton effect. The instrument measures the phase difference between an ordinary (**E** ∥ **B**) and an extraordinary (**E** ⊥ **B**) microwaves passed through the plasma along the same chord [1, 2]. The second method utilizes a pulsed time-of-flight refractometer (PTFR) for measuring the line-averaged electron density [3–5]. The refractometer emits microwave probing pulses with a carrier frequency higher than the plasma frequency and, thus, operates in the transmission mode.

2. MULTICHANNEL PHASE-JUMP-FREE POLARIZATION INTERFEROMETER

When simultaneously probing a plasma by an ordinary and an extraordinary wave, the phase difference between them after passing through the plasma is determined by the expression [1, 2, 6]

$$\Delta\Phi_{o,e}(\omega, x) = \frac{\omega}{c}\int_l \Delta\eta_{o,e}(\omega, x, z)dz$$
$$\approx 2.45 \times 10^{-11}\lambda^3 B_T^2(x)\int_l n(x, z)dz, \quad (1)$$

where $\Delta\eta_{o,e}$ is the difference between the refractive indices for the ordinary and extraordinary waves and λ is the wavelength of the probing wave. Here, we take into account that, for a tokamak, the poloidal field is $B_{\rm pol} \le 0.1B_T$, and the total magnetic field B is replaced with the toroidal magnetic field B_T. By properly choosing the wavelength λ, the phase shift in the plasma can be made less than 2π. In particular, for the T-11M tokamak (the minor radius a = 20 cm, $\langle n\rangle = 4 \times 10^{13}$ cm^{-3}, and B_T = 1.2 T), the probing radiation wavelength must be no longer than 2.2 mm. In our experiments, we used an MUPI with a wavelength close to 2 mm. Detailed information on the operating principles of the polarization interferometer is given in [1].

In 2002, the first measurements were performed simultaneously in five probing channels (–13, –5, –1, +7, and +11 cm); this allowed us to reconstruct the time evolution of the density profile from the measured phase difference. The scheme of the measurements (Fig. 1) was analogous to that of the one-channel mea-

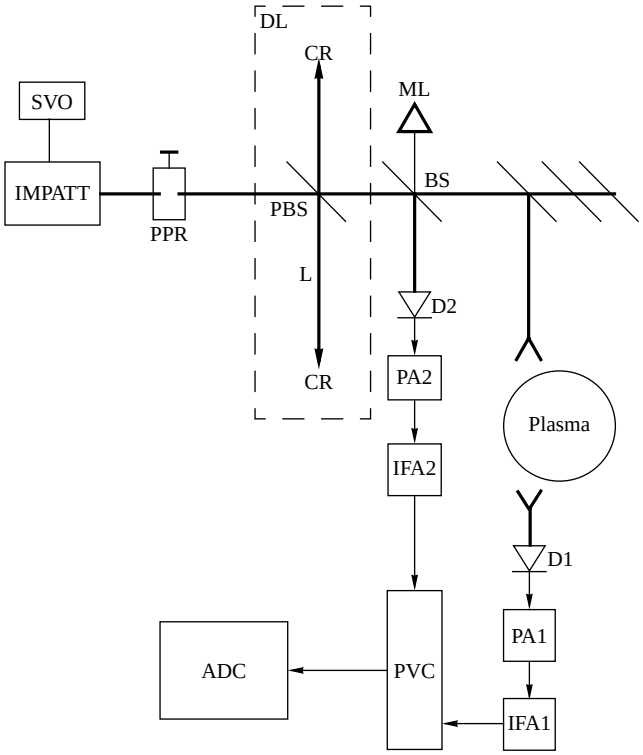

Fig. 1. Block diagram of the MUPI: (IMPATT) microwave IMPATT-diode oscillator, (SVO) sawtooth voltage oscillator, (PPR) polarization-plane rotator, (PBS) polarization beam splitter, (L) quasi-optical line, (CR) corner reflectors, (DL) delay line, (BS) beam splitter, (ML) matched load, (D1, D2) reference and measuring detectors, (PA1, PA2) preamplifiers, (IFA1, IFA2) intermediate-frequency amplifiers, (PVC) phase–voltage converter, and (ADC) analog-to-digital converter.

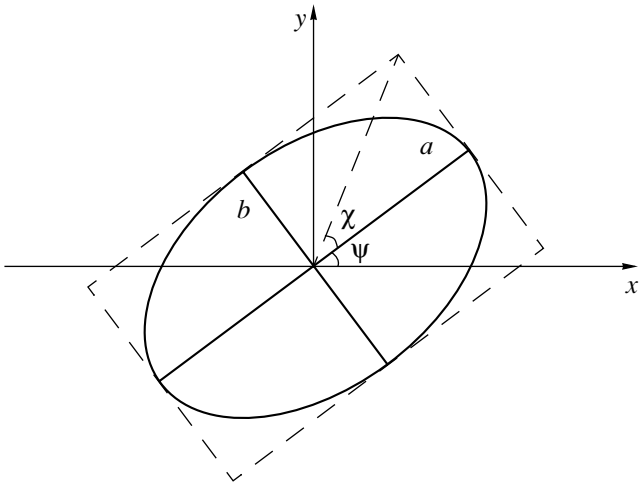

Fig. 2. Polarization ellipse for radiation propagating along the *z* axis.

surements in [1] and is very similar to the well-known scheme proposed by Wharton. The modulating voltage at a frequency of $f = 232.25$ kHz was applied from a sawtooth voltage oscillator (SVO) stabilized by a quartz resonator to the control input of a 15-mW tunable impact-ionization avalanche transit-time (IMPATT) oscillator operating at a frequency of nearly 140 GHz. To obtain two mutually perpendicular and frequency-shifted components of probing radiation, we used a microwave delay line (DL) consisting of a grid polarization beam splitter (PBS), two corner reflectors (CR), and a segment of the transmission line (L). The frequency-shifted components were used to transform the phase difference to an intermediate frequency. To obtain a signal at the intermediate frequency, it is sufficient to orient the polarization planes of the antennas of detectors D1 and D2 at an angle of about 45° to the toroidal magnetic field. In this case, the phases of the beat signals in quadratic detectors will be equal to the phase difference between the ordinary and extraordinary waves. The signal from detector D1 is a reference signal, whereas the signal from detector D2 is a measured signal. In this way, we avoid the influence of the oscillator frequency instability on the results of measurements.

In this interferometer scheme, the propagation path of the two probing waves outside the plasma was the same after the delay line DL. Consequently, the influence of vibrations of the vacuum chamber and antenna feeder on the results of measurements was also avoided. Radiation was transported through an overmoded waveguide (a metal tube with an inner diameter of 20 mm), including a turn and a vacuum and a dielectric decouplings. The antenna was a horn with an output aperture 26 mm in diameter. Probing was performed along vertical chords. The passed radiation was received by a similar horn. Shottky barrier diodes were used as mixers.

For multichannel probing, simple relation (1) is only applicable to the central probing channel (–1 cm). Under T-11M experimental conditions, the Faraday effect is comparable in value to the Cotton–Mouton effect. Hence, the problem of reconstructing the distribution $\langle nl \rangle$ from the corresponding measured values of the phase difference turns out to be rather involved. To resolve this problem, it is necessary to solve an equation describing the change in the polarization state of an electromagnetic wave propagating through a plasma [7].

Let a and b be a major and minor semiaxes of the ellipse describing the radiation polarization. Then, the polarization state can be described (see Fig. 2) by the angle $\psi (0 \le \psi \le \pi)$ between the major semiaxis and the x axis and also the angle χ defined as $\tan\chi = \pm b/a$ $(-\pi/4 \le \chi \le \pi/4)$. The positive sign of χ corresponds to clockwise rotation if we are looking toward the radiation source. The polarization state can also be described by a Stokes vector having the components

$$s_1 = \cos 2\chi \cos 2\psi, \quad s_2 = \cos 2\chi \sin 2\psi, \quad s_3 = \sin 2\chi, \tag{2}$$

so that $\mathbf{s}^2 = s_1^2 + s_2^2 + s_3^2 = 1$.

The full Stokes vector for processes involving a change in the radiation intensity J is defined by the equalities

$$S_0 = J, \quad S_1 = s_1 J, \quad S_2 = s_2 J, \quad S_3 = s_3 J, \qquad S_1^2 + S_2^2 + S_3^2 = S_0^2 = J^2. \tag{3}$$

The vector $\mathbf{s} = (1, 0, 0)$ corresponds to linearly polarized radiation with a polarization vector directed along the x axis, $\mathbf{s} = (0, \pm 1, 0)$ corresponds to linearly polarized radiation with a polarization vector oriented at an angle of $\pm 45°$ to the x axis, and the vector $\mathbf{s} = (0, 0, \pm 1)$ corresponds to circular polarization with two opposite senses of rotation.

It is well known [7] that the evolution of polarization in a uniform nonabsorbing medium with two characteristic refractive indices μ_1 and μ_2 ($\mu_1 > \mu_2$) can be described by the vector equation

$$\frac{d\mathbf{s}(z)}{dz} = \mathbf{\Omega} \times \mathbf{s}(z), \tag{4}$$

where $\mathbf{\Omega} = -\frac{\omega}{c}(\mu_1 - \mu_2)\mathbf{s}_{c2}$ and $\mathbf{s}_{c2}$ is the polarization vector of a fast wave. Let the particle collision frequency in the plasma be much lower than the probing radiation frequency ω and $\omega > \omega_p$ (where $\omega_p = (4\pi ne^2/m)^{1/2}$, e and m are the charge and mass of an electron, and n is the electron density); i.e., the cold plasma approximation is valid and the radiation absorption in the plasma is negligibly small. Let θ be the angle between $\mathbf{B}$ and the z axis (the propagation direction) and β be the angle between the y axis and $\mathbf{z} \times (\mathbf{B} \times \mathbf{z})$. Then, the refractive indices μ_1 and μ_2 and the vector $\mathbf{\Omega}$ are described by the expressions [8]

$$(\mu_{1,2})^2 = 1 - \frac{\omega_p^2}{\omega^2}\left\{1 + \frac{\omega_c^2}{\omega^2}\frac{\sin^2\theta}{2(1 - \omega_p^2/\omega^2)}(-1 \pm (1 + F^2)^{1/2})\right\}^{-1},$$

$$\mathbf{\Omega} = \frac{\omega_p^2}{(\mu_1 + \mu_2)c\omega^3 D}\begin{pmatrix} \left(\frac{e}{mc}\right)^2\left(\frac{B_x^2 - B_y^2}{1 - N}\right) \\ \left(\frac{e}{mc}\right)^2\left(\frac{2B_xB_y}{1 - N}\right) \\ \left(\frac{2\omega eB_z}{mc}\right) \end{pmatrix},$$

where

$$F = \frac{2\omega}{\omega_c}\left\{1 - \frac{\omega_p^2}{\omega^2}\right\}\frac{\cos\theta}{\sin^2\theta}, \quad N = \frac{\omega_p^2}{\omega^2},$$

$$D = 1 - \left(\frac{e}{\omega mc}\right)^2\left\{\frac{B_x^2 + B_y^2}{1 - N} + B_z^2\right\},$$

and $\omega_c = eB/mc$ is the electron cyclotron frequency. The polarization parameters ψ_{c2} and χ_{c2} describing the polarization state of the fast characteristic wave $\mathbf{s}_{c2}$ are given by the expressions $\psi_{c2} = -\beta$ and $\tan\chi_{c2} = -((1 + F^2)^{1/2} - 1)/F$. Using relation (4), we can find the resulting Stokes vector describing the polarization state of the radiation passed through the plasma for any initial vector $\mathbf{s}_0$ describing the polarization of radiation entering the plasma. This is sufficient when $\mathbf{s}_0$ is constant in time. However, many diagnostic methods (in particular, those employed in the T-11M tokamak) use time modulated polarization. In this case, it is more useful to apply the following relation derived in [7] to solve equation (4) with the initial condition $\mathbf{s} = \mathbf{s}_0$:

$$\mathbf{s}(z) = \mathrm{M}(z)\mathbf{s}_0, \tag{5}$$

where $\mathrm{M}(z)$ is the plasma transition matrix that satisfies the differential equation

$$\frac{d\mathrm{M}}{dz} = \mathrm{A}(z)\mathrm{M}(z),$$

$$\mathrm{A}(z) = \begin{pmatrix} 0 & -\Omega_3 & \Omega_2 \\ \Omega_3 & 0 & -\Omega_1 \\ -\Omega_2 & \Omega_1 & 0 \end{pmatrix}. \tag{6}$$

It is well known that a change in the polarization state $\mathbf{S}_0$ of an electromagnetic wave passed through an optical system is determined by the Müller matrix M of the optical system [9],

$$\mathbf{S}_1 = \begin{pmatrix} s_{10} \\ s_{11} \\ s_{12} \\ s_{13} \end{pmatrix} = \mathrm{M} \cdot \mathbf{S}_0 = \mathrm{M}\begin{pmatrix} s_{00} \\ s_{01} \\ s_{02} \\ s_{03} \end{pmatrix}.$$

It follows from relations (2) and (3) that, in our case, the initial Stokes vector of the probing wave has the form

$$\mathbf{S}_0 = J\begin{pmatrix} 1 \\ 0 \\ \cos\delta\omega t \\ \sin\delta\omega t \end{pmatrix},$$

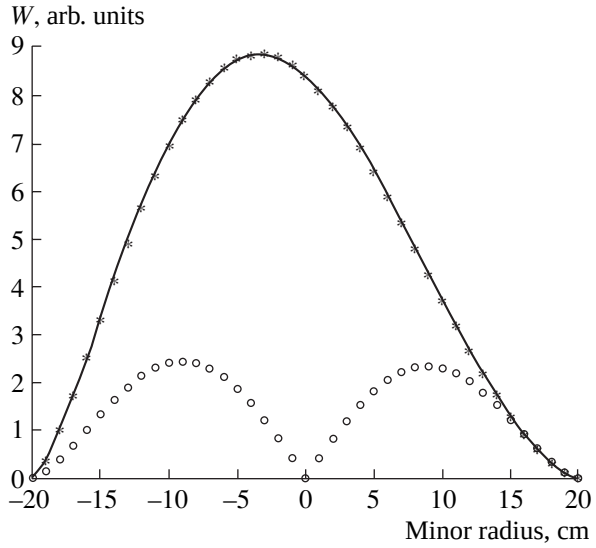

Fig. 3. Coefficients W_1 (asterisks) and W_3 (circles), describing the Cotton–Mouton and Faraday effects in the T-11M tokamak, respectively, as functions of the minor radius. In calculations, the plasma density and current density profiles were assumed to be parabolic, the central density was $N_0 = 6 \times 10^{13}$ cm^{-3}, the plasma current was $I_p = 100$ kA, and the toroidal magnetic field was $B_T = 1.2$ T.

where $\delta\omega t = 4\pi f$ is the intermediate signal frequency (the system is tuned to the second harmonic). The Müller matrix for polarizers placed at an angle of 45° in front of the detectors is defined by the expression [7]

$$\mathrm{M}_p = \frac{1}{2}\begin{pmatrix} 1 & 0 & 1 & 0 \\ 0 & 0 & 0 & 0 \\ 1 & 0 & 1 & 0 \\ 0 & 0 & 0 & 0 \end{pmatrix}.$$

Then, in view of Eqs. (2), (3), and (5), the signals at the reference and measuring detectors are described by the expressions

$$I_{D1} = 1/2J1(1 + \cos\delta\omega t) \sim \cos\delta\omega t,$$

$$I_{D2} = 1/2(1 + s_{12}) \sim J2(1 + M_{22}\cos\delta\omega t + M_{23}\sin\delta\omega t) \sim \cos(\delta\omega t - \Delta\Phi),$$

where $\tan\Delta\Phi = M_{23}/M_{22}$ and $J1$ and $J2$ are the radiation intensities in the reference and measuring channels, respectively. Accordingly, the phase difference between the signals is

$$\Delta\Phi = a\tan\left(\frac{M_{23}}{M_{22}}\right), \quad (7)$$

where M_{23} and M_{22} are the components of the plasma transition matrix $\mathrm{M}(z)$ determined by the plasma parameters. Thus, in our case, the problem of calculating the phase difference as a function of the plasma density reduces to the calculation of the two components of the plasma transition matrix $\mathrm{M}(z)$.

Let us introduce the dimensionless parameters

$$W_j = \int_{z_0}^{z_1} dz\Omega_j(z).$$

The parameters W_1 and W_2 describe the birefringence effect in plasma (the Cotton–Mouton effect), while the parameter W_3 describes the Faraday effect [7]. If the probing radiation propagates in the vertical direction and the x axis is directed along the major radius, then, for a tokamak symmetrical about the equatorial plane, the quantity $\Omega_2 \sim B_xB_y$ is an odd function of z and $W_2 = 0$. In the typical case of $W(z) = \int_{z_0}^{z} |\Omega(z')|dz' \ll 1$, there are approximate analytical solutions to equation (4). So, it is useful to estimate the values of W_1 and W_3 for the conditions of the T-11M tokamak.

Figure 3 shows the calculated coefficients W_1 and W_3, characterizing the relative contributions of the Cotton–Mouton and Faraday effects, respectively, as functions of the minor radius. In calculations, the density and current profiles were assumed to be parabolic, the density at the center of the plasma column was $N_0 = 6 \times 10^{13}$ cm^{-3}, the plasma current was $I_p = 100$ kA, and the toroidal magnetic field was $B_T = 1.2$ T. It can be seen from Fig. 3 that (i) both parameters are substantially higher than unity over almost the entire probing region and (ii) the Faraday effect for the outer channels of the interferometer is comparable to the Cotton–Mouton effect. It is commonly believed that, under these conditions, it is difficult to directly determine the global plasma parameters (such as the plasma density and the current density) from phase measurements (see, e.g., [7]). However, a comparison of the phase shift determined from Eqs. (5) and (6) for the polarization state with that calculated for the Cotton–Mouton effect by formula (1) shows that they differ slightly (Fig. 4). At least, this difference is not as large as one might expect from the calculations of W_1 and W_3 only. Apparently, this is explained by the fact that the condition $W(z) \ll 1$, under which the Faraday and Cotton–Mouton effects can be separated, is too strong. This allows us to use the following algorithm for determining $\langle nl\rangle_i$ from the measured values of the phase difference $\Delta\Phi_i$ for our case, in which the plasma effects are large:

(i) First, by solving Eqs. (5) and (6) for the polarization state, we find the relation between $\langle nl\rangle_i$ and $\Delta\Phi_i$ for a given density and current profiles; i.e., we determine the calibration curves for all the interferometer channels.

(ii) We then verify that these curves are slightly sensitive to the shape of the current density profile and calculate the calibration curves for the interferometer channels in the quasi-steady phase of a discharge,

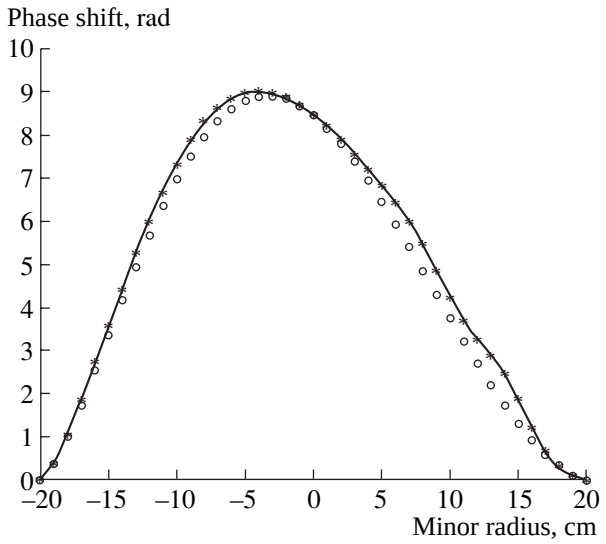

Fig. 4. Phase shift of a microwave passed through the plasma: a pure Cotton–Mouton effect (circles) and the exact solution of Eqs. (3) and (4) (asterisks) for the same parameters as in Fig. 3.

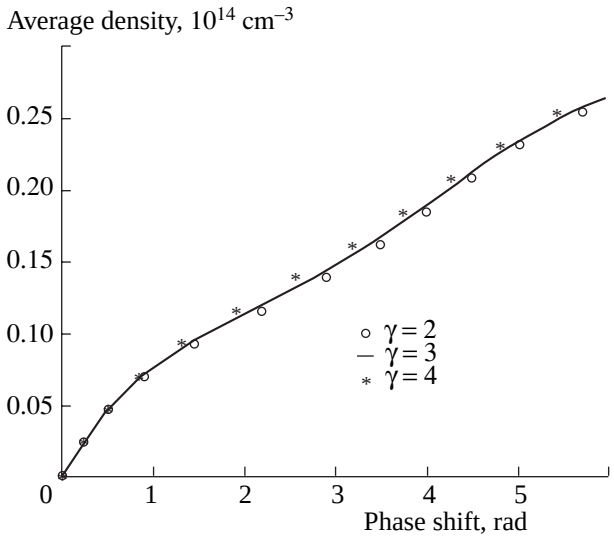

Fig. 5. Calibration curves calculated for the +11-cm channel of the MUPI for $N_0 = 7.5 \times 10^{13}$ cm^{-3}; $B_T = 1.2$ T; a parabolic plasma density profile with the index $\alpha = 1.5$; and parabolic current density profiles with the indices $\gamma = 2$ (asterisks), 3 (solid line), and 4 (circles).

assuming that the current profile is described by the formula $j(r) = j(0)\left(1 - \frac{r^2}{a^2}\right)^{\gamma}$, where $\gamma = 1 - q(a)$ [10] and $q(a)$ is the safety factor at the plasma boundary.

(iii) Applying a common inversion procedure, we determine the plasma density profile $n(r)$ from the measured values of $\langle nl \rangle_i$ [11].

(iv) We then return to step (i); i.e., we solve the equation for the polarization state using the plasma density profile obtained at step (iii), calculate the modified calibration curves, and determine the corrected values of $\langle nl \rangle_i$ using these curves.

(v) After several such cycles, we arrive at a sufficiently correct profile of the plasma density.

The equation of the polarization state was solved numerically by the method described in [12].

Figure 5 shows the calibration curves for the +11-cm channel for a parabolic density profile and different current density profiles. It can be seen that these curves differ by no more than ±4%.

In practice, when calculating the calibration curves, it is necessary to consider another factor, namely, the refraction of the probing beam in the plasma. This refraction is different for ordinary and extraordinary waves; consequently, the beams leave the plasma at different angles and follow different paths to the detector. In the absence of plasma, this effect is naturally absent. For this reason, when calculating the calibration curves, it is necessary to consider the phase shift between the two components of the probing beam that appears outside the plasma, because the wave fronts of the interfering waves are tilted [6]. Figure 6 shows the calibration curves for the +11-cm channel that were calculated with and without allowance for refraction, which was calculated by a method similar to that described in [6]. (The method was somewhat modified by taking into account the beam trajectory calculated by the ray-tracing technique in the geometric-optics approximation.)

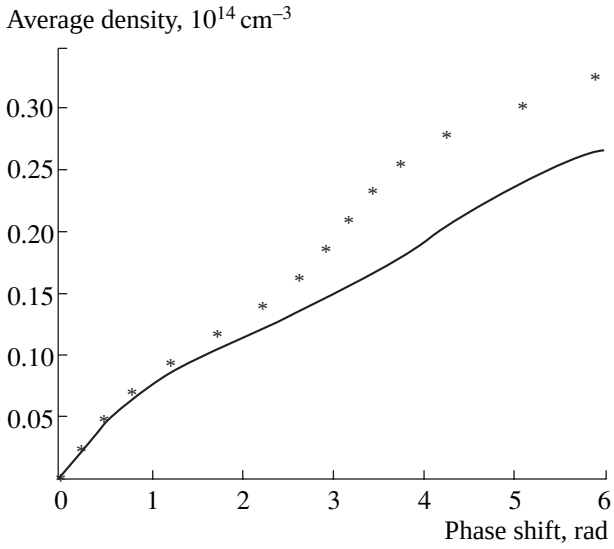

Fig. 6. Calibration curves calculated for the +11-cm channel of the MUPI with (solid line) and without (asterisks) account taken of refraction for $\gamma = 3$; the other parameters are the same as in Fig. 5.

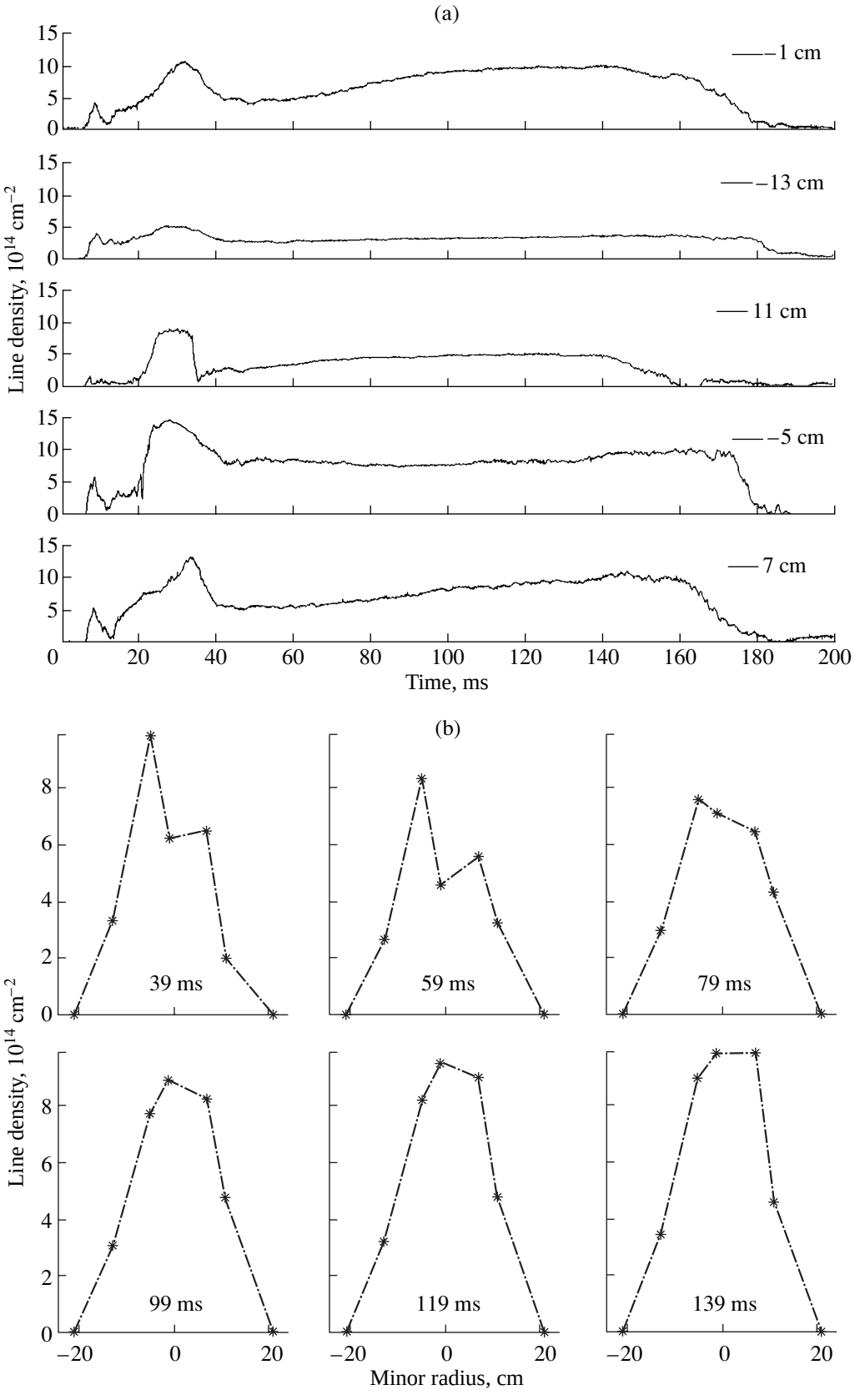

Fig. 7. (a) Line-density signals from the five interferometer channels for shot no. 17070, (b) the time evolution of the line density profile, and (c, d) the reconstructed time evolution of the density profile during the discharge.

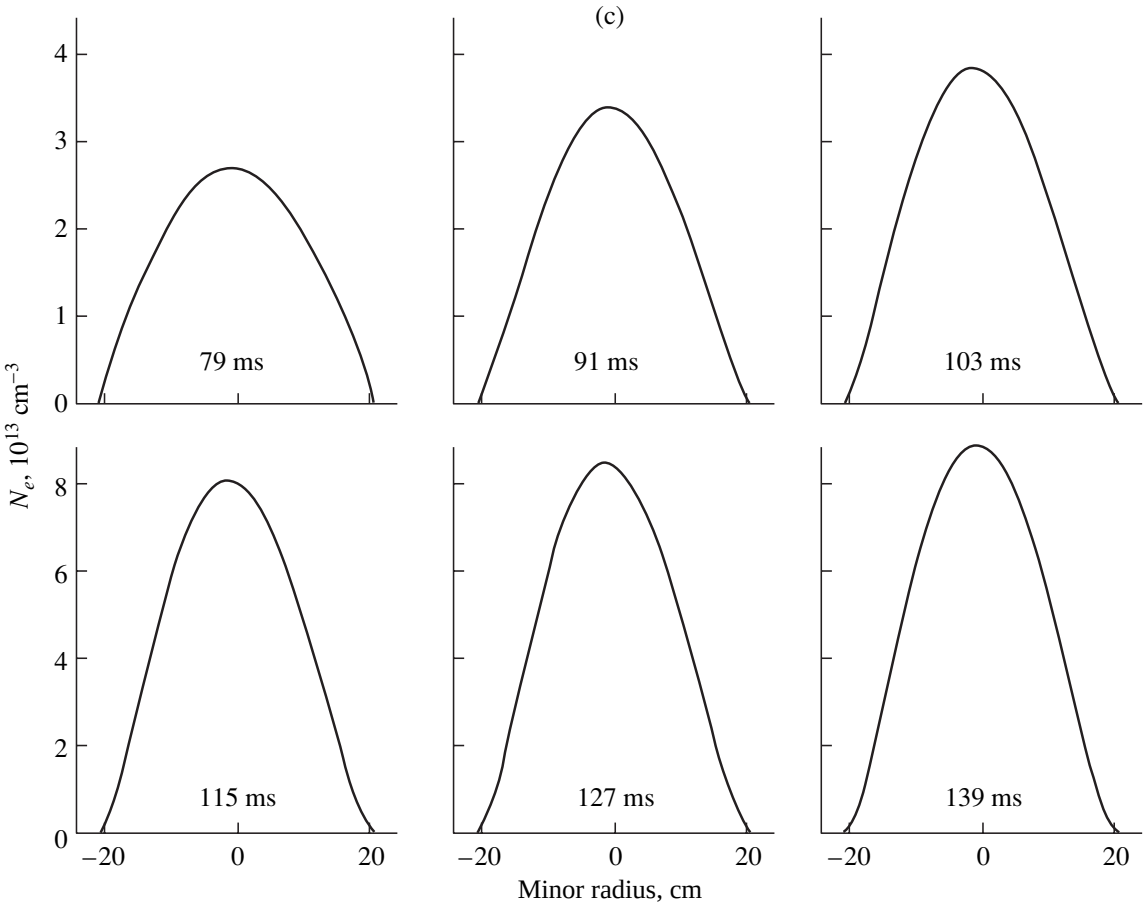
(c)
79 ms
91 ms
103 ms
115 ms
127 ms
139 ms
N_e, 10^{13} cm^{-3}
Minor radius, cm

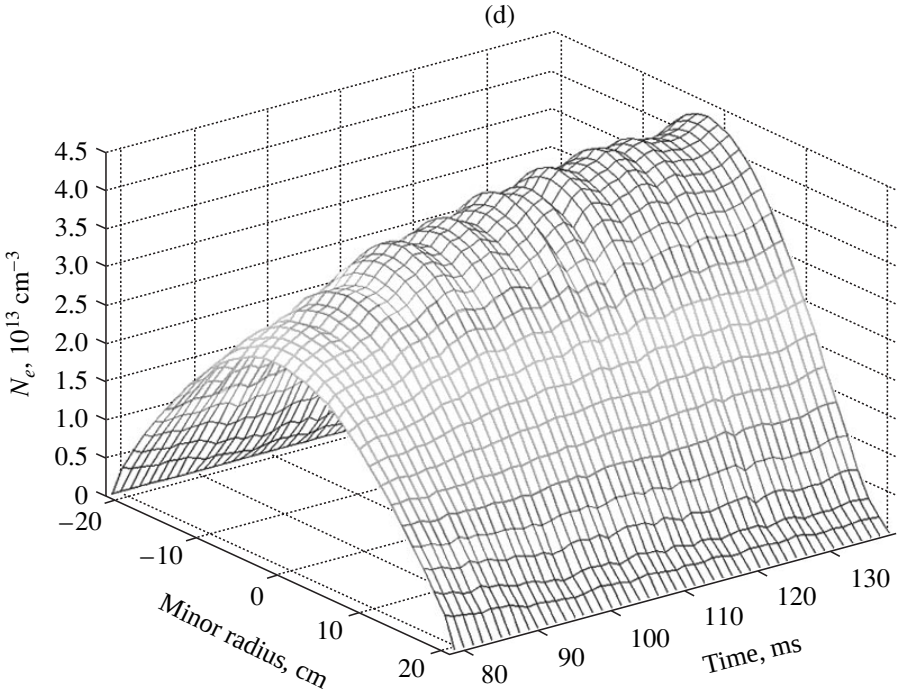
(d)
N_e, 10^{13} cm^{-3}
Minor radius, cm
Time, ms

Fig. 7. (Contd.)

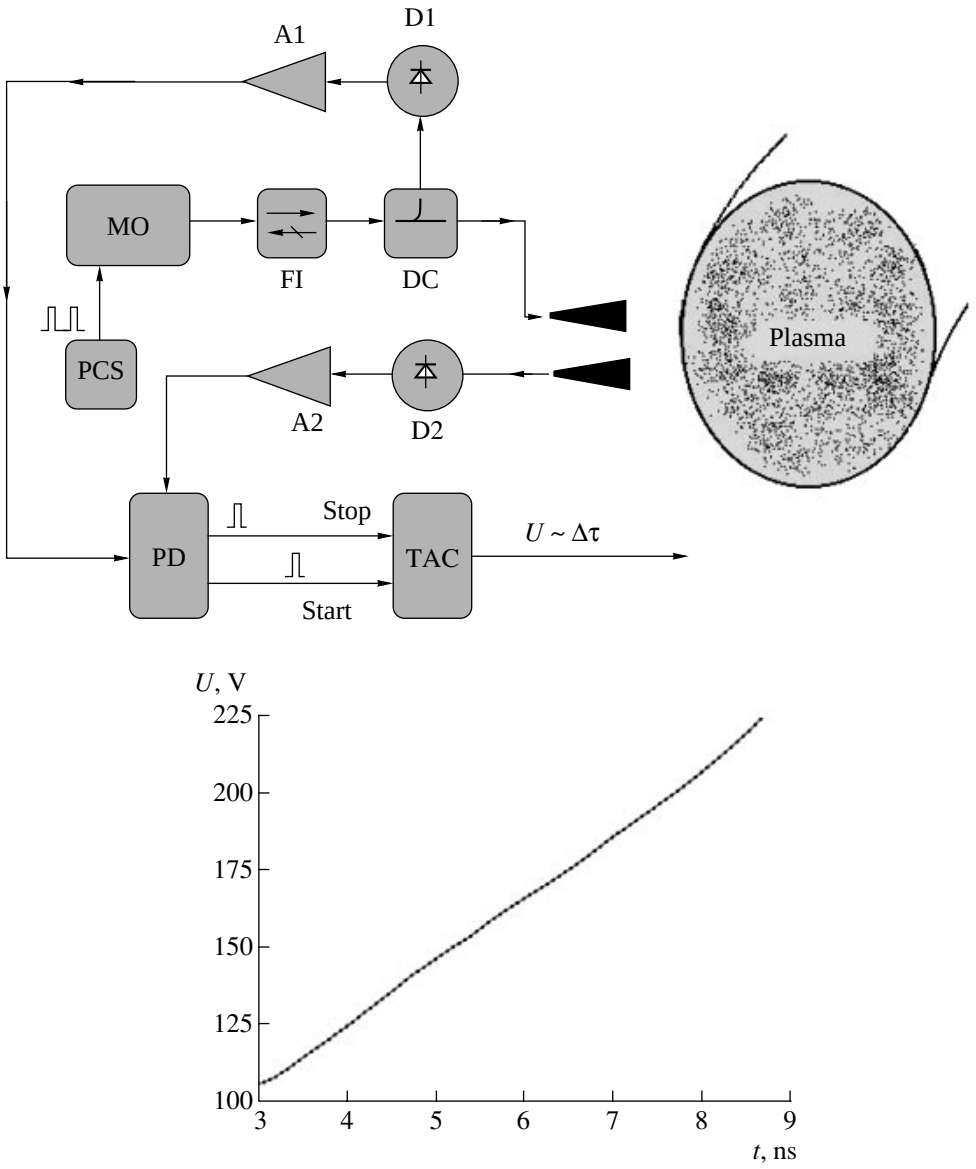

Fig. 8. Block diagram of the PTFR (on top) and the calibration curve (on bottom): (MO) microwave oscillator, (PCS) pulsed current source, (FI) ferrite isolator, (DC) directional coupler, (D1, D2) reference and measuring detectors, (A1, A2) pulsed amplifiers, (PD) pulse discriminator, and (TAC) time–amplitude converter.

It can be seen that refraction contributes substantially to the results of the measurements (up to 30%) and must certainly be taken into account. For the central channel, this effect can be ignored.

Figure 7 shows the line-density signals from the five interferometer channels for shot no. 17070 (a discharge with a hot lithium limiter [13]), the time evolution of the line-density profile, and the reconstructed time evolution of the density profile during the discharge. The obtained profiles are well approximated by a parabola with the index $\alpha = 1–1.6$ ($N(r) = N(0)(1 - r^2/a^2)^\alpha$). In the early stage of the discharge, the profile has a minimum at the center. The average density in the central channel then increases from 1.8×10^{13} to 2.46×10^{13} cm^{-3}, and the profile changes from a parabola with $\alpha = 1.0$ (at 79 ms) to a parabola with $\alpha = 1.6$ (at 139 ms). It can be seen from Fig. 7d, that the average density increases primarily due to the growth of the density in the central region of the plasma column.

3. PULSED TIME-OF-FLIGHT REFRACTOMETER FOR MONITORING THE LINE-AVERAGED DENSITY IN THE T-11M TOKAMAK

The time delay τ measured by the PTFR in plasma is proportional to the line density and is inversely pro-

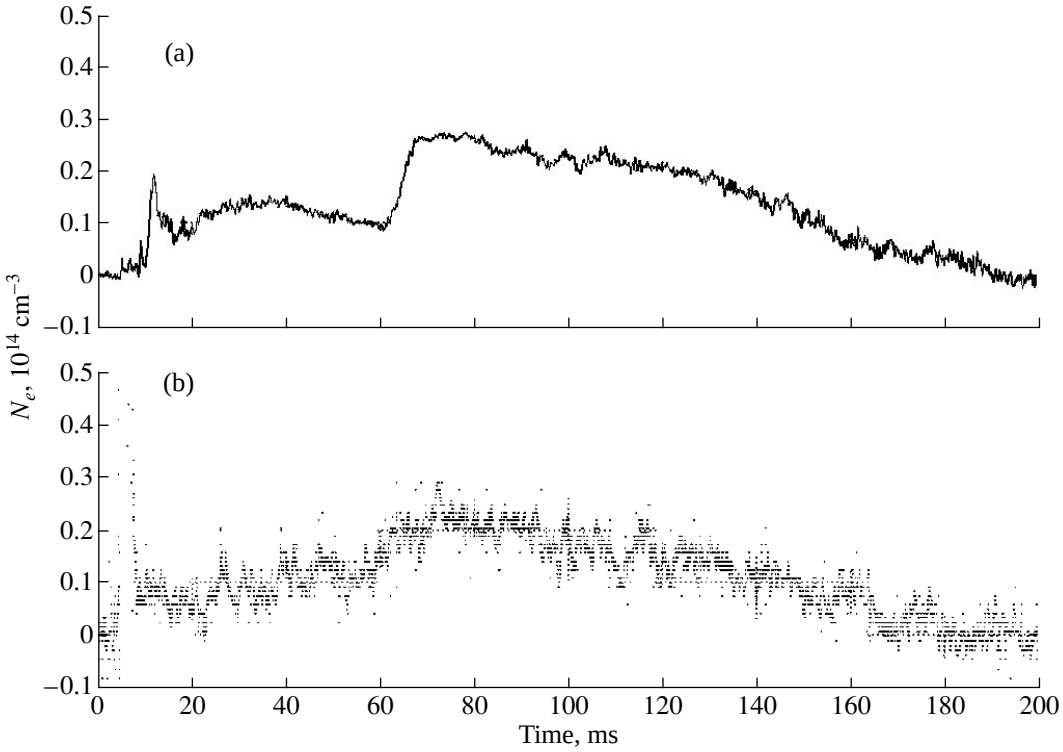

Fig. 9. Average density measured (a) in the –1-cm channel of the MUPI (vertical probing) and (b) by the PTFR (horizontal probing in the equatorial plane in the double-pass regime with reflection of the probing radiation from the inner wall of the vacuum chamber) in shot no. 16201.

portional to the squared carrier frequency f of the probing wave (ordinary-wave probing) [3, 4]

$$\tau_{gr,o} = \frac{d\Phi(\omega)}{d\omega} \approx k\frac{1}{f^2}\int_l n(z)dz. \quad (8)$$

We developed and tested a prototype PTFR with a carrier frequency of 140 GHz. This frequency is sufficient for measuring the line-averaged density in the T-11M tokamak in regimes with a nominal density of $(3–5) \times 10^{13}$ cm^{-3}. The structure of the instrument and the scheme of measurements (see Fig. 8) coincide with those described in [3, 4]. Figure 9 shows the line-density signals measured by the MUPI (vertical probing) and the PTFR (horizontal probing in the equatorial plane in the double-pass regime with reflection of the probing radiation from the inner wall of the vacuum chamber). The measurements were carried out in experiments with additional gas puffing from a piezoelectric valve located on the low-field side of the chamber, in the same poloidal cross section in which the MUPI channels and the PTFR were installed. In these experiments, the signal-to-noise ratio in the PTFR data was rather low because the power of the prototype oscillator used in the PTFR was relatively low and the detector had a low sensitivity. In addition, the receiving and transmitting antennas were not equipped with focusing lenses. However, even under such unfavorable conditions, we could measure the time behavior of the line-averaged density. It can be seen that the time behavior of the density was somewhat different on the vertical and horizontal chords.

4. CONCLUSIONS

(i) The first measurements of the plasma density profile with the help of the MUPI have been carried out in the T-11M tokamak in the ohmic regime, regimes with a Li limiter, and ICR heating regimes. In a discharge with a hot lithium limiter, the measured profiles are well approximated by a parabola with the index α = 1.0–1.6. In the early stage of the discharge, the profile has a minimum at the center. The profile then changes from a parabola with $\alpha = 1.0$ to a parabola with $\alpha = 1.6$.

In future experiments, we plan to perform the following tasks:

to enhance the sensitivity and time resolution and to increase the number of simultaneously operating channels;

to use analog-to-digital converters with small jitter for data acquisition and to use special programs for calculating the phase difference;

to carry out simultaneous measurements of the Faraday effect, which will allow us to determine the current-density profile in the tokamak; and

to use the signal from the interferometer as a command signal in the system for controlled gas puffing.

(ii) A prototype PTFR with a carrier frequency of 140 GHz has been developed, and the first measurements of the average density in the T-11M tokamak have been carried out. The probing was performed in the equatorial plane in regimes with a nominal density.

Further, we plan to create a higher power PTFR, to develop a detector for controlling the vertical position of the plasma column with the help of the PTFR, and to use the PTFR to measure the average plasma density by probing along a vertical chord.

ACKNOWLEDGMENTS

We thank Prof. S.E. Segre for his useful comments and V.G. Merezhkin for some fruitful discussions and for providing us with the Abel inversion code that was used to reconstruct the time evolution of the plasma density profile.

REFERENCES

1. V. F. Shevchenko, A. A. Petrov, V. G. Petrov, and Yu. A. Chaplygin, Fiz. Plazmy **22**, 32 (1996) [Plasma Phys. Rep. **22**, 21 (1996)].
2. V. G. Petrov and A. A. Petrov, in *Theoretical and Experimental Studies Performed at the TRINITI Department of the Physics of Tokamak Reactors in 2001* (TRINITI, Troitsk, 2002), p. 116.
3. A. A. Petrov, V. G. Petrov, A. Yu. Malyshev, *et al.*, Fiz. Plazmy **28**, 877 (2002) [Plasma Phys. Rep. **28**, 806 (2002)].
4. V. Petrov, A. Petrov, and A. Romannikov, in *Proceedings of the 29th EPS Conference on Plasma Physics and Controlled Fusion, Montreux, 2002*; ECA **26B**, 4.127 (2002).
5. A. A. Petrov and V. G. Petrov, Rev. Sci. Instrum. **74**, 1465 (2003).
6. D. Veron, *Infrared and Millimeter Waves* (Academic, New York, 1979), Vol. 2, p. 71.
7. S. E. Segre, Plasma Phys. Controlled Fusion **41**, R57 (1999).
8. M. A. Heald and C. B. Wharton, *Plasma Diagnostics with Microwaves* (Wiley, New York, 1965; Atomizdat, Moscow, 1968).
9. R. M. A. Azzam and N. M. Bashara, *Ellipsometry and Polarized Light* (North-Holland, Amsterdam, 1977; Mir, Moscow, 1981).
10. S. V. Mirnov, *Physical Processes in Tokamak Plasma* (Énergoatomizdat, Moscow, 1985), p. 49.
11. E. P. Gorbunov, V. F. Denisov, V. G. Merezhkin, *et al.*, in *Proceedings of the 10th All-Russia Conference on the Diagnostics of High-Temperature Plasma, Troitsk, 2003*, Paper No. B6.
12. G. Dattoli and S. E. Segre, Phys. Plasmas **4**, 898 (1997).
13. V. B. Lazarev, E. A. Azizov, A. G. Alekseyev, *et al.*, in *Proceedings of the 30th EPS Conference on Plasma Physics and Controlled Fusion, St. Petersburg, 2003*; ECA **27A**, 3.162 (2003).

Translated by N.F. Larionova

Plasma Physics Reports, Vol. 30, No. 2, 2004, pp. 121–127. Translated from Fizika Plazmy, Vol. 30, No. 2, 2004, pp. 139–146.

PLASMA DIAGNOSTICS

X-ray Backlighting of the Periphery of an Imploding Multiwire Array in the Angara-5-1 Facility

E. V. Grabovskiĭ, K. N. Mitrofanov, G. M. Oleĭnik, and I. Yu. Porofeev

Troitsk Institute for Innovation and Fusion Research, Troitsk, Moscow oblast, 142190 Russia

Received July 24, 2003

Abstract—Backlighting diagnostics for studying the peripheral region of an imploding liner in the Angara-5-1 facility by using X-ray emission from an X-pinch is described. The spatial resolution of the diagnostics was no worse than 4 μm. The X-pinch emission passed through the plasma was recorded with a photofilm. The plasma density was reconstructed from the photofilm blackening density with the help of a step attenuator made of the same material as the liner. Results are presented from experiments on X-ray backlighting of the peripheral region of a multiwire liner at the 70th ns after the beginning of the discharge. It was found that, by this time, the wire cores were depleted to different extent, their masses totalled 70% of the original wire mass, and their diameters had increased approximately threefold. The plasma ejected from the wire cores was found to be axially stratified with a spatial period of 200 μm. Sometimes the axial nonuniformity of the core material with a characteristic scale length of 20 μm was observed. *© 2004 MAIK "Nauka/Interperiodica".*

1. INTRODUCTION

The current-induced implosion of cylindrical tungsten-wire arrays (liners) has been studied since the late 1980s [1–6]. The high-power soft X-ray pulse generated in the phase of maximum compression and the stagnation of the plasma in the final stage of the liner implosion is used in inertial confinement fusion research and in studying the equations of state of various substances at ultrahigh energy densities.

Knowledge of the time evolution of the mass density distribution inside imploding liners is of great importance for understanding the physics of implosion. One of the methods for determining the absolute value of the mass density in such objects is through plasma backlighting with emission from a point X-ray source. The duration of the X-ray burst from such a source should be much shorter than the characteristic times of the processes occurring in the plasma under study. The data on absorption of the probing radiation are used to determine the plasma density in the liner. An X-ray source for such backlighting can be either a plasma created by a high-power short-duration laser beam focused onto a solid target [7, 8] or an X-pinch burst [9–11].

In this study, an X-pinch source was used for backlighting [12]. The data on the absorption of X-ray emission in the liner plasma was obtained by recording the transmitted emission on a photofilm.

Along with measuring the absorption coefficient in plasma by recording two-dimensional images of the liner on an X-ray film (as in fluorography), this study was also aimed at determining the distribution of the mass density in the peripheral part of a tungsten wire liner in the course of its implosion.

2. EXPERIMENTAL SETUP

A scheme of the experiment on X-ray backlighting of the liner periphery is shown in Fig. 1. The system was adjusted in such a way that the images of both the internal and external regions of the liner were recorded on an X-ray film (i.e., the line of sight passed along the tangent to the cylindrical surface of the array, as is shown in Fig. 1). In our experiments, X-ray films were placed at a distance of 1.2 m from the X-pinch.

The X-pinch array consisted of four crossed 20-μm-diameter Mo wires that were connected at their middle points. The X-pinch array was set in place of one of the eight return-current posts at a distance of 45 mm from the liner axis (see Fig. 2). Therefore, it was connected in series with the main load (liner) of the generator. Consequently, the X-pinch was synchronized with the Z-pinch. The X-pinch emitted more than 200 mJ per burst into a 4π solid angle [13].

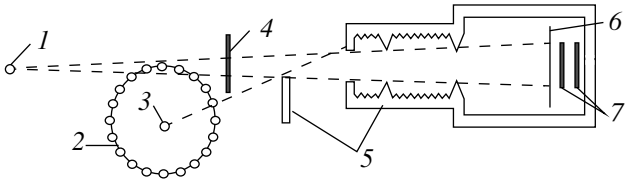

Fig. 1. Scheme of the experiment on X-ray backlighting of the liner periphery: (*1*) X-pinch, (*2*) wire array, (*3*) Z-pinch, (*4*) test wire, (*5*) system of screens and diaphragms, (*6*) foil, and (*7*) X-ray films placed one behind another.

1063-780X/04/3002-0121$26.00 © 2004 MAIK "Nauka/Interperiodica"

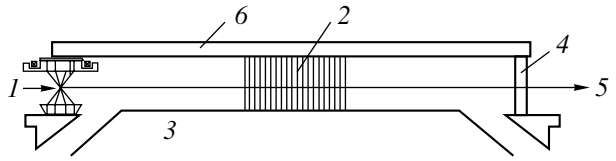

Fig. 2. X-pinch arrangement on the anode disc (side view): (*1*) X-pinch, (*2*) multiwire array (liner), (*3*) liner cathode, (*4*) return-current post, (*5*) to the detector, and (*6*) liner anode.

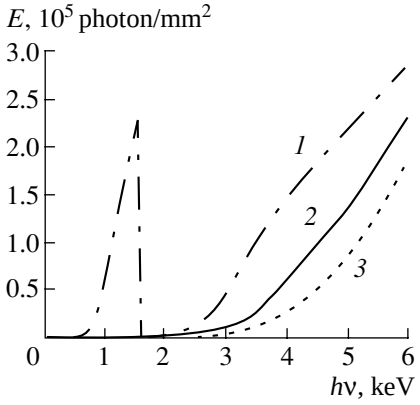

Fig. 3. Spectral sensitivity of a UF-ShS X-ray film placed (*1*) behind a 10-μm Al foil, (*2*) behind a 10-μm Al foil and 100-μm X-ray film, and (*3*) behind a 10-μm Al foil and two 100-μm X-ray films. The sensitivity curves correspond to a film blackening density of $D = 1$.

2.1. Detector of X-pinch Emission

The X-pinch emission was recorded on RF-3 and UF-ShS X-ray films.

The spectral sensitivity and the characteristic curves of the UF-ShS X-ray film were measured in [14]. More detailed information on the UF-ShS X-ray film is presented in [15].

The X-ray films were placed one behind another. The first (RF-3) film recorded an X-ray image created by X rays that passed through a 16-μm Ti foil or 10-μm Al foil. The second film recorded an X-ray image produced by X rays that passed through a metal foil and the first X-ray film with a thickness of 100 μm. Thus, every subsequent X-ray film recorded an image produced by harder X rays than the previous one. In the Angara-5-1 facility, up to four X-ray films were placed one behind another.

The spectral sensitivities of UF-ShS X-ray films placed behind a 10-μm Al foil (curve *1*), behind a 10-μm Al foil and 100-μm X-ray film (curve *2*), and behind a 10-μm Al foil and two 100-μm X-ray films (curve *3*) are shown in Fig. 3. The curves are plotted for a film blackening density of $D = 1$.

2.2. Selection of X-pinch Emission against the Background Z-pinch Emission

A specific feature of the backlighting of multiwire arrays with X-pinch emission is that the Z-pinch is a much more intense source of X-ray emission than the X-pinch. Hence, it can substantially contribute to the detector output signal. When recorded on an X-ray film, this will manifest itself as a parasitic exposure of the film.

In the final stage of implosion, the power of X-ray emission from the Z-pinch reaches 6 TW, the pulse duration is 5–10 ns, and the characteristic photon energy is less than 2 keV. The emission zone, which has a diameter of 0.4–2 mm and height of 1 cm, resides on the axis of the multiwire array [16]. Meanwhile, the power of the X-ray emission from the X-pinch in the photon energy range of 2–20 keV is no higher than 300 MW [13]; i.e., it is lower by a factor of 30000. The ratio between the Z- and X-pinch emission energies (30–80 kJ and 200–700 mJ, respectively) is of the same order of magnitude (actually, somewhat higher). Although the photon energy ranges of emission from the Z- and X-pinches formally do not overlap, there is always a high-energy tail in the Z-pinch emission spectrum. This tail overlaps with the X-pinch emission spectrum, and the power and energy of this tail can be comparable to those of X-pinch emission. In the final stage of implosion, the scattered Z-pinch emission can be also comparable in power to X-pinch emission.

To prevent the X-ray film from exposure to the forward and scattered X-ray emission from the Z-pinch, a set of screens and diaphragms were placed between the Z-pinch and X-ray films (see Fig. 1). The diaphragms also protected the films from exposure to scattered hard X rays. To shield the films from the microparticle flows and radiation arising at the instant of liner pinching, as well as from plasma radiation emitted from the liner periphery, the films were coated with a 16-μm Ti foil or 10-μm Al foil.

2.3. Spatial and Temporal Resolution of the Diagnostics

The instant of the X-pinch burst and its duration were determined using pin diodes. The measurements with pin diodes [13] showed that the full width at half-maximum of the X-pinch emission pulse is ≈1.8 ns in the photon energy range of >2 keV and 1.5 ns in the range of >5 keV. These values characterize the time resolution of X-ray backlighting. The true duration of the X-pinch emission pulse was probably shorter than the measured one because the temporal resolution of pin diodes was ≈1.2 ns; hence, it was not possible to record shorter pulses.

The spatial resolution of the recorded shadowgraphs was determined by several factors. These were diffraction, the refraction of the probing beam in a medium with a variable density, the interference of the deflected

beams, and the finite source dimensions. We estimated the role of diffraction. For this purpose, we calculated the distribution of the relative radiation intensity on the screen set behind an opaque strip of width d. The calculations were performed using the Fresnel method. The emission spectrum was assumed to lie in the range 1–8 keV. The modification of the spectrum by a filter consisting of a 10-μm Al foil and one 100-μm X-ray film placed behind the foil was also taken into account. The distance between the source and the strip was 5 cm, and the distance between the strip and the screen was 1.2 m. The full width at a level of one-half of the sum of the minimum intensity (in the shadow region) and the unperturbed intensity (far enough from the strip shadow) was taken as the width of the diffraction pattern obtained. This width was recalculated to the original object with account taken of the scaling factor. The intensity distribution behind the strip with a thickness of d = 4 μm recalculated to the object is shown in Fig. 4a. The shadow width is Δ = 5.8 μm. The shadow width Δ as a function of d is shown in Fig. 4b. The diagonal in this figure corresponds to a situation in which diffraction is absent and the shadow width is equal to the strip width. It can be seen that the distance between this diagonal and the curve Δ(d) is no larger than 3 μm. Formally, to determine the diffraction-limited spatial resolution, one should find the response for a zero-width strip. However, such a response would be of infinite width. The leftmost point on the Δ(d) dependence has the coordinates d = 1.5 μm and Δ = 4.5 μm. Taking into account the results of the above calculations and the width of the diffraction pattern, the diffraction-limited spatial resolution can be estimated as no worse than 4 μm.

To verify the spatial resolution of the diagnostics and determine the source size, 5-μm test wires (with no current) were placed near the liner under study (see Fig. 1). It can be seen from Fig. 5 that the 5-μm test wire is recorded correctly. This fact, together with the estimated value of the diffraction-limited spatial resolution (4 μm), evidences that the contribution of any of the other factors to the spatial resolution is lower than that of diffraction. This allows us to obtain an upper estimate for the source size. In the case of an X-pinch burst, the source size is less than 4 μm. In [17], the size of an X-ray source on the basis of an X-pinch was found to be less than 2 μm in the photon energy range >4 keV.

To find the relation between the blackening density of X-ray films and the mass density of the liner material, we performed the following calibration procedure. A step attenuator made of the same material as the liner (in our case, tungsten) was placed in front of the X-ray films (this is not shown in Fig. 1). The step attenuator consisted of tungsten filters with surface densities from 300 to 1300 μg/cm^2. The filter shadows in the X-pinch emission were recorded on X-ray films. The surface density of the plasma under study was estimated by comparing the film blackening density measured in the experiment with that obtained in the calibration procedure.

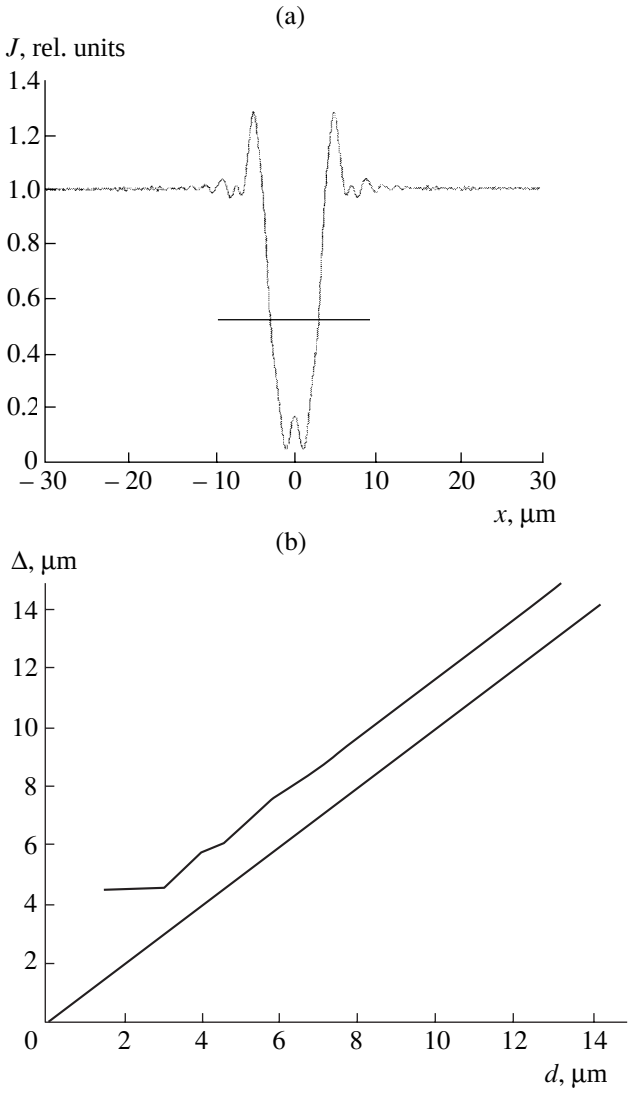

Fig. 4. Simulations of the shadow produced by an opaque strip with allowance for diffraction: (a) the intensity profile $J(x)$ behind the strip with a thickness of d = 4 μm (the profile is recalculated to the object with account taken of the scaling factor; the horizontal straight line shows the ordinate used to determine the shadow width) and (b) the shadow width Δ as a function of the strip width d (the diagonal corresponds to a situation in which diffraction is absent and the shadow width is equal to the strip width). Simulations were performed for the X-pinch emission spectrum (1–8 keV) modified by a filter consisting of a 10-μm Al foil and a 100-μm X-ray film (Fig. 3, curve *2*).

3. BACKLIGHTING OF THE LINER PERIPHERY

The results of the X-ray backlighting of the peripheral region of a multiwire array at t = 70 ns after the beginning of the discharge, when the current per wire had reached 50 kA, are shown in Fig. 5. The liner, 12 mm in diameter and 1 cm in length, consisted of 40

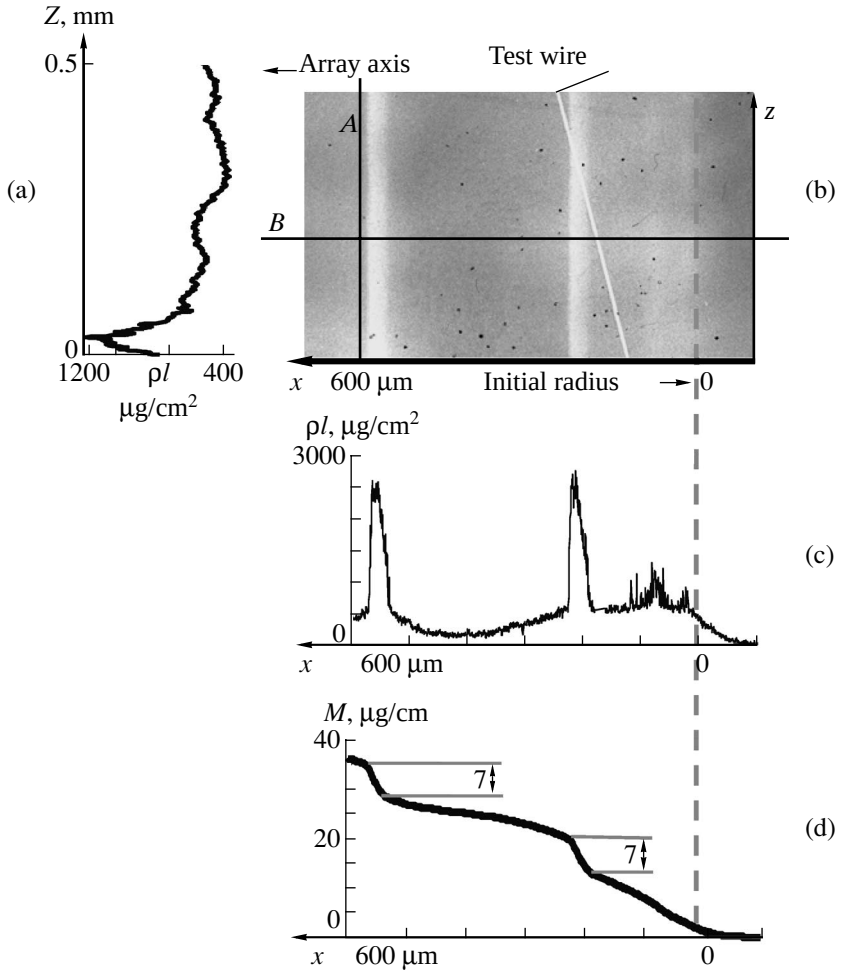

Fig. 5. Mass density distribution in the imploding liner at $t = 70$ ns from the beginning of the discharge: (a) the profile of the surface plasma density along straight line *A*, (b) the shadows of the test wire (slanting line) and dense cores (vertical bands), (c) the profile of the surface plasma density along straight line *B*, and (d) the linear density of the substance located between the outer boundary of the liner and the current *x* coordinate. The liner with a diameter of 12 mm consists of 40 8-μm tungsten wires. The interwire distance is 1 mm. The wire linear density is 9.5 μg/cm.

8-μm tungsten wires with a linear density of 9.5 μg/cm. Figure 6 shows the waveforms of the current through the liner, the power of soft X-ray emission from the Z-pinch, and the X-pinch emission power under conditions corresponding to Fig. 5.

A fragment of a shadowgraph obtained by the backlighting method is shown in Fig. 5b. The results of processing this shadowgraph are shown in Figs. 5a, 5c, and 5d. The *x* and *z* axes in Fig. 5b define the coordinate system that will be used subsequently. The *x* axis is directed along the radius from left to right (toward the array axis), the origin $x = 0$ being at the point with the *r* coordinate corresponding to the initial radius of the wire array. The *z* axis is directed along the liner axis (toward the anode), the origin $z = 0$ being at the bottom of the shadowgraph fragment.

The light slanting line on the shadowgraph fragment is a shadow produced by a 5-μm test wire. At $x = 220$ μm and $x = 550$ μm, one can clearly see the shadows of two dense wire cores.

The shadowgraph of the step tungsten attenuator with a known surface density (this is not shown in Fig. 5b) allowed us to estimate the plasma mass density at different liner points. Below, we will use such a characteristic of the mass density distribution as the surface density ρl [μg/cm²], which is the integral of the plasma mass density $\int \rho dl$ along a straight line *l* passing through the X-pinch and the point with coordinates (*x*, *z*).

The profiles of the surface density ρl along lines *A* and *B* are shown in Figs. 5a and 5c, respectively. In Fig. 5b, line *B* is directed radially and passes at the midheight of the shadowgraph fragment ($z = 0.25$ mm), while line *A* is directed axially and passes at a distance of 5 μm from the left margin of the left dense core ($x = 568$ μm).

In Fig. 5c, the profile of the plasma surface density ρl has two 25-μm-wide peaks (at x = 220 μm and x = 550 μm) corresponding to the shadows of the two dense cores. The diameter of the dense cores is larger than initial wire diameter by a factor of ~3; i.e., 60–80 ns after the beginning of the discharge, the diameter of the liner wires increases nearly threefold. To the right of the dense cores, there are two faint fuzzy peaks (at x = 20 and 80 μm) corresponding to the shadows of the two cores that have evaporated to a much greater extent. In the shadowgraphs, these have almost evaporated, and their smeared cores manifest themselves as variations in the blackening density over the entire length of the initial wires (see, e.g., the shadowgraph fragment presented in Fig. 5b). This fact evidences (i) that smeared cores do exist and (ii) that different wires evaporate to different extent; this could be related to the nonuniformity of plasma production and, perhaps, the nonuniformity of the liner current.

The integral of the plasma surface density ρl [μg/cm^2] from Fig. 5c taken over the x axis,

$$M(X) = \int_{-\infty}^{x} \rho l dx,$$

is shown in Fig. 5d. It is a function of the x coordinate and gives the linear mass density M [μg/cm] of the substance located between the outer boundary of the liner and the current x coordinate. Although the lower integration limit was set at $-\infty$, the integral was actually taken from the outer boundary ($x \sim -100$ μm). The estimated mass remaining in the dense cores with diameters of about 25 μm is ~7 μg/cm. The initial mass of one wire is 9.5 μg/cm; hence, the dense cores contain about 70% of the initial wire mass. The rest of the wire mass is spread out toward the liner axis over a distance of ~200 μm. In the case of smeared cores, the wire mass is spread out toward the liner axis over a distance of ~400 μm. We note that a minor fraction of the plasma is spread outward: a low-density plasma extends to a distance of ~100 μm from the initial boundary of the liner.

In Fig. 5a, which shows the axial profile of the plasma surface density, one can see the axial stratification of the plasma near the core with a period of about 200 μm. At t = 70 ns after the beginning of the discharge, the surface density in these plasma jets is ~1000 μg/cm^2.

In some discharges, we observed the internal axial inhomogeneity of the core itself with a characteristic period of 20 μm (see Fig. 7). It can be seen that there are sites in which the core looks as if it is fractured in the axial direction. In these sites, the mass density is much lower and, perhaps, all the core material has already been transformed into plasma.

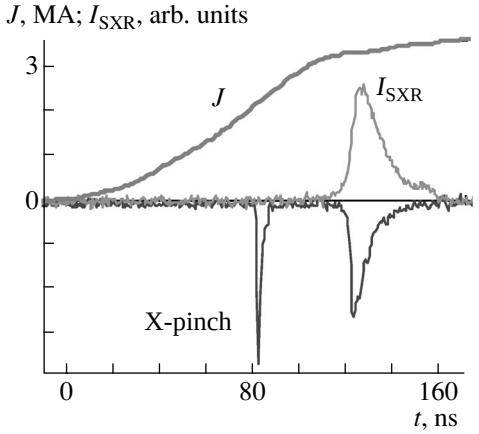

Fig. 6. Waveforms of the liner current J, the intensity of soft X-ray emission I_{SXR}, and the signal from a pin detector sensitive in the range 2–5 keV (the first spike is the X-pinch burst, and the second pulse is the Z-pinch burst) for the parameters of Fig. 5.

Fig. 7. Inner axial inhomogeneity of the core at the instant 60 ns after the beginning of the discharge. The current per wire is 30 kA. The liner with a diameter of 20 mm consists of 60 6-μm tungsten wires; the interwire distance is 1 mm.

4. DISCUSSION

The process of the wire array implosion can be outlined as follows:

Over the first several nanoseconds after the beginning of the discharge, a plasma corona arises near the wire surfaces, and the current switches from the wires to the corona [18, 19]. A further heating of the wires is primarily due heat transfer from the plasma corona. The wire array becomes a heterogeneous system consisting of the dense wire cores and a surrounding low-density plasma. The wire cores consist of a substance with a

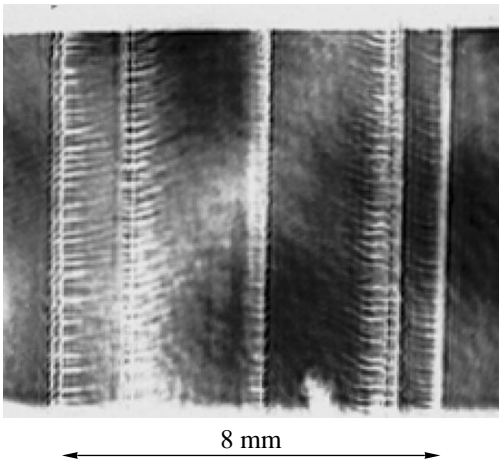

Fig. 8. Wire array shadowgraph obtained by pulsed laser probing at the instant $t = 54$ ns from the beginning of the discharge. The current per wire is 25 kA. The liner of diameter 8 mm consists of 8 6-μm tungsten wires. The characteristic period of axial modulations is 200–300 μm. The characteristic azimuthal size of the plasma jet emerging from the wire in the middle of the figure is no larger than 100 μm.

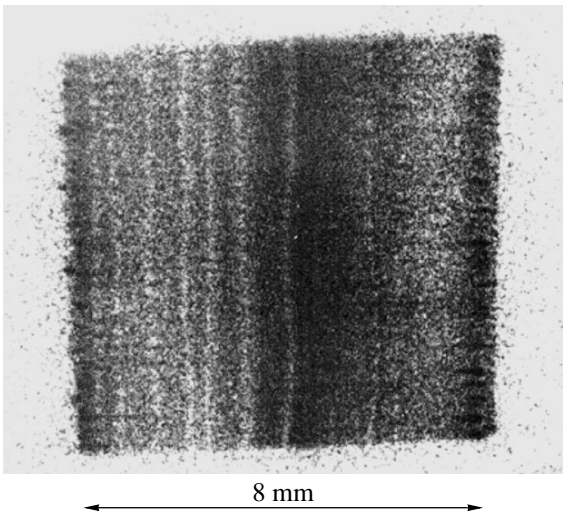

Fig. 9. X-ray frame image of the wire array 20 ns before the Z-pinch burst. The shadows in the prepinch emission are produced by the wire cores surrounded by the plasma corona.

density as high as the density of solids. Over the most part of the discharge, the cores remain in their initial positions and act as stationary plasma sources.

The Ampère force caused by the current flowing through the plasma corona surrounding the wires accelerates the plasma toward the axis of the wire array. The plasma generated on each wire acquires the form of highly nonuniform jets stretched along the radius toward the array axis.

The results obtained allow us to conclude that, by the time $t = 60$–70 ns after the beginning of the discharge, the bulk of the array mass (about 90%) is concentrated at the periphery and only a minor fraction of the low-density plasma has reached the liner axis. The plasma originated from a single wire is spread out toward the liner axis over a distance of ~400 μm. This is less than the liner interwire distance, which is equal to 1 mm. This means that it makes no sense to talk about a plasma shell that implodes as a single entity (at least at the instant $t = 70$ ns after the beginning of the discharge).

The high azimuthal and axial nonuniformity of the plasma flows allowed the authors of [20] to propose the so-called "plasma rainstorm" model. In the Angara-5-1 facility, the fragmentation of the plasma into jets was also recorded by other diagnostics [16, 21].

Figure 8 presents a wire array shadowgraph obtained by pulsed laser probing at the instant $t = 54$ ns after the beginning of the discharge, when the current per wire was 25 kA. The plasma emerging from the wires consists of plasma jets that are modulated in the axial direction and move toward the liner axis (see Fig. 8). The characteristic period of these modulations is 200–300 μm. The characteristic azimuthal size of the plasma jets is no larger than 100 μm (see the wire image in the middle of the figure).

As the array cavity is filled with hot plasma, a prepinch is formed well before the final stage of implosion. The prepinch and the plasma jets are both sources of soft X rays. The cold cores and the plasma corona surrounding them produce shadows in radiation from the prepinch and the plasma jets. Figure 9 presents a shadowgraph of a wire array in the course of implosion. The array consisted of 32 8-μm tungsten wires. The shadows are seen in radiation with photon energies from 0.1 to 1 keV. For this reason, the shadow size is significantly larger than that observed when an X-pinch is used as a radiation source. In different shadowgraphs, the shadow size varies in the range 100–400 μm. Shadows with such dimensions are produced by the plasma surrounding the dense cores. Similar shadows are also seen in the time-integrated X-ray images of an imploding wire liner [21]. We note that the shadows are clearly seen at the left of Fig. 9, whereas at the right, they are not so pronounced. This fact indicates that the wires at the right in Fig. 9 have evaporated to greater extent than those at the left. This may be explained in the same way as in the backlighting experiments (see Fig. 5), namely, by the nonuniformity of the liner current and plasma production.

To determine the fraction of the liner mass that remains at the liner periphery at the instant of the Z-pinch burst (approximately within 100–120 ns after the beginning of the discharge), one needs to either employ other diagnostics (such as laser interferometry [22]) or to shift the X-pinch burst closer in time to the Z-pinch burst.

5. CONCLUSIONS

Thus, the results of X-ray backlighting of a wire array at the 70th nanosecond after the beginning of the discharge can be formulated as follows:

(i) There are dense wire cores with masses of ~70% of the initial wire mass. The rest of the core mass is spread out toward the lines axis over a distance of ~200 μm.

(ii) The diameters of the dense cores are about three times the initial wire diameter. The substance density in the expanded cores is at least one order of magnitude lower than the initial density of the cold tungsten.

(iii) Besides the dense cores, there are also smeared cores that have evaporated to a much greater extent. Their material is spread out toward the axis over a distance of ~400 μm. This fact indicates the nonuniformity of the plasma production and, perhaps, of the liner current.

(iv) The radial size of the region occupied by the material evaporated from the wires is less than the interwire distance.

(v) Outside the liner, the low-density plasma extends to a distance of ~100 μm.

(vi) The plasma on the inner side of the cores is stratified in the axial direction with a period of 200 μm.

(vii) An axial inhomogeneity with a characteristic scale length of 20 μm is observed inside the cores.

REFERENCES

1. M. B. Bekhtev, V. D. Vikharev, S. V. Zakharov, *et al.*, Zh. Éksp. Teor. Fiz. **95**, 1653 (1989) [Sov. Phys. JETP **68**, 955 (1989)].
2. I. K. Aĭvazov, M. B. Bekhtev, V. V. Bulan, *et al.*, Fiz. Plazmy **16**, 645 (1990) [Sov. J. Plasma Phys. **16**, 373 (1990)].
3. T. W. L. Sanford, B. M. Marder, R. B. Spielman, *et al.*, Phys. Rev. Lett. **77**, 5063 (1996).
4. R. B. Spielman, C. Deeney, G. A. Chandler, *et al.*, Phys. Plasmas **5**, 2105 (1998).
5. S. V. Lebedev, F. N. Beg, S. N. Bland, *et al.*, Phys. Plasmas **8**, 3734 (2001).
6. V. V. Alexandrov, I. N. Frolov, E. V. Grabovsky, *et al.*, IEEE Trans. Plasma Sci. **30**, 559 (2002).
7. M. H. Key, P. T. Rumsby, R. G. Evans, *et al.*, Phys. Rev. Lett. **45**, 1801 (1980).
8. D. T. Attwood, IEEE J. Quantum Electron. **14**, 909 (1978).
9. S. V. Lebedev, F. N. Beg, S. A. Pikuz, *et al.*, Phys. Rev. Lett. **85**, 98 (2000).
10. S. M. Zakharov, G. V. Ivanenkov, A. A. Kolomenskiĭ, *et al.*, Pis'ma Zh. Tekh. Fiz. **9**, 1192 (1983) [Sov. Tech. Phys. Lett. **9**, 512 (1983)].
11. E. Grabovsky, K. Mitrofanov, G. Oleinik, *et al.*, in *Proceedings of the European Conference on Advanced Diagnostics for Magnetic and Inertial Fusion, Varenna, 2001*, Ed. by P. E. Stott *et al*. (Kluwer, New York, 2001), p. 419.
12. V. V. Alexandrov, M. V. Fedulov, I. N. Frolov, *et al.*, in *Proceedings of the 5th International Conference on Dense Z-Pinches, Albuquerque, 2002*, p. 91.
13. G. S. Volkov, E. V. Grabovskiĭ, I. Yu. Porofeev, *et al.*, Preprint No. 0104A (Troitsk Institute for Innovation and Fusion Research, Troitsk, 2003).
14. V. V. Gavrilov, Doctoral Dissertation (Troitsk, 1999).
15. Z. A. Al'bikov, V. P. Belik, S. V. Bobashev, *et al.*, *Plasma Diagnostics*, Ed. by M. I. Pergament (Énergoatomizdat, Moscow, 1989).
16. A. Alexandrov, A. Branitskii, E. V. Grabovskii, *et al.*, in *Inertial Fusion Sciences and Applications 99*, Ed. by C. Labaune, W. J. Hogan, and K. A. Tanaka (Elsevier, St. Louis, 1999), p. 591.
17. T. A. Shelkovenko, S. A. Pikuz, D. B. Sinars, *et al.*, IEEE Trans. Plasma Sci. **30**, 567 (2002).
18. A. V. Branitskii, E. V. Grabovskii, M. V. Frolov, *et al.*, in *Proceedings of the 12th International Conference on High-Power Particle Beams, Haifa, 1998*, p. 599.
19. V. V. Aleksandrov, A. V. Branitskiĭ, G. S. Volkov, *et al.*, Fiz. Plazmy **27**, 99 (2001) [Plasma Phys. Rep. **27**, 89 (2001)].
20. V. V. Aleksandrov, E. V. Grabovskiĭ, G. G. Zukakishvili, *et al.*, Zh. Éksp. Teor. Fiz. **124**, 829 (2003) [JETP **97**, 745 (2003)].
21. E. V. Grabovskiĭ, G. G. Zukakishvili, S. L. Nedoseev, *et al.*, Fiz. Plazmy **30**, 33 (2004) [Plasma Phys. Rep. **30**, 30 (2004)].
22. V. V. Aleksandrov, G. S. Volkov, E. V. Grabovskiĭ, *et al.*, Fiz. Plazmy **30** (3) (2004) (in press).

Translated by N.N. Ustinovskiĭ

Plasma Physics Reports, Vol. 30, No. 2, 2004, pp. 128–135. Translated from Fizika Plazmy, Vol. 30, No. 2, 2004, pp. 147–154.

PLASMA DIAGNOSTICS

Development of the Concept of Charge-Exchange Recombination Spectroscopy for ITER

S. N. Tugarinov*, I. L. Beĭgman, L. A. Vaĭnshteĭn**, V. N. Dokuka*, A. V. Krasil'nikov*, N. N. Naumenko***, I. Yu. Tolstikhina**, and R. R. Khaĭrutdinov***

** Troitsk Institute for Innovation and Fusion Research, Troitsk, Moscow oblast, 142190 Russia*

*** Lebedev Physical Institute, Russian Academy of Sciences, Leninskiĭ pr. 53, Moscow, 119991 Russia*

**** Institute of Molecular and Atomic Physics, Belarussian Academy of Sciences, pr. F. Scoriny 70, Minsk, 220072 Belarus*

Received October 8, 2003

Abstract—Charge-exchange recombination spectroscopy under ITER conditions is numerically simulated using the DINA code. The code allows one to calculate the attenuation of neutral beams in plasma, the intensity of atomic emission and emission from the ions produced by charge exchange with the neutral beam, and the intensity ratio between the emission related to charge exchange and the background continuum plasma emission. The cross sections for atom–ion interactions in plasma are calculated, and the excitation rates of spectral transitions in hydrogen-like impurity ions are determined. The measurement scheme and the main parameters of the spectrometer proposed for charge-exchange recombination diagnostics in ITER are described. © *2004 MAIK "Nauka/Interperiodica".*

1. INTRODUCTION

ITER is an international project for the development of a tokamak reactor through the joint efforts of scientists and engineers from a number of countries, including Russia. The main goal of the project is to demonstrate the feasibility of achieving controlled self-sustained D–T fusion reaction with an output power exceeding the input. The ITER project will not only integrate all the control and diagnostic systems operating in existing tokamaks, but also implement conceptually new diagnostics that have never been used before (e.g., the "helium ash" diagnostics). The basic parameters of ITER, as well as the main diagnostic systems involved, are described in [1].

The active charge-exchange recombination spectroscopy (CXRS) technique, which uses diagnostic or heating neutral atomic beams, is employed in almost all of the existing tokamaks [2]. The CXRS technique allows one to measure the most important parameters of plasmas, such as the ion temperature profile, the poloidal and toroidal rotation rate profiles, and the concentration and distribution of light impurities inside the plasma column. One of the most challenging problems of the CXRS diagnostics in the ITER system is to study the time behavior and distribution of the helium ash produced in the plasma column.

In order to extrapolate the CXRS diagnostics to the ITER scale, we carried out simulations with the DINA code, which allows one to calculate the attenuation of the diagnostic beam in plasma, the intensity of atomic emission and emission from the ions produced by charge exchange with the neutral beam, the intensity ratio between the charge-exchange emission and the background spontaneous plasma emission. The parameters of the diagnostic beam used in our calculations were taken from the literature on the ITER project [3]. The plasma parameters were varied depending on the possible operating scenarios. The signal-to-noise ratio was calculated for a definite experimental configuration with certain parameters of the detecting and recording facilities, the light collection and transmission system, and the spectral diagnostics.

In this study, we calculate the cross sections for the interaction between the diagnostic beam and plasma ions, as well as the excitation rates of the spectral transitions in hydrogen-like impurity ions.

The simulation results show that the CXRS diagnostics can be used to determine the helium ash concentration, the ion temperature profile, the concentration of light impurities, and the plasma rotation velocity in ITER.

2. THE BASIC PHYSICS AND TASKS OF CHARGE-EXCHANGE RECOMBINATION SPECTROSCOPY

The basic physics of the CXRS diagnostics can be outlined as follows: When a neutral atomic beam is injected into a plasma, an intense charge-exchange reaction between the beam atoms and the plasma ions takes place within the region occupied by the beam:

$$H^0 + A^{z+} \Rightarrow H^+ + A^{*(z-1)+}. \quad (1)$$

Since the atoms of the working gas and light impurities in the plasma core are fully ionized, this reaction yields

1063-780X/04/3002-0128$26.00 © 2004 MAIK "Nauka/Interperiodica"

an excited hydrogen-like ion, which then loses its excitation by emitting a photon. Radiative transitions with $\Delta n = 1$ have maximum probability. For high-lying levels, such transitions are accompanied by the emission of visible radiation. The lines that are most frequently used in CXRS measurements are the following:

HI (n = 3–2) 656.3 nm, HeII (n = 4–3) 468.6 nm, BeIV (n = 6–5) 465.8 nm, CVI (n = 8–7) 529.1 nm, OVIII (n = 10–9) 606.8 nm.

The ion temperature and the plasma rotation velocity are determined from the Doppler broadening and the shift of the spectral lines, while the absolute intensities of the lines give the impurity densities.

The relationship between the line intensity and the density of the corresponding impurity can be written as

$$B_\lambda = 1/4\pi \sum_{i=1}^{m} \langle \delta v \rangle^{\lambda i} \int N_z N_i dl, \quad (2)$$

where $\langle \delta v \rangle^{\lambda i}$ is the excitation rate of a transition with a wavelength λ due to the interaction with the ith component of the neutral beam, N_z is the density of nuclei of a given impurity species, and N_i is the density of atoms of the ith beam component.

The integral is taken along the line of sight within the region occupied by the neutral beam.

3. CALCULATION OF THE ATOMIC BEAM ATTENUATION AND THE SPECTRAL-LINE AND CONTINUUM INTENSITIES

Let a neutral beam be injected normally to the boundary of the plasma column. We assume the transverse profile of the beam power density to be Gaussian and to retain its shape as the beam propagates through the plasma.

The beam attenuation can be estimated in terms of a thin-beam model, which implies that the beam diameter is much less than the plasma dimensions. In this case, it is sufficient to determine the power density at the beam axis $P_0(r)$. The power density $P_0(r)$ was calculated for the projected ITER parameters: the major radius of the torus is R = 6.20 m, the minor radius of the plasma column (in horizontal direction) is a = 2.0 m, and the elongation is K = 1.85. The parameters of the diagnostic beam were taken from [3]: E_{at} = 100 keV, the beam size is 0.3×0.3 m, and the equivalent current density at the beam axis is 600 A/m^2.

To increase the signal-to-noise ratio, the light should be gathered from the central part of the diagnostic beam (from an area of about 0.1×0.1 m^2), where the current density is maximum.

The plasma density profile was assumed to be flat with an electron density of 7.5×10^{19}, 10×10^{19}, and 14×10^{19} m^{-3}, and the temperature profile was assumed to be parabolic with the central temperature $T_e = T_i$ = 15 keV. The concentrations of the plasma components (in terms of the electron density n_e) were taken to be constant over the entire cross section of the plasma column: $n_{T+D} = 0.77\, n_e$, $n_{He} = 0.04\, n_e$, $n_c = 0.012\, n_e$, and $n_{Be} = 0.02\, n_e$. Such a plasma composition corresponds to the effective ion charge number z_{eff} = 1.7, which is quite reasonable under the ITER operating conditions.

All the curves are plotted as functions of the major radius R. The plasma column axis corresponds to the major radius R = 6.3 m and the minor radius r = 0. The outer boundary of the vertically elongated plasma column corresponds to R = 8.3 m and r = 2.0 m.

Numerical simulations were performed for the HeII 468.6-nm (n = 4–3), BeIV 465.8-nm (n = 6–5), and CVI 529.1-nm (n = 8–7) spectral lines.

The attenuation of the beam over a distance dr can be expressed as

$$dP_0(r) = -\sigma_s^{(N)} n_e P_0(r) dr, \quad (3)$$

where the total attenuation cross section $\sigma_s^{(N)}$ is determined by formula (4) from [4]:

$$\sigma_s^{(N)} = \frac{\exp S_1(E_0, n_e, T_e)}{E_0} \times \left[1 + \sum_{q=1}^{N} c_q z_q (z_q - 1) S_{z_q}(E_0, n_e, T_e) \right]. \quad (4)$$

The function $S_1(E_0, n_e, T_e)/E_0$ describes the attenuation of a neutral beam with a particle energy E_0 in a hydrogen plasma, while the function S_{z_q} describes the attenuation by an impurity with a charge z_q and concentration c_q (in terms of the electron density n_e). The calculations also take into consideration the additional attenuation due to the excitation of atoms of the diagnostic beam in plasma.

Figure 1 shows the attenuation of a beam in a pure D–T plasma (curve *1*) and a plasma with the impurity composition specified above (curve *2*). In both cases, the electron density is $n_e = 7.5 \times 10^{19}$ m^{-3}. It can be seen that the impurities contribute substantially to the attenuation and, thus, must be taken into account. The attenuation also depends significantly on the absolute value of the plasma density (as an exponential function). This effect becomes especially pronounced for long path lengths of the beam in plasma (i.e., for the central region of the plasma column). Figure 2 shows the beam attenuation for the three different plasma densities: 7.5×10^{19} m^{-3} (curve *1*), 10×10^{19} m^{-3} (curve *2*), and 14×10^{19} m^{-3} (curve *3*).

Since the ITER-FEAT diagnostic beam is monoenergetic, formula (2) for the photon flux emitted by the excited impurity atoms with the effective ion charge

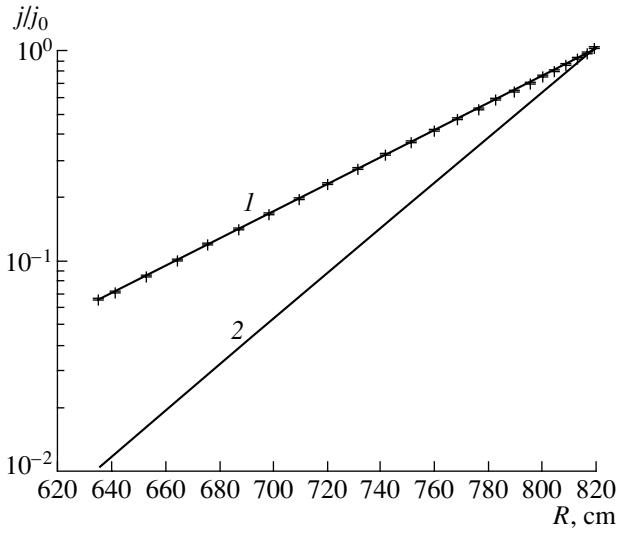

Fig. 1. Attenuation of the current density j of the beam passed through (*1*) a pure D–T plasma and (*2*) a plasma of the same density in the presence of impurities.

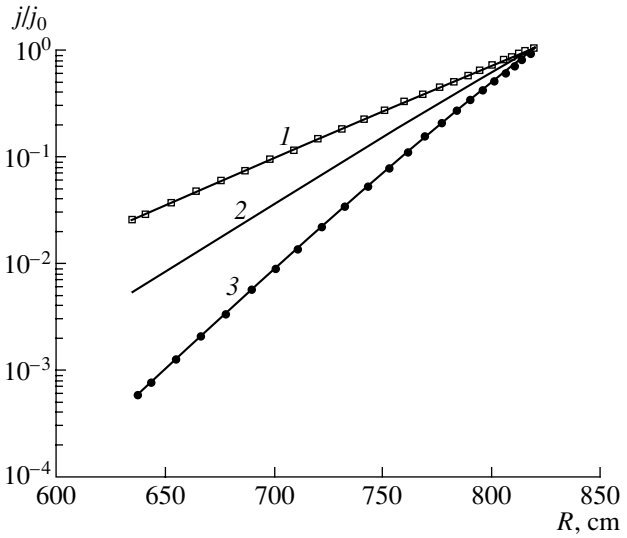

Fig. 2. Attenuation of the current density j of the beam passed through a plasma with a density of (*1*) 7.5×10^{19}, (*2*) 10×10^{19}, and (*3*) 14×10^{19} m^{-3}.

number z_q from a unit volume of the beam into a unit solid angle takes the form

$$S^0_{cx}(r) = \frac{1}{4\pi}\frac{P_0(r)}{v_0 E_0}\langle \sigma v\rangle_{z_q} c_q n_e, \quad (5)$$

where v_0 and E_0 are the velocity and energy of neutrals. The excitation rate of a given transition $\langle \sigma v\rangle_{z_q}$ depends on both the energy of the neutrals and the impurity species.

The intensity of bremsstrahlung from a unit volume into a unit solid angle within an spectral interval of 1 Å is described by formula (6) from [5]:

$$\frac{\Delta n_{\rm ff}}{\Delta\lambda} = 7.56 \times 10^{-15} g_{\rm ff}\frac{n_e^2 z_{\rm eff}}{\lambda\sqrt{T_e}}, \quad (6)$$

where $g_{\rm ff}$ is the Gaunt factor for bremsstrahlung, which takes the value 3.8 under ITER conditions. The subscript ff stands for free–free transitions. We also take into account the Doppler broadening of an impurity emission line with a wavelength λ:

$$\Delta\lambda_D = 7.75 \times 10^{-5}\lambda\sqrt{T_i/A}, \quad (7)$$

where λ is in Å, T is in eV, and A is the atomic weight of the impurity. Finally, we obtain the expression for the bremsstrahlung photon flux from a unit volume into a unit solid angle within a spectral interval equal to the line width:

$$S_{\rm ff}(r) = \frac{n_{\rm ff}}{\Delta\lambda}\Delta\lambda_D. \quad (8)$$

4. CALCULATION OF THE INTERACTION CROSS SECTIONS AND THE EXCITATION RATES OF SPECTRAL TRANSITIONS

The main mechanism for excitation is the charge exchange between the impurity ions and the beam atoms via reaction (1), resulting in the formation of excited impurity ions. Since most of the impurity ions are bare nuclei, the resulting ions are hydrogen-like. At the same time, the interaction of the high-energy beam with plasma gives rise to neutral deuterium and tritium atoms with the temperature equal to the plasma temperature. This secondary neutral component, which is known as a "halo," also participates in the charge-exchange process and additionally contributes to the formation of excited impurity ions.

The charge exchange cross sections for the collisions of the 100-keV hydrogen beam atoms with helium (He^{2+}), beryllium (Be^{4+}), and carbon (C^{6+}) nuclei were taken from the results of calculations using the CAPTURE code [6] and the results of [7]. In particular, cross sections for charge exchange into states with n = 1–6 were obtained by the strong coupling method [7]. For $n > 6$, the normalized charge-exchange cross sections were calculated using the CAPTURE code in the Brinkman–Kramers approximation.

Taking into account the branching ratio and the contribution of the cascade population from the highly excited states generated during the charge-exchange process, we can write the $n \longrightarrow n'$ excitation rate in the form

$$v\sigma_{n-n'} = \frac{A_{n-n'}}{A_n} v \sum_{m=0}^{N} c_{mn}\sigma_{n+m}, \quad (9)$$

Table 1. Excitation rates for a 100-keV hydrogen beam

Element	Transition	N	$\nu\sigma$, 10^{-14} m^3/s	$\nu\sigma$, 10^{-14} m^3/s (ADAS)
He^+	4–3	15	0.102	0.088
Be^{3+}	6–5	15	0.338	0.354
C^{5+}	8–7	15	0.609	0.688

Table 2. Direct charge-exchange rate for a 100-keV hydrogen beam and the total excitation rate for three energies of the secondary thermal ions

Element	Transition	$\nu\sigma_d$, 10^{-14} m^3/s	$\nu\sigma_t$, 10^{-14} m^3/s		
			10 keV/nucleon	20 keV/nucleon	25 keV/nucleon
He^+	4–3	0.102	0.11	0.13	0.15
Be^{3+}	6–5	0.338	0.34	0.34	0.37
C^{5+}	8–7	0.609	0.61	0.61	0.62

where $A_{n-n'}$ is the probability of the radiative transition $n-n'$; A_n is the total probability of radiative decay from the nth level; σ_{n+m} is the cross section for charge exchange into states with the principal quantum numbers $n+m$; and c_{mn} are the Seaton cascade matrix elements, which define the relative probability of radiative decay from the $(n+m)$th level to the nth level. In a rarified plasma, the upper summation limit N should be chosen to ensure the convergence of the sum in Eq. (9). In practice, $N \approx 15$ turns out to be quite sufficient. In real plasmas, however, the highly excited levels do not contribute to the population of the nth level because their ionization rate exceeds the radiative decay probability. The results of the calculations are listed in Table 1.

For the sake of comparison, the last column presents the excitation rates taken from the ADAS database for the same transitions. It can be seen that the ADAS data and the results of our calculations are in good agreement.

Along with the direct excitation of impurity ions, a secondary process is also possible in which the neutral deuterium and tritium atoms generated via the resonant charge exchange of the beam atoms with the plasma ions give rise to excited impurity ions. This phenomenon is known as the "halo effect." Thus, the total excitation rate $\nu\sigma_t(n-n')$ with allowance for the halo effect is equal to

$$v\sigma_t(n-n') = v\sigma_d(n-n') + \alpha v\sigma_s(n-n'), \quad (10)$$

where $v\sigma_d(n-n')$ is the direct charge-exchange rate, $v\sigma_s(n-n')$ is the secondary charge-exchange rate at thermal energies, and α is the impurity factor (the ratio of the density of the secondary neutral deuterium and tritium atoms to the atomic density of the diagnostic beam). Ignoring the diffusion of the secondary atoms from the beam–plasma interaction region, the factor α can be found from the equilibrium condition between the generation and ionization of the secondary atoms:

$$\alpha = v\sigma_r/\langle v\sigma_i\rangle \approx 0.15, \quad (11)$$

where $v\sigma_r \approx 4.5 \times 10^{-15}$ m^3/s is the resonant charge-exchange rate and $\langle v\sigma_i\rangle \approx 3 \times 10^{-14}$ m^3/s is the ionization rate. The total excitation rates calculated for three energies of the secondary thermal atoms are listed in Table 2.

It can be seen from Table 2 that the halo effect manifests itself only at high temperatures and is most pronounced for light ions such as He^+.

5. APPLICATION OF THE DIAGNOSTICS TO ITER AND THE CALCULATION OF THE SIGNAL-TO-NOISE RATIO

The poloidal cross section of the ITER tokamak and the arrangement of the diagnostics are shown in Fig. 3. The diagnostic beam is injected horizontally, in the equatorial plane of the tokamak, normally to the toroidal field. A scheme of vertical observation from the upper port was chosen in view of a number of advantages as compared to the other possible versions. One of the benefits is the minimal length of the observation chord inside the plasma volume; this ensures the highest signal-to-noise ratio. Here, the useful signal is radiation related to charge exchange with the neutral beam, while the background noise is the bremsstrahlung continuum.

We propose to perform measurements only for the outer half of the plasma column, from the point at which the bean enters the plasma to the center of the column, since the beam attenuation is smaller here than in the inner half of the column. The observation scheme was chosen so as to prevent the observation chords from crossing the vicinity of the divertor. Otherwise, one could hardly measure the useful signal against the

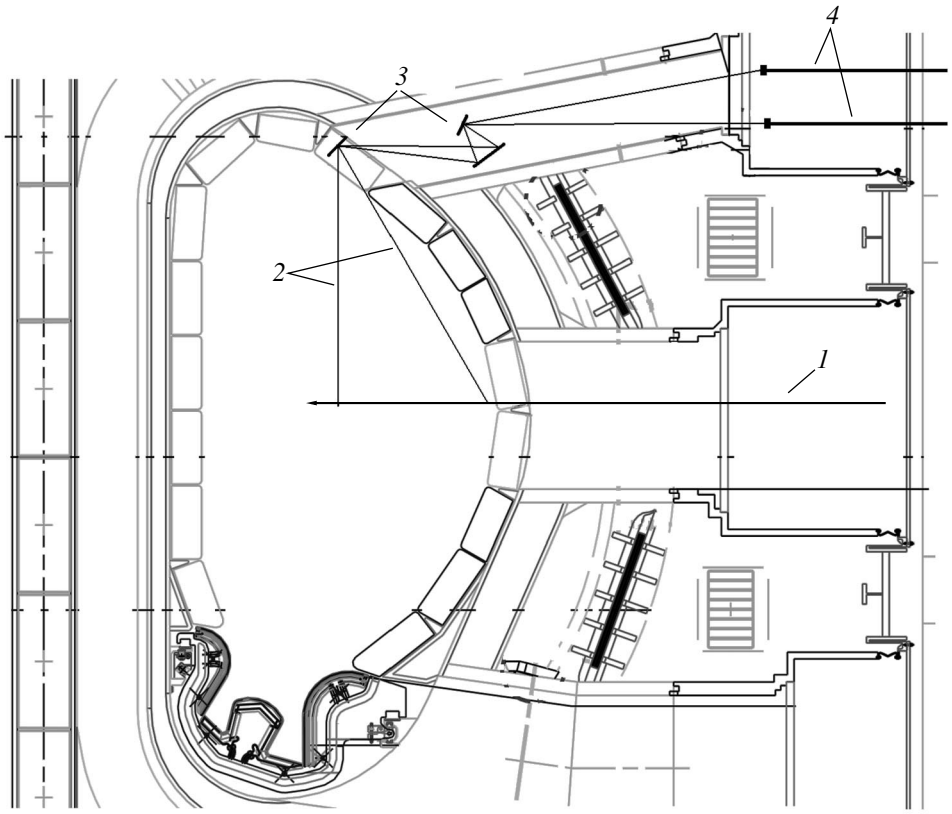

Fig. 3. Poloidal cross section of ITER and the arrangement of the diagnostics: (*1*) diagnostic atomic beam, (*2*) observation chords, (*3*) light-gathering mirrors, and (*4*) optical fibers transferring light to a spectrometer.

background radiation because of the intense molecular continuum arising in the divertor.

The radiation emitted from the plasma is output through a window in the shielding blanket. On the output window, the photon flux density of radiation emitted from the volume $\delta r \Delta z \delta t$ inside the beam due to the charge-exchange excitation of the impurity ions is determined by the formula

$$I_{cx} = \Omega_\alpha S^0_{cx}(r_\alpha) G(\sigma) \delta r \Delta z \delta t \qquad (12)$$

and the photon flux density of continuum integrated along the observation chord is given by the formula

$$I_{ff} = \int S_{ff}(r)\Omega(r)dV \cong \Omega_\alpha S_{ff}(r_\alpha)\sin\alpha \Delta p_\alpha \Delta r \delta t. \qquad (13)$$

Here, Ω_α is the solid angle at which the unit area of the output window is seen from the observation point with the radius r_α, $G(\sigma)$ is the Gaussian factor taking into account the transverse profile of the beam,

$$G(\sigma) = \frac{\pi\sigma^2}{\Delta z \delta t}\mathrm{erf}\left(\frac{\Delta z}{2\sigma}\right)\mathrm{erf}\left(\frac{\delta t}{2\sigma}\right), \qquad (14)$$

$\delta r \times \delta t$ is the viewed area at the radius r_α, α is the angle between the observation chord and the horizontal plane; and Δp_α is the length of the observation chord.

Expression (13) is derived under the assumption that $S_{ff}(r) \cong S_{ff}(r_\alpha)$; i.e., the intensity of bremsstrahlung is constant along the observation chord. This assumption seems reasonable because the electron density profile is taken to be flat.

It was shown in [6, 7] that the bremsstrahlung intensity integrated along the observation chord appreciably exceeds the charge-exchange signal at nearly all the values of the small radius r over the range of 0 to 200 cm (which agrees with the results of our simulations; see Figs. 4–6 and their descriptions below). In this situation, a useful signal can be separated from the dominating background with the help of a well-known method based on the 100% periodic amplitude modulation of the injected atomic beam. Usually, a square-wave modulation is applied. A CCD detector is synchronized with the beam modulation; i.e., one shot is taken when the beam is switched on and the next one catches the beam when it is switched off (the so-called lock-in detection). Subtracting the spectra thus obtained, one can separate the desired radiation related to charge exchange with the neutral beam.

Under the conditions of beam modulation and lock-in detection, the measurement accuracy is fundamentally limited by the continuum fluctuations. Therefore,

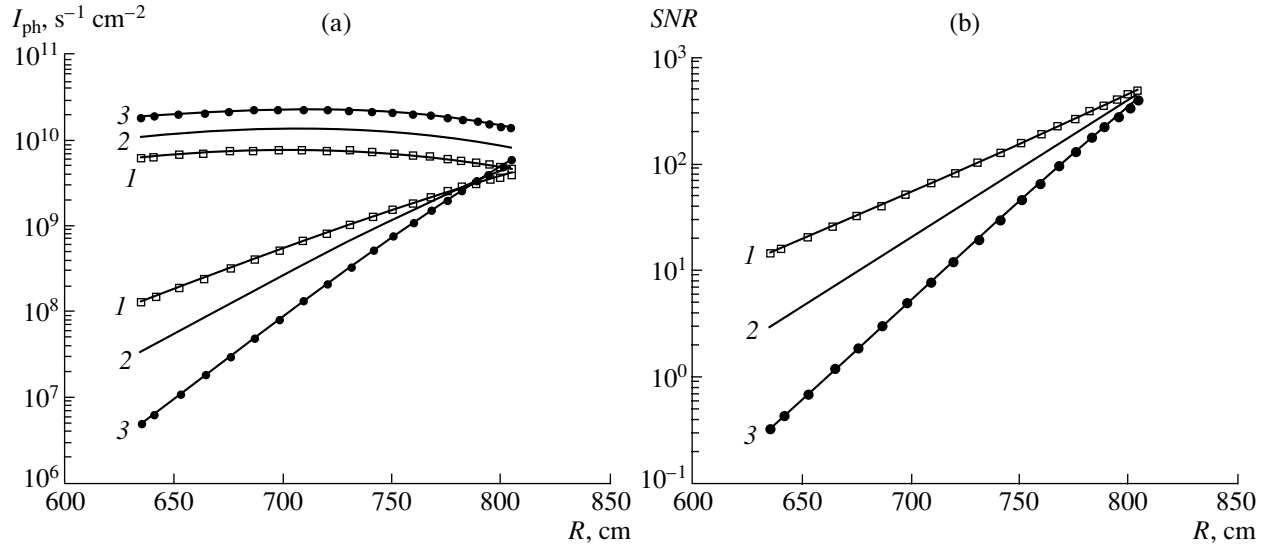

Fig. 4. (a) Photon flux densities of the HeII 468.6-nm charge-exchange line (on bottom) and the background continuum (on top), both integrated along the observation chord, vs. major radius R and (b) the radial profiles of the signal-to-noise ratio SNR calculated by formula (16) for plasma densities of (*1*) 7.5×10^{19}, (*2*) 10×10^{19}, and (*3*) 14×10^{19} m^{-3}.

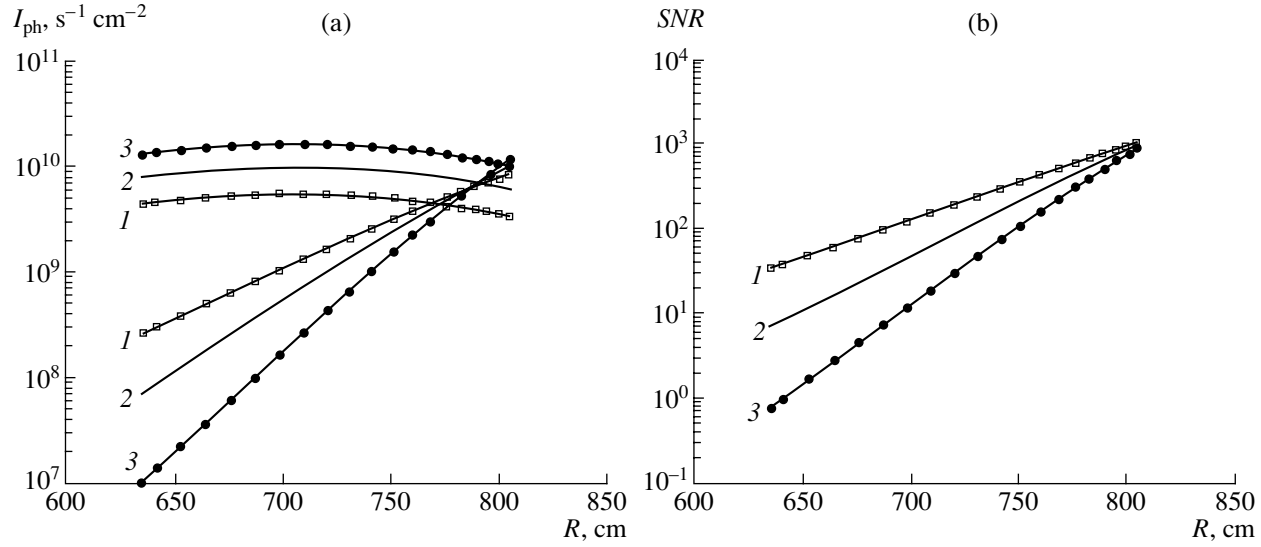

Fig. 5. (a) Photon flux densities of the BeIV 465.8-nm charge-exchange line (at bottom) and the background continuum (at top), both integrated along the observation chord, vs. major radius R and (b) the radial profiles of the signal-to-noise ratio SNR calculated by formula (16) for plasma densities of (*1*) 7.5×10^{19}, (*2*) 10×10^{19}, and (*3*) 14×10^{19} m^{-3}.

the signal-to-noise ratio SNR can be calculated by the formula [8–10]

$$SNR = \frac{I'_{cx}\sqrt{t}}{\sqrt{2(2I'_{ff} + I'_{cx})}}, \qquad (15)$$

where I'_{cx} and I'_{ff} are the numbers of photons per unit time that are brought onto the detector from the useful signal (due to charge exchange) and from the bremsstrahlung continuum, respectively, and t is the time of the signal integration.

Taking into account Eqs. (12) and (13), we can write expression (15) in the form

$$SNR = \left[\frac{\Omega_\alpha S^0_{cx}(r_\alpha)\delta r \Delta z \delta t \eta \Delta\tau}{2\left(2\frac{S_{ff}(r_\alpha)}{S^0_{cx}(r_\alpha)}\frac{\Delta p_\alpha \sin\alpha}{G(\alpha)\Delta z} + 1\right)}\right]^{1/2}. \qquad (16)$$

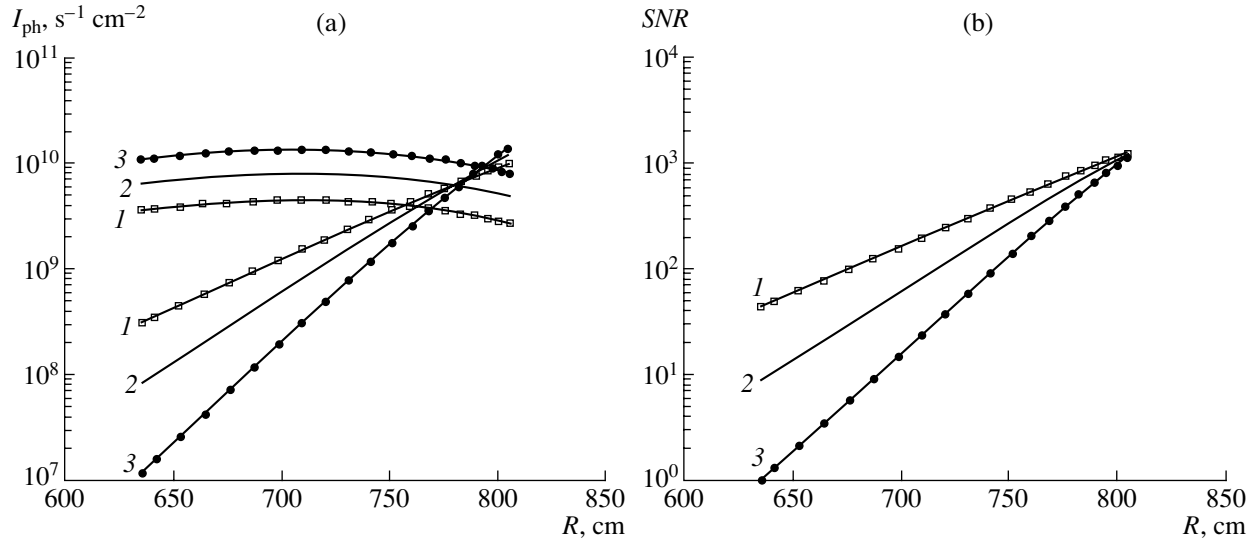

Fig. 6. (a) Photon flux densities of the CVI 529.1-nm charge-exchange line (at bottom) and the background continuum (at top), both integrated along the observation chord, vs. major radius *R* and (b) the radial profiles of the signal-to-noise ratio *SNR* calculated by formula (16) for plasma densities of (*1*) 7.5×10^{19}, (*2*) 10×10^{19}, and (*3*) 14×10^{19} m^{-3}.

The factor η in Eq. (16) takes into account the losses related to reflection and absorption in the optical elements, the limitation of the light flux by the entrance slit of the spectrometer, and the efficiency of the detection system.

Formula (16) is an analog of the expression for *SNR* in [7].

6. CHOICE AND CALCULATION OF THE OPTICAL SCHEME

The optical scheme is chosen to gather all the radiation that passes through the output aperture (the window in the blanket). In our calculation, the window diameter is taken to be 50 mm. Then, the light beam passes without geometrical loss through the light guides and arrives at the entrance slit of the spectrometer. Depending on the required spectral resolution and the corresponding slit width, the light beam is partially cut off by the entrance slit, which is taken into account by the factor η introduced above.

In the case of a cylindrically symmetrical optical system, the Lagrange–Helmholtz formula takes the form

$$n_1 s_1 \Omega_1 = n_2 s_2 \Omega_2, \qquad (17)$$

where $n_{1,2}$ are the refractive indices of the media, $s_{1,2}$ are the sizes of the source and its image, and $\Omega_{1,2}$ are the light-gathering solid angles.

The optical scheme is designed with provision made for using a special high-resolution wide-aperture device that was developed in the Troitsk Institute for Innovation and Fusion Research for high-precision measurements of the spectral lines. The main parameters of this device are as follows: the operating spectral range is 200–800 nm (for a stigmatic image), the f-ratio is 3, the inverse linear dispersion is 2.5–3.0 Å/mm, and the instrumental width at a normal slit width is 20–25 μm.

7. RESULTS, DISCUSSION, AND CONCLUSIONS

Figure 4a shows photon flux densities of the HeII 468.6-nm charge-exchange line and the background continuum (both integrated along the observation chord) versus the major radius *R* for three values of the plasma density: 7.5×10^{19}, 10×10^{19}, and 14×10^{19} m^{-3}. The radial profiles of the signal-to-noise ratio *SNR* calculated by formula (16) for the same plasma densities are shown in Fig. 4b.

Figure 5a shows photon flux densities of the BeIV 465.8-nm charge-exchange line and the background continuum (both integrated along the observation chord) versus *R* for three values of the plasma density: 7.5×10^{19}, 10×10^{19}, and 14×10^{19} m^{-3}. The radial profiles of *SNR* calculated by formula (16) for the same plasma densities are shown in Fig. 5b.

Figure 6a shows the photon flux densities of the CVI 529.1 nm charge-exchange line and the background continuum (both integrated along the observation chord) versus *R* for three values of the plasma density: 7.5×10^{19}, 10×10^{19}, and 14×10^{19} m^{-3}. The radial profiles of *SNR* calculated by formula (16) for the same plasma densities are shown in Fig. 6b.

Active spectroscopic measurements carried out in the JET tokamak, the parameters of which are closest to those of ITER, show that, for reliable lock-in detection measurements with an accuracy of 10–20%, the signal-

to-noise ratio should be no lower than 10 [9, 10]. It follows from the radial profiles of *SNR* for HeII, BeIV, and CVI spectral lines (Figs. 4b, 5b, 6b) that the measurements of the ion temperature using the BeIV and CVI lines at a plasma density of up to 10^{20} m^{-3} may be performed along the entire outer half of the plasma column, including the center. At higher densities (of up to 1.4×10^{20} m^{-3}), the measurements can be performed in the region $r \geq a/3$. The measurements of the helium-ash density using the HeII line at plasma densities higher than 10^{20} m^{-3} are also limited to the region $r \geq a/3$.

REFERENCES

1. P. E. Stott, G. Gorini, P. Prandoni, and E. Sindoni, in *Diagnostics for Experimental Thermonuclear Fusion Reactor* (Plenum, New York, 1996).
2. R. J. Fonk, D. S. Darrow, and K. P. Jaehnig, Phys. Rev. A **29**, 3288 (1984).
3. E. D. Pietro, A. Costley, T. Inoue, *et al.*, Fusion Eng. Des. **56**, 929 (2001).
4. R. K. Janev, C. D. Boley, and D. E. Post, Nucl. Fusion **29**, 2125 (1989).
5. K. Kadota, M. Otsuka, and J. Fujita, Nucl. Fusion **20**, 209 (1980).
6. I. Yu. Tolstikhina and V. P. Shevel'ko, Kratk. Soobshch. Fiz., No. 10, 10 (2000).
7. N. Toshima and H. Tawara, NIFS-DATA **26** (1995).
8. E. S. Marmar, in *Diagnostics for Experimental Thermonuclear Fusion Reactor* (Plenum, New York, 1996), p. 281.
9. M. G. von Hellermann, W. G. F. Core, A. Howman, *et al.*, in *Diagnostics for Experimental Thermonuclear Fusion Reactor* (Plenum, New York, 1996), p. 321.
10. M. G. von Hellermann, S. Tugarinov, G. Vayakis, *et al.*, in *The Final Report on EFDA Contracts 00-558, 00-559, and 00-560, 2002* (CIT, Garching, 2002).

Translated by A. Sidorova

Plasma Physics Reports, Vol. 30, No. 2, 2004, pp. 136–142. Translated from Fizika Plazmy, Vol. 30, No. 2, 2004, pp. 155–162.

PLASMA DIAGNOSTICS

Measurements of the Plasma Radiative Loss Profile in the M-11M Tokamak with the Help of a Tangential-View AXUV Photodiode Array

A. S. Prokhorov, A. G. Alekseyev, A. M. Belov, V. B. Lazarev, and S. V. Mirnov

Troitsk Institute for Innovation and Fusion Research, Troitsk, Moscow oblast, 142190 Russia

Received July 24, 2003

Abstract—The plasma radiative loss profile in the T-11M tokamak operating with a lithium limiter was measured using a sixteen-channel absolute extreme-ultraviolet photodiode array. The field of view of the detector was set in a vertical plane tangential to the plasma column axis. The radiative loss profile was recovered by solving an inverse problem under the assumption of toroidal and poloidal symmetry of the plasma column. A stable algorithm is developed for solving the problem with this geometry, and the possible errors of the method are evaluated. The radiative loss profiles and their evolution in various tokamak regimes are derived. © *2004 MAIK "Nauka/Interperiodica".*

1. INTRODUCTION

A very important parameter of a tokamak plasma is its integral radiative loss power, which is usually monitored with the help of a wide-angle bolometer. This power is usually varied over the range 15–50% of the total heating power, depending on the impurity concentration and plasma density. From the radiative loss power, one can estimate the amount of impurities in the plasma. A more detailed analysis of the experimental data involves measurements of the radial profile of the radiative loss power in the plasma column. To provide these measurements, a sixteen-channel fast absolute extreme-ultraviolet (AXUV) photodiode array with a time resolution of 2 μs was installed in the T-11M tokamak [1]. The major axis of the pinhole camera was directed tangentially to the plasma column axis. For this reason, the radiative loss profile could not be recovered by using the conventional cylindrical Abel inversion. Instead, we elaborated a numerical method capable of solving an inverse problem under the assumption of toroidal symmetry. The method, which is conceptually analogous to the Abel inversion, was used to analyze the data obtained from the AXUV detector array in experiments with a lithium limiter in T-11M.

However, the method proposed, as well as any Abel inversion method, implies some kind of symmetry of the emission sources (toroidal symmetry in our case). This fact does not allow one to directly apply well-known Abel inversion methods to asymmetric sources. For this reason, it is rather difficult to correctly determine the radiative loss profile near the lithium limiter, because the lithium flux from the limiter introduces strong asymmetry into the distribution of the radiative loss power near the limiter. Therefore, in this study, we processed exclusively the data from the upper bolometer channels (see Section 2) for which the assumption of toroidal symmetry is valid, since the transit time of lithium ions along the torus (20–100 μs) is small compared to their expected lifetime in the T-11M plasma (≈10 ms). The temporal and spatial resolution was limited by the number and arrangement of the detector channels and also by the sampling rate of the data acquisition system (200 μm per sixteen channels). In spite of the above limitations, the data obtained are enough to fairly correctly determine the radiative loss profile in discharges for which the assumption of toroidal symmetry is valid. Possessing these data, we can infer the behavior and radiative characteristics of lithium impurity in plasma.

2. EXPERIMENTAL AND DIAGNOSTIC TECHNIQUE

Experiments with a lithium limiter were carried out in the T-11M tokamak. The major radius of the tokamak vacuum vessel was $R = 700$ mm, the minor radius was 230 mm, the effective radius of the lithium limiter (the plasma radius) was $a = 190$ mm, the central electron temperature was $T_e = 350$–400 eV, and the line-averaged electron density was $N_e = (1.5–5) \times 10^{13}$ cm^{-3}. The total discharge duration was 150 ms, whereas the duration of the steady-state phase was about 50 ms. The working gas was hydrogen, deuterium, or helium. Lithium was injected into the plasma directly from the limiter installed in the lower part of the vessel (Fig. 1). The limiter was a cylindrical metal surface covered with a 5-mm-thick capillary porous structure consisting of several metal meshes with 30-μm cells impregnated with lithium [2–4]. The limiter was equipped with a built-in electric heater. The temperature of the limiter surface was monitored by two thermocouples. The experiments were carried out at various initial limiter

1063-780X/04/3002-0136$26.00 © 2004 MAIK "Nauka/Interperiodica"

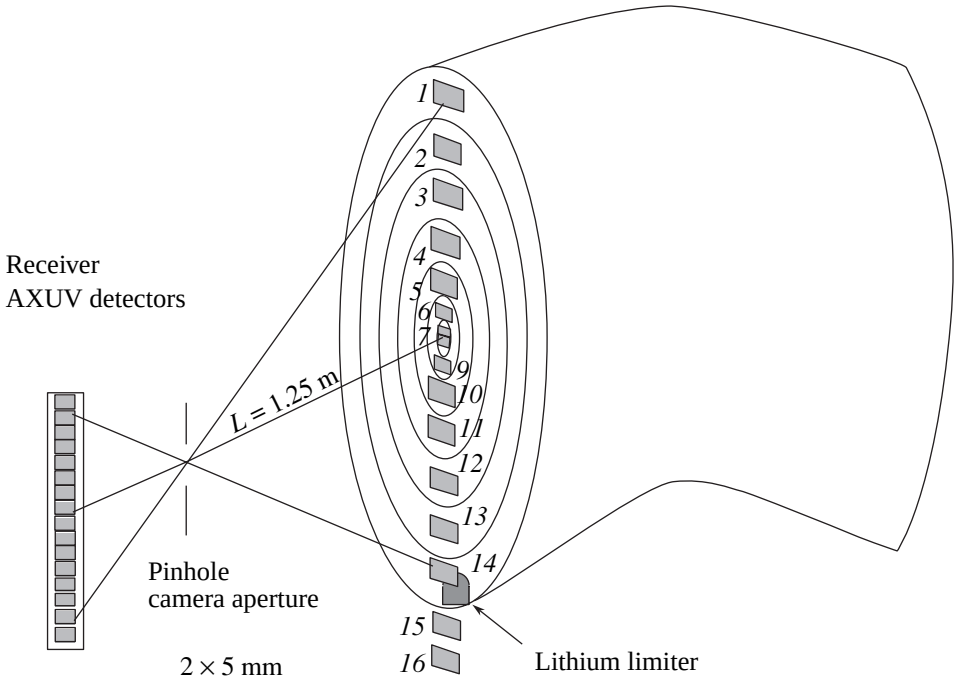

Fig. 1. Viewing geometry of the AXUV detector pinhole camera. Rectangles show the cross sections of the fields of view of the detectors in the Li limiter plane.

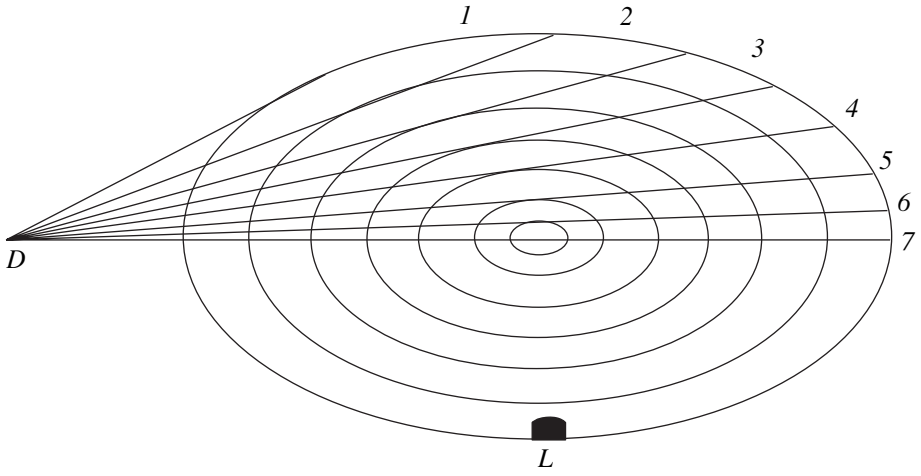

Fig. 2. Positions of the fields of view of the AXUV detectors in the vertical tangential cross section of the plasma column: (*D*) AXUV detector array and (*L*) lithium limiter.

temperatures in the range of 20–400°C. These experiments and the reasons why the tangential view was chosen are described in more detail in [2–4].

The radiative loss power was monitored with an AXUV multichannel system [1] consisting of a pinhole camera equipped with a sixteen-element AXUV array whose field of view was directed tangentially to the plasma column (Fig. 1). The detectors had a nearly uniform sensitivity in the XUV and soft X-ray spectral ranges [1]. A slit aperture (2×5 mm in size) was placed in front of the detector array. The detectors received radiation along chords nearly 5 cm in width and 2.5 cm in height in the poloidal cross section where the Li limiter is installed. The field of view of the detectors covered the total cross section of the plasma column at the limiter location, so that we were able to recover the

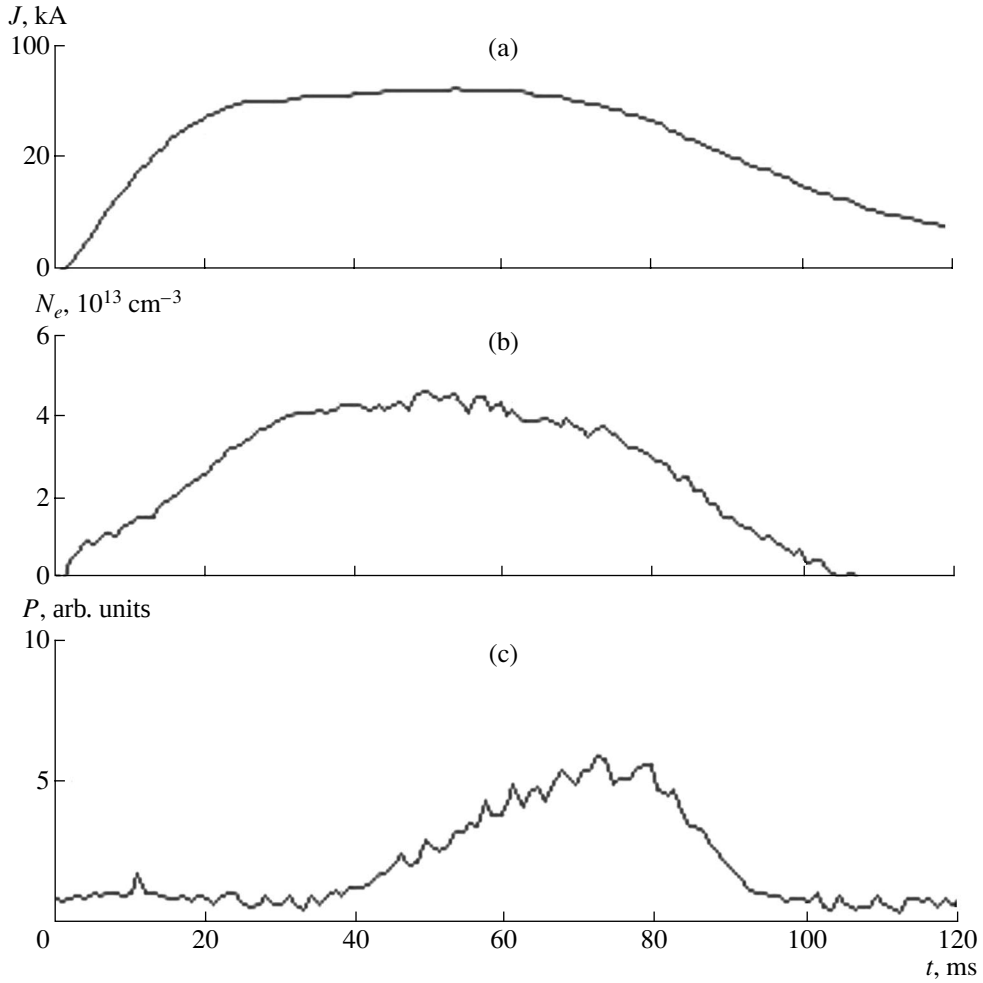

Fig. 3. Evolution of the plasma parameters in a low-density T-11M discharge (shot no. 13132): (a) plasma current J, (b) line-averaged electron density N_e, and (c) intensity P of soft X-ray emission from the plasma center.

radiative loss profile under the assumption of toroidal symmetry. The outputs of the sixteen channels were sampled successively by two simultaneously operating analog-to-digital converters. The sampling time of the entire system was 200 μs, which determined the temporal resolution of the AXUV array.

3. RECOVERY OF THE RADIATIVE LOSS PROFILE

The signal from each AXUV detector was proportional to the integral of the plasma specific emittance taken along the view axis of each channel (Fig. 1).

The recovery of the radiative loss profile in a plasma column from the data obtained with the AXUV detector array viewing in one (tangential) direction is an inverse problem that can be solved for a certain limited class of functions. In our case, we assume the toroidal symmetry of the plasma radiation profile, which is generally correct for tokamaks. We also assume that the plasma radiation power is a function of the minor radius r alone. Hence, we ignore both the Shafranov shift of the magnetic surfaces and the angular anisotropy related to MHD activity. The influence of a local perturbation produced by the lithium limiter in the lower part of the plasma column is excluded, since only seven upper channels are used in the recovering procedure. To find an approximate solution, we use the Pierce method, which results in a transformation similar to the well-known Abel inversion.

The plasma column is separated into nested toroidal layers, assuming that, in each layer, the specific emittance is constant and equal to its average value. Hence, we obtain a set of equations that relate the radiation power received by the detector array to the specific emittance in each layer. However, for this set of equations could be solved, the number of the unknown variables must be equal to the number of equations, which is determined by the number of the viewing channels. This implies that the number of layers must be equal to the number of channels.

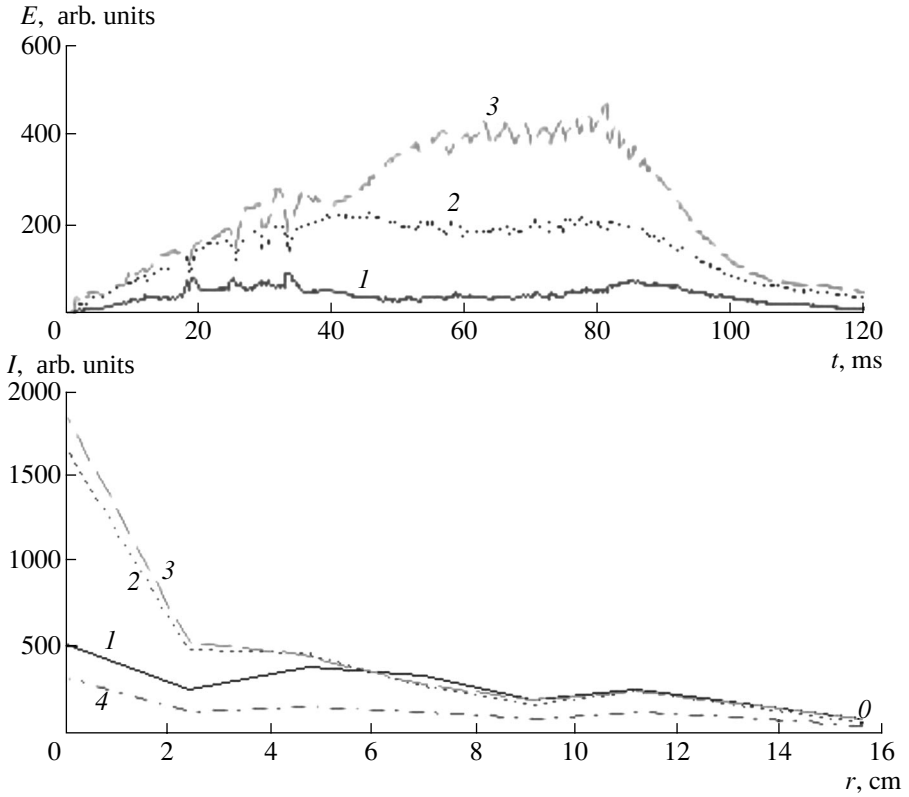

Fig. 4. (a) Raw signals from the upper channels of the AUXV detector array for a low-density discharge: (*1*) 1st, (*2*) 4th, and (*3*) 7th channels; (b) the recovered radiative loss profiles for t = (*1*) 40, (*2*) 60, (*3*) 80 and (*4*) 100 ms.

As a result, we arrive at the following set of ordinary algebraic equations:

$$\int_0^L I(l)dl = \sum I_i l_i. \qquad (1)$$

Here, $I(l)$ is the radiation power received from a point with the coordinate l along the channel, L is the channel length, I_i is the specific emittance in the ith layer, and l_i is the length of the viewing chord crossing the ith layer.

We assume that the volume of each layer watched by a channel is approximately proportional to the length of the corresponding viewing chord. Thus, the problem is reduced to calculating I_i. However, in this approach, we encounter the problem of determining the layer boundaries.

The thicknesses of the layers are determined by the positions of the viewing chords. The layer thicknesses are chosen such that, when moving from the periphery to the center, each next chord crosses only one more layer in comparison with the preceding chord. Moreover, the inner (closer to the plasma column axis) boundary of the field of view of each detector coincides with the layer boundary. Figure 2 shows the tangential cross section of the plasma column separated into layers as was described above.

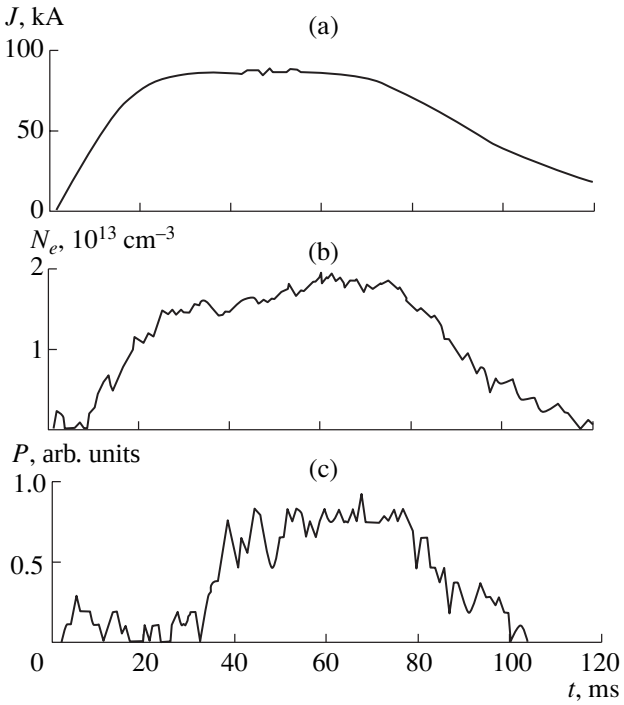

Fig. 5. Evolution of the plasma parameters in a high-density T-11M discharge (shot no. 13100): (a) plasma current J, (b) line-averaged electron density N_e, and (c) intensity of soft X-ray emission from the central region of the plasma column P.

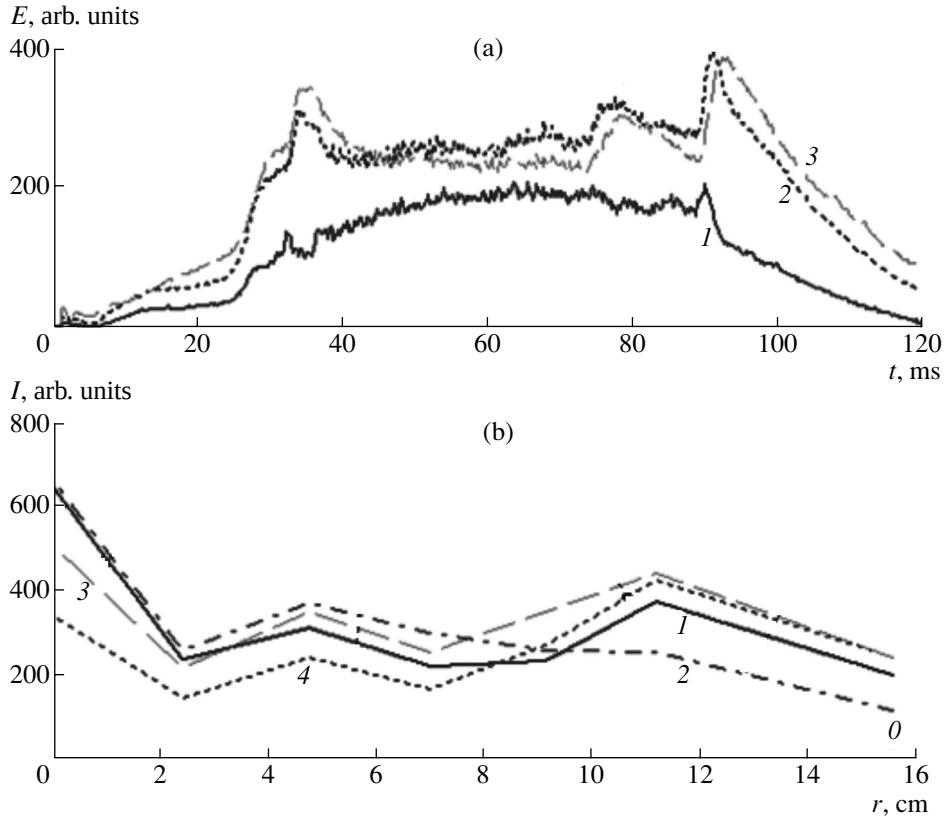

Fig. 6. (a) Raw signals from the upper channels of the AXUV detector array for a high-density discharge: (*1*) 1st, (*2*) 4th, and (*3*) 7th channels; (b) the recovered radiative loss profiles for t = (*1*) 40, (*2*) 60, (*3*) 80 and (*4*) 100 ms.

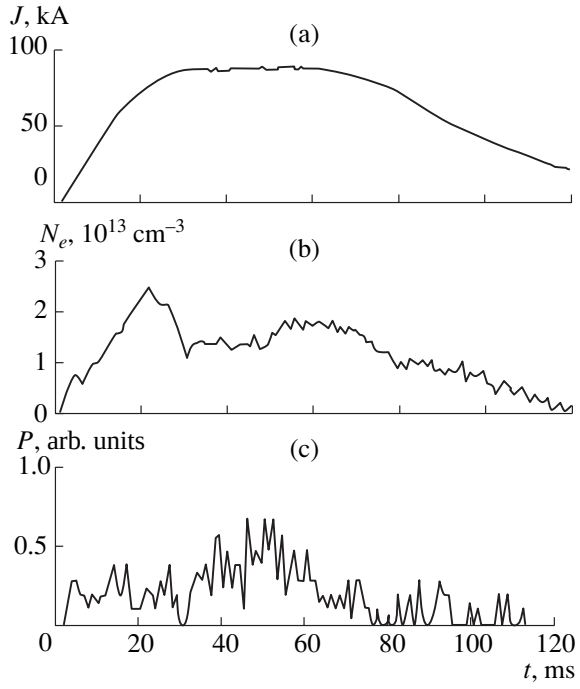

Fig. 7. Evolution of the plasma parameters in a T-11M discharge with a negatively biased lithium limiter (shot no. 13119): (a) plasma current J, (b) line-averaged electron density N_e, and (c) intensity P of soft X-ray emission from the plasma center.

As a result, the set of equations takes the form

$$\begin{aligned} 75.45I_1 &= E_1, \\ 63.2I_1 + 26.06I_2 &= E_2, \\ &\cdots\cdots \\ 23.75I_1 + 7.9I_2 + 9.01I_3 + 10.59I_4 &\\ + 13.21I_5 + 18.9I_6 + 10.68I_7 &= E_7. \end{aligned} \tag{2}$$

Here, I_i is the specific emittance in the ith layer and E_i is the response of the ith detector.

Solving this set of equations for each time sample, we obtain the evolution of the plasma radiative loss profile.

An important advantage of this method is that the matrix in set (2) is triangular, which is favorable for reducing errors in solving this set numerically. In order to estimate these errors, we performed numerical simulations of model profiles with a certain noise component superimposed. These profiles were taken as initial data for the inverse problem. After solving the problem by the method proposed, the solution obtained should coincide with the initially given function. The deviation from the initial profile is the error introduced by this method. Based on a series of such simulations, the relative error in recovering the radiative loss profile was

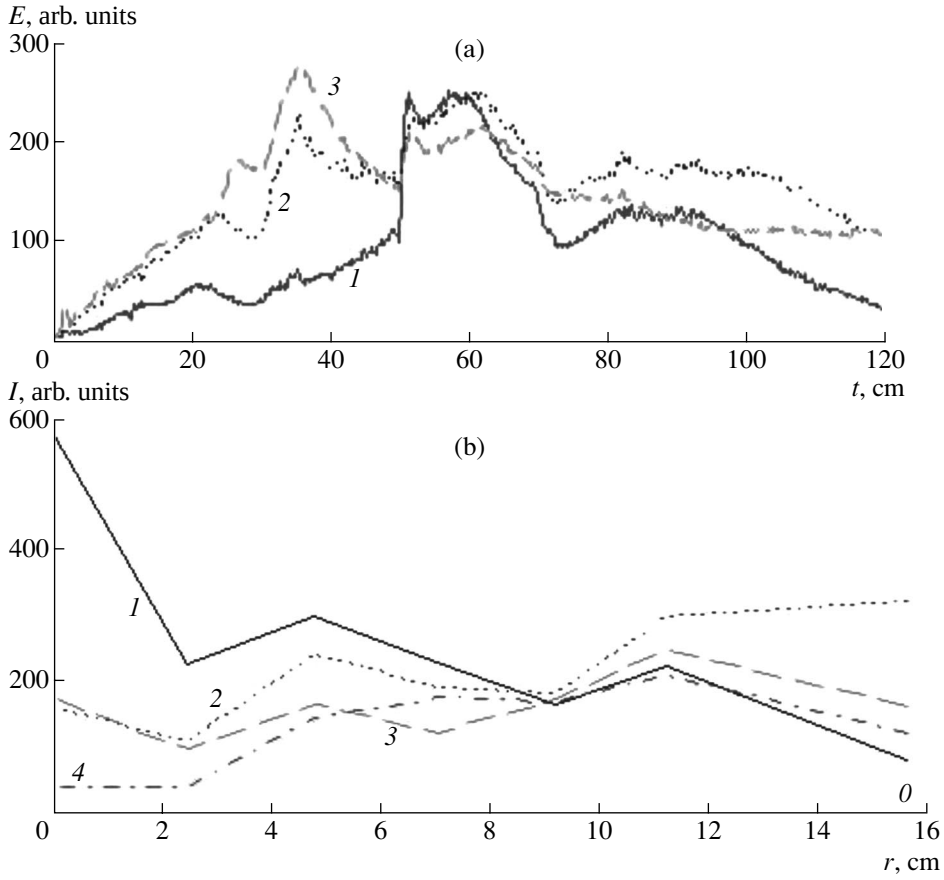

Fig. 8. (a) Raw AUXV detector signals for a discharge with a negatively biased lithium limiter: (*1*) 1st (*2*) 4th, and (*3*) 7th channels; (b) the recovered radiative loss profiles for t = (*1*) 40, (*2*) 60, (*3*) 80 and (*4*) 100 ms.

found to be a factor of 3–5 larger than the initial noise level. Hence, at an initial noise level of 1–5%, the error in recovering the radiative loss profile is 5–25%.

4. RESULTS

To illustrate, we present the results obtained for three different shots:

(i) shot no. 13132 with a high (4×10^{13} cm^{-3}) plasma density (Figs. 3, 4);

(ii) shot no. 13100 with a moderate (1.8×10^{13} cm^{-3}) plasma density and a hot lithium limiter (the limiter temperature before the shot was 237°C, which was higher than the lithium melting temperature by 50°) (Figs. 5, 6), and

(iii) shot no. 13119 with a low (1.2×10^{13} cm^{-3}) plasma density and a cold biased lithium limiter (the lithium limiter was at a negative potential of –400 V with respect to the vacuum vessel) (Figs. 7, 8) [3].

The results obtained (Figs. 4, 6, 8) satisfactorily describe the major features of the plasma radiative loss profile. In high-density plasmas (Fig. 4), an intense peak appears at the plasma center. This peak coincides with the onset of soft X-ray emission from this region (Fig. 3). In contrast, in low-density plasmas, the plasma radiation profile is flattened and is even depressed inside the plasma column (Fig. 6). When the lithium limiter is negatively biased, the radiation intensity in a 5-cm-thick outer layer substantially increases (nearly doubles) in the time interval 50–70 ms (Fig. 8) because of the injection of an additional influx of lithium atoms into the edge plasma due to the ion sputtering effect [3].

Local variations in the emission profile (within 20% of the averaged level) can be ignored, because their amplitude is close to the numerical error.

To measure the absolute value of the radiative loss power, the system was calibrated using an He puff and a Li limiter (shot no. 17281), assuming the total radiative loss power to be close to the ohmic heating power.

The raw data and the recovered radiative loss profiles are presented in Fig. 9. As was expected, intense radiation peaks are observed at the center of the plasma column (which is related to the accumulation of neon) and at the periphery (which is related to lithium emission).

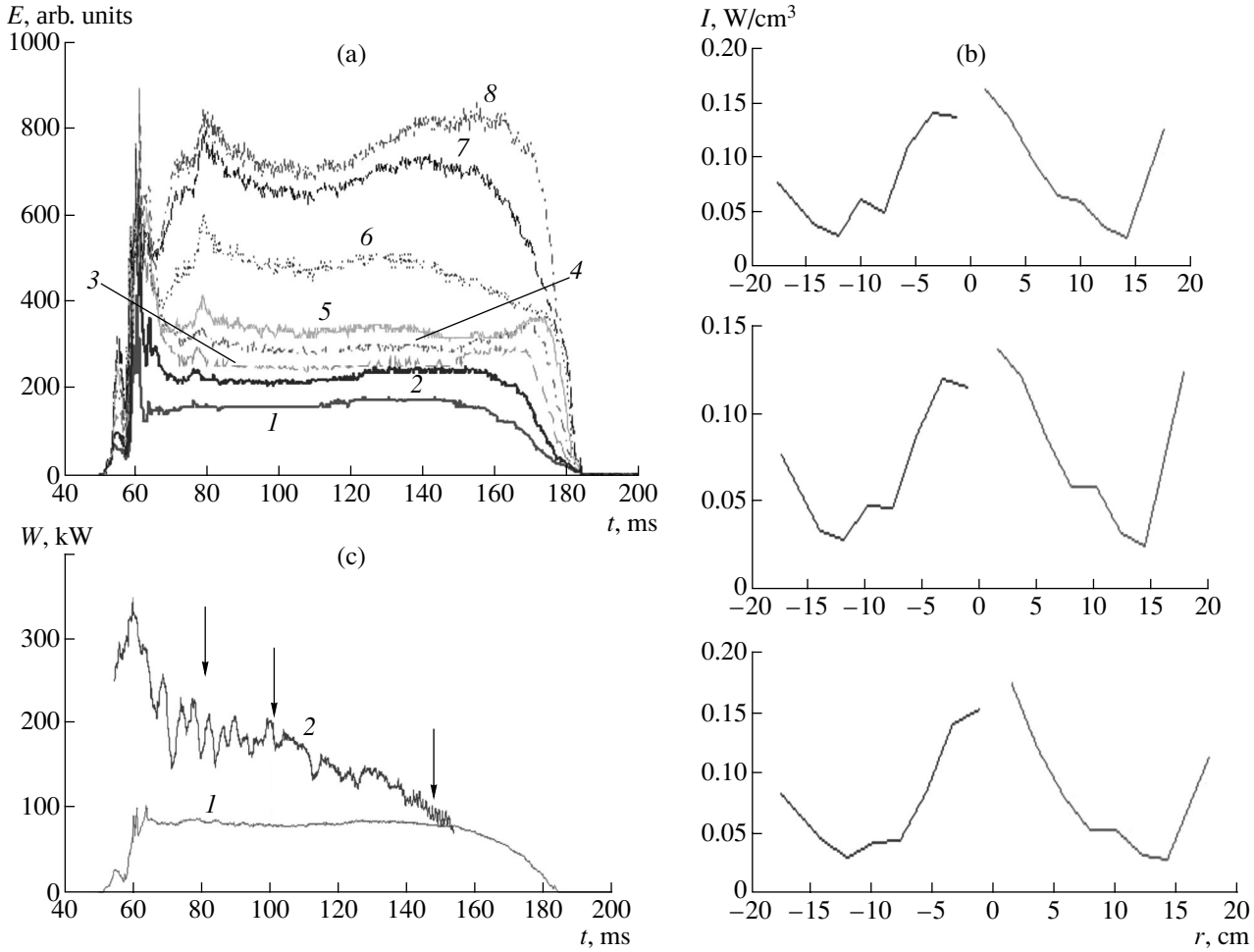

Fig. 9. (a) Raw AXUV detector signals for a calibration discharge with neon puff: (*1*) 15th, (*2*) 13th, (*3*) 11th, (*4*) 9th, (*5*) 7th, (*6*) 5th, (*7*) 3rd, and (*8*) 1st channels; (b) the recovered radiative loss profiles for t = 80, 100, and 150 ms (from top to bottom); and (c) the evolution of the (*1*) total radiative loss power and (*2*) ohmic power (the arrows indicate the instants corresponding to the recovered profiles in Fig. 9b).

5. CONCLUSIONS

A stable algorithm similar to the well-known cylindrically symmetric Abel inversion has been elaborated for recovering the plasma radiative loss profile in tokamaks by analyzing the data from a detector with a tangential field of view.

When applied to the AXUV detector system of the T-11M tokamak, the method allows the recovery of a plasma radiation profile with an accuracy of 25% even with a relatively small number of detector channels (seven to eight). Clearly, it would be expedient to double the number of detector channels in order to increase the accuracy of the method.

REFERENCES

1. A. Alekseyev, G. Perov, A. Kurnosov, *et al.*, Plasma Devices Op. **7**, 139 (1999).
2. V. Lazarev, E. Azizov, E. Alekseyev, *et al.*, in *Proceedings of the 26th EPS Conference on Plasma Physics and Controlled Fusion, Maastricht, 1999*; ECA **23J**, 845 (1999).
3. V. Evtikhin, I. Lyublinski, A. Vertkov, *et al.*, in *Proceedings of the 21st Symposium on Fusion Technology, Madrid, 2000*, Paper A-37.
4. V. Evtikhin, I. Lyublinski, A. Vertkov, *et al.*, in *Proceedings of the 18th IAEA Fusion Energy Conference, Sorrento, 2000*, Paper EXP4/21.

Translated by N.F. Larionova

Plasma Physics Reports, Vol. 30, No. 2, 2004, pp. 143–148. Translated from Fizika Plazmy, Vol. 30, No. 2, 2004, pp. 163–168.

PLASMA DIAGNOSTICS

Diagnostics of Fast Processes in Laser Plasmas after the Irradiation of Low-Density Media in the Mishen Facility

A. É. Bugrov, I. N. Burdonskiĭ, V. V. Gavrilov, A. Yu. Gol'tsov, O. L. Dedova, E. V. Zhuzhukalo, N. G. Koval'skiĭ, V. N. Kondrashov, M. I. Pergament, V. M. Petryakov, I. K. Fasakhov, and G. M. Yankovskiĭ

Troitsk Institute for Innovation and Fusion Research, Troitsk, Moscow oblast, 142190 Russia

Received July 24, 2003

Abstract—New experimental data on the laser irradiation of low-density porous materials in the Mishen facility are presented and discussed. A wide set of optical and X-ray diagnostics was used to analyze the physical processes in porous media with different microstructures and specific densities of 1–30 mg/cm^3 exposed to laser pulses with $\lambda = 1.054$ μm, $\tau = 3$ ns, and $I = 10^{13}$–10^{14} W/cm^2. The features of laser absorption and scattering and the processes of energy transfer in porous media were investigated for different average densities, thicknesses, and microstructures of the targets and different incidence angles of the laser beam. It was found that the material microstructure (chaotic or quasi-ordered) significantly affected the formation and dynamics of a plasma produced inside the irradiated samples that model the components of the advanced targets used in inertial confinement fusion research. © *2004 MAIK "Nauka/Interperiodica".*

1. INTRODUCTION

In recent years, the interaction of high-power laser radiation with low-density (1–100 mg/cm^3) volume-structured media have attracted great interest [1–4]. The study of laser absorption and mechanisms for energy transfer in low-density media opens up new opportunities for resolving a number of fundamental problems of high-energy-density physics, including inertial confinement fusion (ICF), radiative hydrodynamics, the study of the equation of state under extreme conditions, and the modeling of astrophysical phenomena under laboratory conditions. It should be noted that the plasma produced in the interaction of high-power laser radiation with matter possesses a number of specific features: short lifetime (a few nanoseconds), small dimensions (a few hundred micrometers), high density and inhomogeneity, and highly nonsteady behavior. Under such conditions, scientific information can only be gained from diagnostic techniques that provide extremely high temporal and spatial resolution. The Mishen facility created at the Troitsk Institute for Innovation and Fusion Research is equipped with a complex of optical and X-ray diagnostics [5–8] that furnish detailed information about the interaction of high-power laser radiation with porous media having various internal structures.

2. EXPERIMENTAL AND DIAGNOSTIC TECHNIQUES

Experiments on the interaction of high-power laser radiation with low-density media were carried out under the following conditions: The laser wavelength was 1.054 μm, the laser pulse energy was as high as 100 J, and the laser pulse duration was ~3 ns (the rise time being 0.3 ns). The energy contrast was no worse than 10^6. Laser radiation was focused onto a plane target by a lens with an aperture ratio of 1 : 10. The average laser intensity on the irradiated target surface attained $\sim 5 \times 10^{13}$ W/cm^2 at a focal spot diameter of ~250 μm. Plane agar-agar $(C_{12}H_{18}O_9)_n$ or foam polystyrene $(CH)_n$ targets with average densities from 1 to 30 mg/cm^3 and thicknesses of 100–1000 μm were placed in a vacuum chamber. Agar-agar is a chaotic structure of solid fibers and films, whereas polystyrene has a quasi-ordered film structure. The photos illustrating agar-agar and foam polystyrene structures are shown in Fig. 1.

The X-ray diagnostics employed in the Mishen facility allow the following measurements: time-integrated calorimetric measurements in the wavelength range of 0.5–1.5 nm; pinhole imaging of the plasma using various filters; recording of X-ray plasma emission by vacuum diodes with a time resolution of ~0.5 ns; measurements of plasma X-ray spectra in the wavelength range of 0.5–2 nm; and measurements of the X-ray plasma emission with a spatial, temporal, and spectral resolution with the help of an X-ray streak camera. The optical diagnostics include multiframe shadowgraphy of the produced plasma (with an exposure of ~0.3 ns, a probing radiation wavelength of $\lambda = 0.53$ μm, and a spatial resolution of ~30 μm); monitoring of the time evolution of the emission intensity from the rear surface of the target in the wavelength range of 400–700 nm with a spatial resolution of ~30 μm and time resolution of 50 ps with the use of an Agat-SF

1063-780X/04/3002-0143$26.00 © 2004 MAIK "Nauka/Interperiodica"

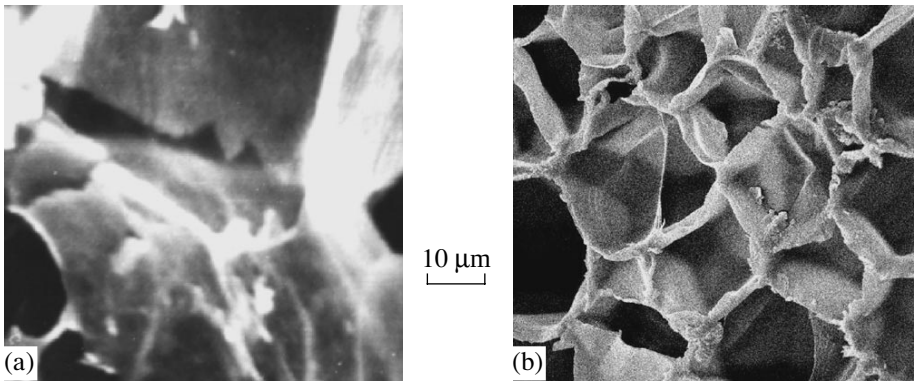

Fig. 1. Electron micrographs of the structure of (a) agar-agar and (b) foam polystyrene with the same average density of 10 mg/cm^3.

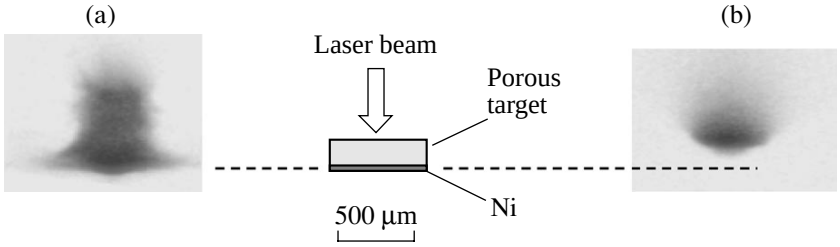

Fig. 2. Typical X-ray pinhole images of the irradiated (a) foam polystyrene and (b) agar-agar targets with an average density of 10 mg/cm^3 and a thickness of 200 μm. The rear surfaces of the targets are covered with a 0.6-μm Ni foil.

streak camera; measurements of the reflected, transmitted, and scattered laser radiation; and time-integrated and time-resolved spectral measurements of the radiation emitted from the plasma into the aperture of the focusing lens at frequencies near $2\omega_0$ and $3\omega_0/2$, where ω_0 is the laser frequency.

3. RESULTS AND DISCUSSION

In [5–8], it was shown that the absorption of laser radiation in a porous low-density medium is volumetric in character. Absorption and subsequent energy transfer result in the formation of a rather deep high-temperature plasma layer inside a porous target. For example, in the case of an agar-agar target with an average density of 1 mg/cm^3, the depth of this layer (along the laser beam) amounts to 400–500 μm. For a target with a density of 10 mg/cm^3, this depth is reduced to 100–150 μm. The duration of the X-ray pulse recorded using vacuum diodes is 3–4 ns, which is nearly equal to the laser pulse duration. For agar-agar targets, the plasma electron temperature determined by the filter method under the assumption of a Maxwellian electron velocity distribution amounts to 0.8–1 keV and somewhat decreases deep into the target. It was shown in [9] that, for the target irradiation parameters close to those achieved in our experiments, the temperature of suprathermal electrons is ~5 keV, whereas the relative concentration of the hot electron component is ~10^{-5}. Under these conditions, the error in measuring the electron temperature of the bulk plasma by the filter method is less than 10% [10]. Such an electron temperature value was also obtained in [11, 12] using X-ray spectroscopy; the ion temperature was estimated to be a factor of 1.5–2 higher than the electron one.

Let us compare the experimental data on the laser irradiation of agar-agar and foam polystyrene targets of equal densities (≈10 mg/cm^3). Figure 2 shows typical X-ray plasma images recorded behind a 1.5-μm Al foil. It can be seen that, for a foam media with a quasi-ordered structure, the depth of the hot region (along the laser beam) is two to three times larger than for an agar-agar target with a chaotic fiber–film structure.

There is also a drastic difference in the rate of energy transfer into irradiated low-density agar-agar and foam polystyrene targets. The data on energy transfer were obtained by monitoring the glow of the rear target surface in the optical range and using multiframe shadowgraphy ($\lambda = 0.53$ μm) of the accelerated part of the target. The corresponding experimental data are shown in Figs. 3 and 4.

It can be seen that the rear surface of a foam polystyrene target starts glowing at the third nanosecond

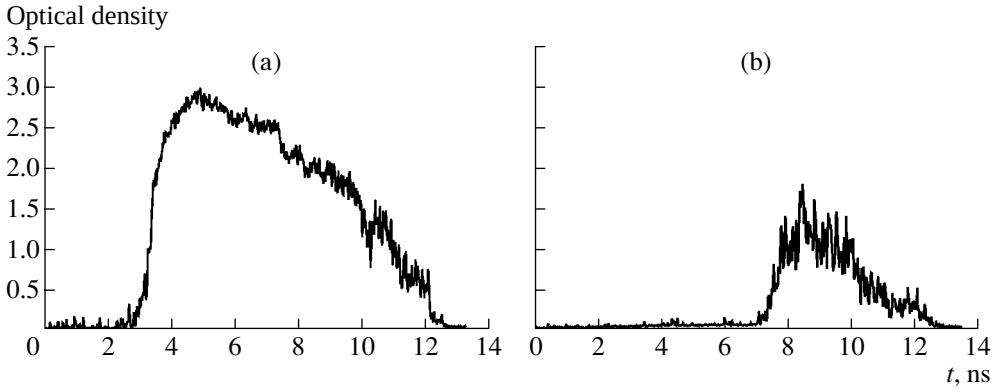

Fig. 3. Densitograms of the signals from a streak camera recording visible emission from the rear surfaces of the irradiated (a) foam polystyrene and (b) agar-agar targets with an average density of ≈10 mg/cm^3 and a thickness of ≈200 μm. The rear surfaces of the targets were covered with a 0.6-μm Ni foil.

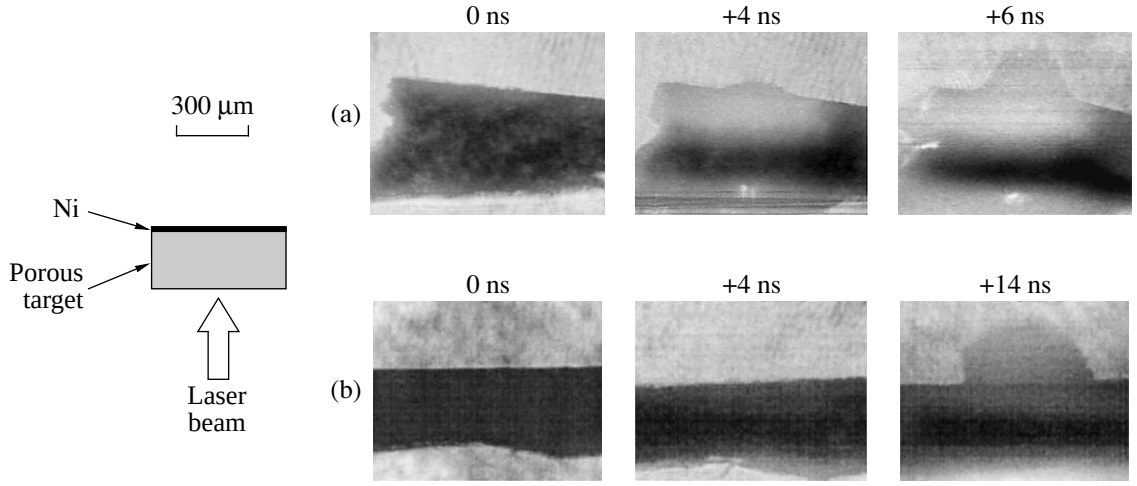

Fig. 4. Visible-light shadowgraphs illustrating the acceleration of the rear surfaces of the irradiated (a) foam polystyrene and (b) agar-agar targets with an average density of ≈10 mg/cm^3 and a thickness of ≈200 μm. The rear surfaces of the targets were covered with a 0.6-μm Ni foil. Time is counted from the beginning of the laser pulse.

after the beginning of the laser pulse (Fig. 3). It can also be seen that, at the fourth nanosecond, the rear surface of the target has already begun to move (Fig. 4). In the case of an agar-agar target, the rear surface starts glowing 7 ns after the beginning of the laser pulse. The images taken at the fourth and fourteenth nanoseconds illustrate the acceleration of the rear surface of the agar-agar target. An analysis of these images, together with images obtained in other experiments, shows that the rear surface starts moving 8–9 ns after the beginning of the laser pulse. Measurements performed with samples of different thicknesses show that the rates of energy transfer in foam and agar-agar targets with the same average density of 10 mg/cm^3 are $(3–4) \times 10^7$ cm/s and $(7–8) \times 10^6$ cm/s, respectively.

The results of space- and time-resolved measurement of plasma emission at the second harmonic of the laser frequency (λ = 0.53 μm) in experiments with polystyrene and agar-agar targets are also of interest. Typical time evolutions of the second-harmonic emission intensity for laser-irradiated foam and agar-agar targets are shown in Figs. 5a and 5b, respectively. Since the second harmonic is generated only in regions where the plasma density is close to critical (10^{21} cm^{-3} for λ = 1.054 μm), the time history of the second-harmonic intensity obtained in experiments on the laser irradiation of low-density agar-agar and foam targets provides information on the formation and homogenization of the high-temperature plasma produced inside the targets [13]. Figure 5a allows us to suppose that, in targets with a quasi-ordered film structure, laser radiation

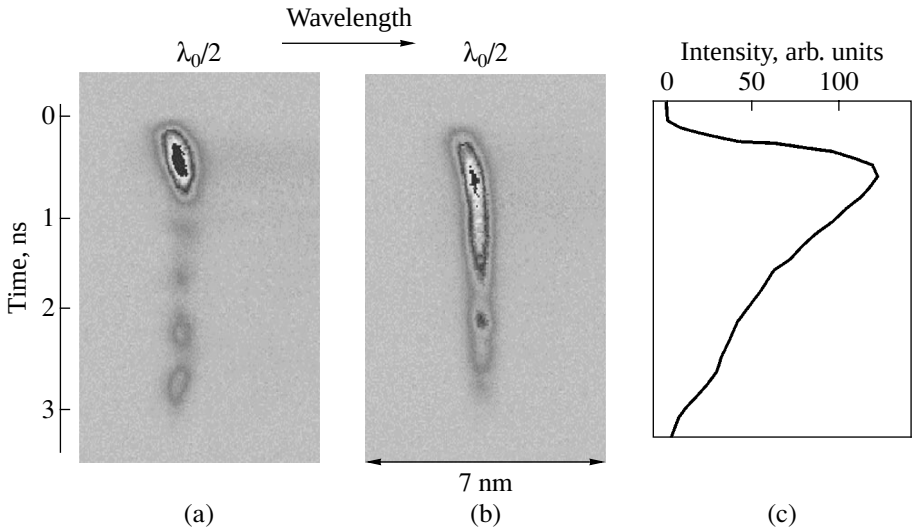

Fig. 5. Time evolution of the plasma emission spectra near the second-harmonic frequency recorded in experiments with (a) foam polystyrene and (b) agar-agar targets with an average density of 10 mg/cm^3 and a thickness of 300 μm and (c) the time history of the laser pulse intensity.

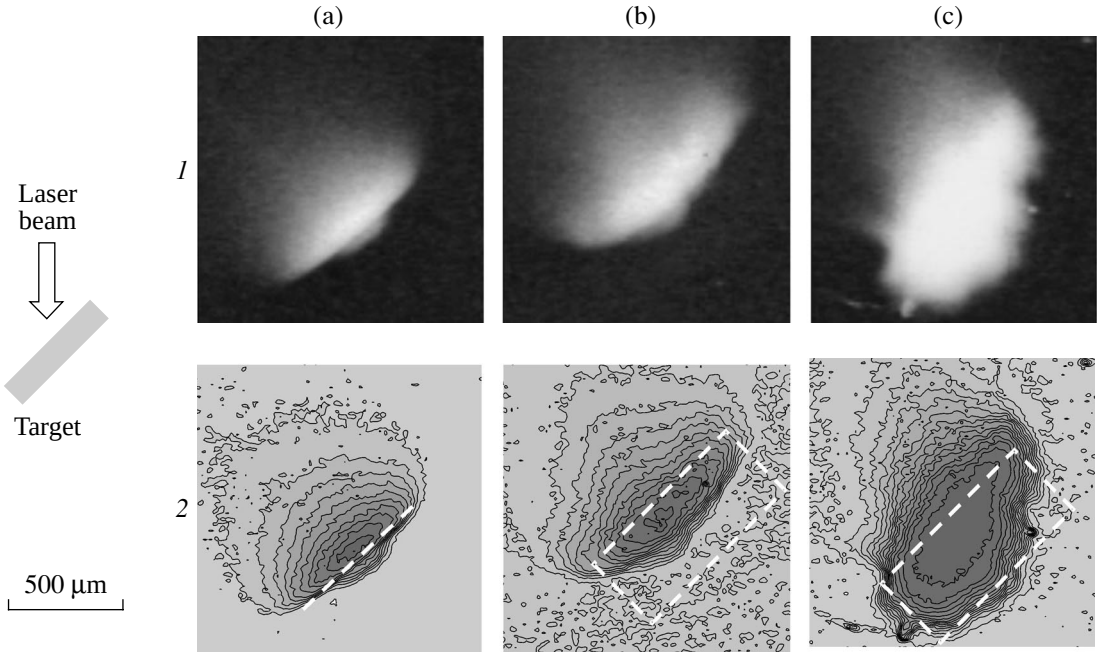

Fig. 6. (*1*) X-ray pinhole images recorded in experiments with a laser beam incident obliquely (at an angle of 45°) onto (a) a 7-μm-thick Mylar target and (b, c) 400-μm-thick agar-agar targets with densities of (b) 5 and (c) 2 mg/cm^3; (*2*) the results of processing these images (the initial target positions are sketched by the dashed lines).

interacts sequentially with individual solid elements of the medium. The equidistant breaks observed in the time evolution of the second-harmonic intensity indicate that the density of the expanding plasma produced in the course of irradiation of the previous solid element becomes lower than the critical density before the laser pulse begins to interact with the next element. No such breaks in the time evolution of the second-harmonic intensity were observed in experiments with agar-agar targets (see Fig. 5b) of the same average density (10 mg/cm^3). Therefore, in the case of a chaotic medium structure, there are always regions inside the

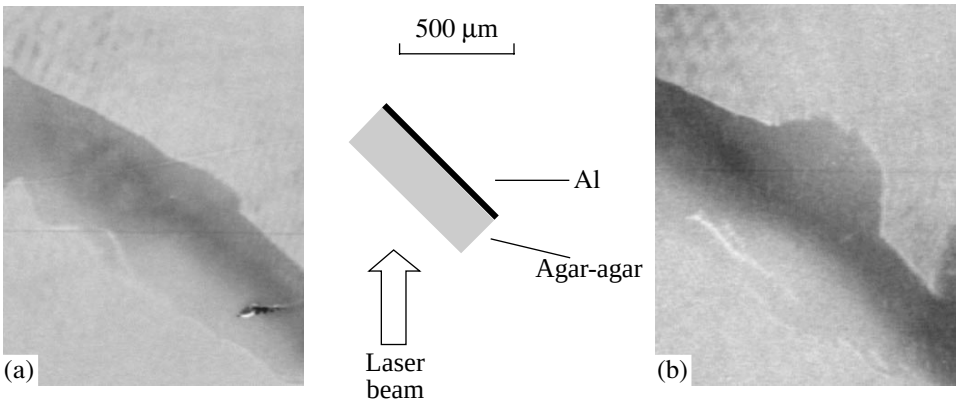

Fig. 7. Shadowgraphs recorded in experiments with a laser beam incident obliquely (at an angle of 45°) onto a 400-μm-thick agar-agar target with a density of 2 mg/cm^3 at the instants t = (a) 4 and (b) 6 ns after the beginning of the laser pulse.

samples where the plasma density is critical during the entire laser pulse.

We carried out a special series of experiments on the interaction of an oblique laser beam with a plane agar-agar target. Specific features of the formation of a high-temperature plasma and energy transfer under such conditions should be taken into account when considering the feasibility of providing a uniform distribution of the ablation pressure on the surface of a thermonuclear capsule in experiments with indirect-irradiation [3] and hohlraum [4] targets with the use of low-density materials. Figure 6 shows pinhole images recorded in the interaction of laser pulses with agar-agar targets of different densities at an incidence angle of 45° (for comparison, a pinhole image obtained in an experiment on the irradiation a Mylar film is also shown).

It can be seen that, for agar-agar targets with relatively high average densities (≥5 mg/cm^3), the formation and propagation of a high-temperature plasma region inside the target occurs in the direction perpendicular to the target surface (Fig. 6b). We note that a similar distribution of the high-temperature plasma takes place both for a laser pulse incident normally onto an identical target and in the case of an obliquely irradiated thin solid-state Mylar target (Fig. 6a). For targets with relatively low average densities (≈2 mg/cm^3) and an incidence angle of 45°, the high-temperature plasma region inside the agar-agar target is stretched along the propagation direction of the laser beam (Fig. 6c). Nevertheless, the efficiency of energy transfer onto the rear surface of a target is still rather high, as is the case with higher density agar-agar targets (≥5 mg/cm^3). The shadow photographs shown in Fig. 7 clearly demonstrate energy transfer onto the rear surface of an agar-agar target with an average density of 2 mg/cm^3 (for diagnostic purposes, the rear surface was covered with a thin Al layer). Shadow photography also shows that the substance at the rear side of the target is accelerated normally to the target surface.

4. CONCLUSIONS

The diagnostic complex of the Mishen facility allows X-ray and optical measurements with high space, time, and spectral resolutions. The interaction of high-power laser pulses with low-density (1–30 mg/cm^3) media of different internal structure (fibrous agar-agar and foam polystyrene) has been investigated systematically.

By employing in each experiment a combination of complementary diagnostic methods, we have obtained reliable information on the properties and behavior of the dense high-temperature plasma produced in the interaction of high-power laser radiation (10^{13}–10^{14} W/cm^2) with targets made of low-density substances of different internal structure.

The analysis of the experimental data obtained shows that the most interesting and important results are as follows:

(i) It is found that the microstructure of the low-density materials that model the components of advanced ICF targets significantly affects the formation and dynamics of the plasma produced inside the irradiated samples. For foam polystyrene targets with a quasi-ordered structure and an average density of 10 mg/cm^3, the thickness of the hot plasma region and the rate at which the energy is transferred deep into the target are a factor of 4–5 larger than those for agar-agar targets with a chaotic fibrous structure and the same average density.

(ii) It is shown that, when a laser beam is obliquely incident (at an angle of 45°) onto a target made of a relatively dense (≥5 mg/cm^3) porous material with randomly directed thin fibers (agar-agar samples), the formation and propagation of the high-temperature plasma region inside the sample occurs in a direction perpendicular to the target surface. For targets with a lower average density (≈2 mg/cm^3), the high-temperature plasma region inside the sample is stretched along the propagation direction of the laser beam. In both cases,

the substance at the rear side of a plane target is accelerated normally to the target surface (at an angle of 45° with respect to the laser propagation direction). The efficiency of energy transfer toward the rear surface of a low-density sample is as high as that in the case of a dense sample.

The results obtained can be used in computer codes intended for searching the optimum structure and parameters of low-density materials used in various kinds of advanced ICF targets.

ACKNOWLEDGMENTS

We are grateful to V.G. Nikolaevskiĭ, V.G. Ponomarev, and B.F. Vasil'ev for providing the operation of the Mishen facility. This study was supported by the Russian Foundation for Basic Research (project nos. 01-02-17361 and 01-02-17336) and INTAS (grant no. 2001-0572).

REFERENCES

1. J. Lindl, Phys. Plasmas **2**, 3933 (1995).
2. O. L. Landen, D. R. Farley, S. G. Glendinning, *et al.*, Rev. Sci. Instrum. **72**, 627 (2000).
3. O. Willi, L. Barringer, C. Vickers, *et al.*, Astrophys. J., Suppl. Ser. **127**, 527 (2000).
4. G. A. Vergunova, A. I. Gromov, S. Yu. Gus'kov, *et al.*, Preprint No. 58 (Lebedev Physical Institute, Russian Academy of Sciences, Moscow, 1999).
5. V. A. Bolotin, I. N. Burdonsky, V. V. Gavrilov, *et al.*, Rev. Sci. Instrum. **61**, 3259 (1990).
6. A. E. Bugrov, I. N. Burdonsky, V. V. Gavrilov, *et al.*, in *Proceedings of the 1st International Conference on Inertial Fusion Sciences and Applications, Bordeau, 1999* (Elsevier, Paris, 2000), p. 154.
7. A. É. Bugrov, I. N. Burdonskiĭ, V. V. Gavrilov, *et al.*, Zh. Éksp. Teor. Fiz. **111**, 903 (1997) [JETP **84**, 497 (1997)].
8. V. A. Bolotin, I. N. Burdonsky, V. V. Gavrilov, *et al.*, Proc. SPIE **4424**, 367 (2001).
9. I. N. Burdonskiĭ, V. V. Gavrilov, A. Yu. Gol'tsov, *et al.*, Fiz. Plazmy **13**, 819 (1987) [Sov. J. Plasma Phys. **13**, 473 (1987)].
10. V. V. Gavrilov, N. V. Torokhova, and I. K. Fasakhov, in *Plasma Diagnostics* (Énergoatomizdat, Moscow, 1986), No. 5, p. 284.
11. V. V. Gavrilov, A. Yu. Gol'tsov, N. G. Koval'skiĭ, *et al.*, Kvantovaya Élektron. (Moscow) **31**, 1071 (2001).
12. A. Ya. Faenov, I. K. Fasakhov, V. V. Gavrilov, *et al.*, in *Proceedings of the 2nd International Conference on Inertial Fusion Sciences and Applications, Kyoto, 2001* (Elsevier, Paris, 2002), p. 323.
13. A. É. Bugrov, I. N. Burdonskiĭ, V. V. Gavrilov, *et al.*, Zh. Éksp. Teor. Fiz. **115**, 805 (1999) [JETP **88**, 441 (1999)].

Translated by N.N. Ustinovskiĭ

Plasma Physics Reports, Vol. 30, No. 2, 2004, pp. 149–153. Translated from Fizika Plazmy, Vol. 30, No. 2, 2004, pp. 169–174.

PLASMA DIAGNOSTICS

Interaction of Laser Plasmas with Noble Gases

V. E. Levashov, K. N. Mednikov, A. S. Pirozhkov, and E. N. Ragozin

Lebedev Physical Institute, Russian Academy of Sciences, Leninskiĭ pr. 53, Moscow, 119991 Russia

Received July 24, 2003

Abstract—The interaction of a noble gas jet (Xe, Kr, He) with a laser plasma at a distance of ~1 cm from a solid target (Mg, $(CH_2)_n$, LiF, or CF_4) was studied for the first time. The line spectra that were excited in the course of charge exchange of multicharged ions with noble gas atoms in the interaction region were recorded. A clean (debris-free) soft X-ray source excited by laser pulses focused into a xenon jet was designed and investigated. © *2004 MAIK "Nauka/Interperiodica".*

1. INTRODUCTION

By charge exchange, we mean processes of the type $X^{q+} + A \longrightarrow X_{nl}^{*(q-1)+} + A^+$, where X^{q+} is a projectile multicharged ion in the ground state, A is a neutral atom, $X_{nl}^{*(q-1)+}$ is the resultant ion in the nl excited state, and A^+ is the resultant single-charged ion. Interest in charge exchange processes stems largely from the fact that the resultant ions are in the excited states and the charge exchange cross section can be relatively high (10^{-15}–10^{-14} cm^2, which is higher than that for other processes with the participation of multicharged ions). In addition, charge exchange is of quasi-resonance nature, which, in principle, enables one to achieve the selective population of the multicharged ion states and population inversion in soft X-ray (SXR) transitions [1–3].

Although charge exchange cross sections have often been measured in beam–plasma experiments, the distribution of the resultant ions over the energy states still remains unknown. Spectroscopic measurements allow one to evaluate such a distribution by recording transitions of multicharged ions in the SXR range. In the few available spectroscopic experiments, charge exchange processes were believed to be responsible for the onset of or increase in the intensity of certain spectral lines; however, these spectral features can be related to alternative plasma processes (recombination or extra heating). In a tokamak plasma, the H_α transition in O VIII ions (λ = 10.2 nm) was observed in experiments with the injection of neutral atomic hydrogen beams [4]. The population of the n = 3 level was related to the charge-exchange reaction of oxygen nuclei with hydrogen atoms

$$O^{8+} + H \longrightarrow O^{*7+} + H^+.$$

It was noted, however, that there was no corresponding increase in the intensity of the Ly_α and Ly_β lines ($2 \longrightarrow 1$ and $3 \longrightarrow 1$ transitions). That charge exchange plays an important role in more complicated systems, such as a laser plasma expanding into a buffer gas, was demonstrated by comparing the experimental spectra with the results of numerical simulations [5]. Observations of the visible transitions of multicharged ions excited in the course of charge exchange with neutral atomic beams serve as a diagnostic tool in tokamak plasmas (see, e.g., [6]).

In the present study, we experimentally investigated the charge exchange of multicharged ions with noble gas atoms in the interaction of a noble gas jet with a laser plasma created by irradiating a solid target. For this purpose, space-resolved SXR radiative decay spectra of the excited states of $X_{nl}^{*(q-1)+}$ ions were recorded.

We also carried out experiments in which laser radiation was focused directly into a xenon jet, which served as a plasma source of quasi-continuous SXR emission. Such a clean (debris-free) SXR source is of

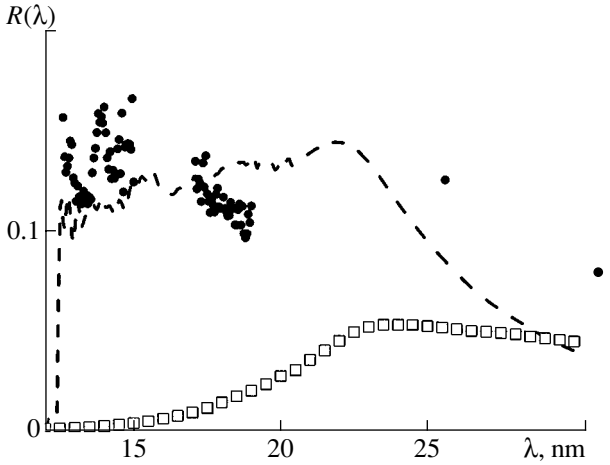

Fig. 1. Measured (circles) and calculated (dashed line) reflection coefficients of an aperiodic MM at an incidence angle of 5°. The calculated reflection coefficient of solid molybdenum is shown by the squares. The measurements were performed at the Institute for the Physics of Microstructures of the Russian Academy of Sciences (Nizhni Novgorod).

1063-780X/04/3002-0149$26.00 © 2004 MAIK "Nauka/Interperiodica"

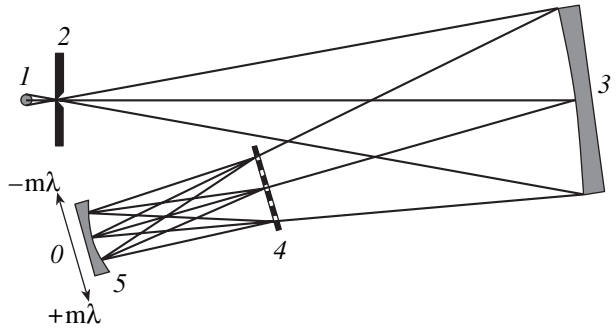

Fig. 2. Schematic of a large-aperture stigmatic spectrograph consisting of a focusing aperiodic MM (*3*) (with a radius of curvature of $r = 1$ m and an aperture of $D = 5$ cm) and a transmission grating (*4*): (*1*) laser plasma, (*2*) entrance slit, and (*5*) cassette with an UF-4 X-ray film.

interest for both laboratory studies (reflectometry and absorption spectroscopy) and X-ray projection microlithography.

2. EXPERIMENTAL SETUP

All the experiments were carried out in the IKAR vacuum chamber (0.9 m in diameter and 3.8 m in

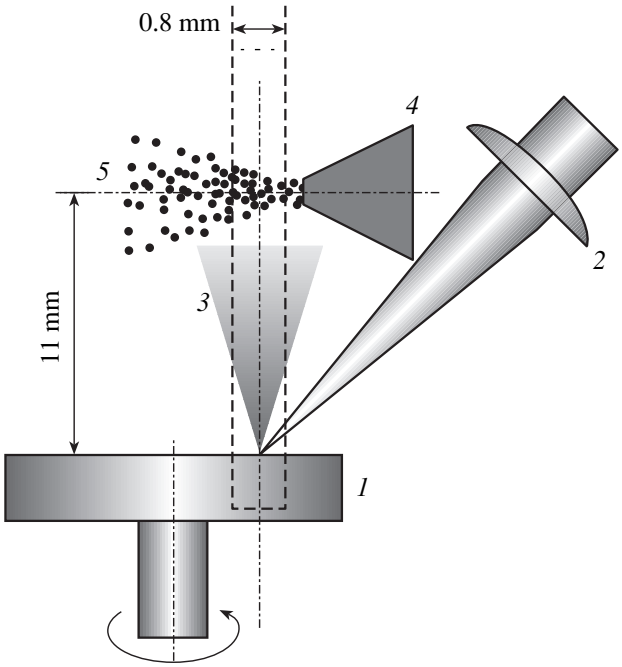

Fig. 3. Disposition of the laser plasma (*3*) and gas cloud (*5*): (*1*) rotating target, (*2*) focusing lens, and (*4*) gas valve nozzle. The dashed lines outline the viewing field of the spectrograph.

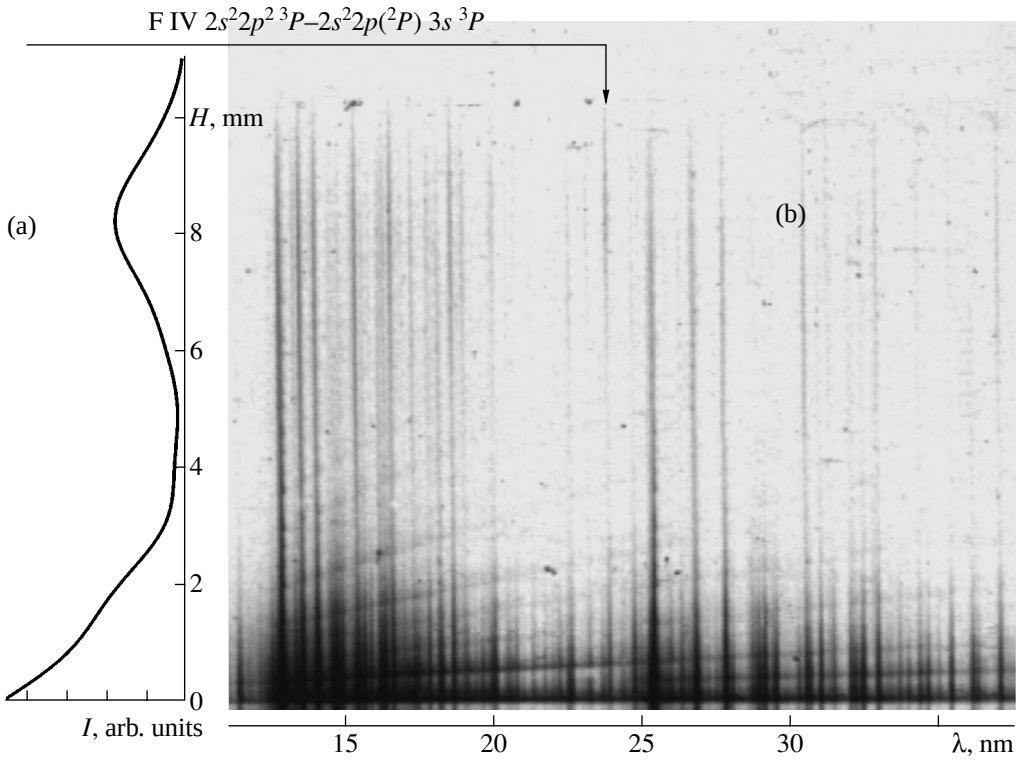

Fig. 4. (a) The total intensity of the six unresolved lines of the F IV $2s^2 2p^2\ ^3P$–$2s^2 2p(^2P)3s\ ^3P$ transition ($\lambda \approx 23.9$–24.4 nm) vs. distance H from a CF_4 target and (b) the spectrum (integrated over 200 laser pulsed) of a CF_4 plasma interacting with a xenon jet (the lines under study are shown by the arrow). The inclined bands in the spectrum are related to the presence in the transmission grating of a regular supporting structure perpendicular to the grating grooves.

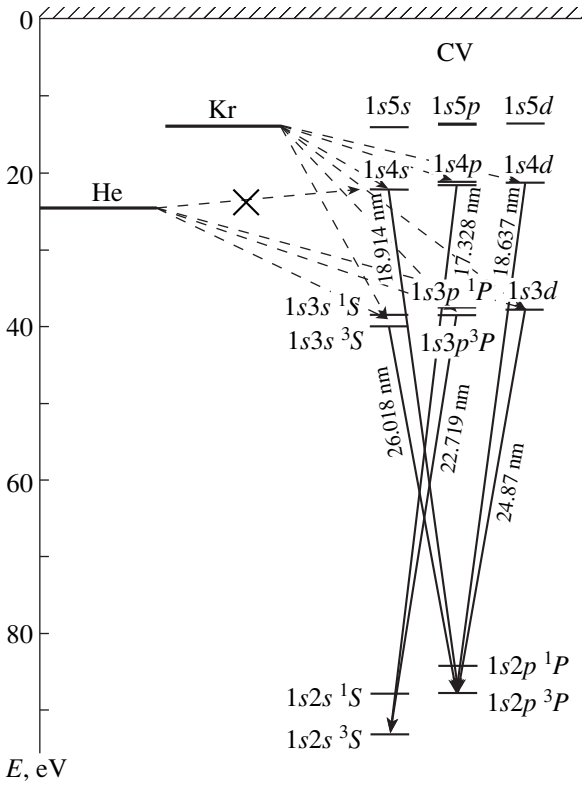

Fig. 5. Level diagram of a CV ion with the ionization energies of Kr and He atoms indicated. The dashed lines show the charge-exchange channels, while the arrows show the spectral lines observed in the experiment.

length). At the end of the chamber, a repetitively pulsed Nd:$YAlO_3$ laser (0.5 J, 6 ns, 1.08 μm, 0.5 Hz) was installed. The gas target was produced with the help of a pulsed high-pressure (up to 10 atm) valve, which was open for ~1.5 ms synchronously with the laser pulses. The diameter of the cylindrical nozzle was 0.4 mm. The gas was supplied from gas tanks placed outside the vacuum chamber.

The employed spectroscopic diagnostic complex enabled us to construct spectral images and record stigmatic spectra in the SXR range. These measurements made it possible to determine the spatial structure of the interaction between the gas jet and laser radiation and between multicharged ions and neutral gas atoms. The diagnostic complex incorporates the most advanced elements of SXR optics: periodic and aperiodic multilayer mirrors (MMs), high-aperture transmission gratings (1000 and 5000 line/mm), high-speed absolutely calibrated AXUV-5 photodiodes, etc. In particular, we designed a high-aperture broadband stigmatic diffraction spectrograph based on an aperiodic multilayer normal-incidence Mo/Si mirror with a nearly constant reflectance in the spectral range of 12.5–25 nm (Figs. 1, 2) [7, 8]. The spectrograph possesses the following features: stigmatism, a field of view of ~2 cm, spectral resolution of no lower than ~300, a wide operating spectral range, and an extremely high aperture ratio (in the plasma–gas interaction region, we were able to record lines with intensities two orders of magnitude lower than those near the laser target). This was achieved by using broadband normal-incidence multilayer optics. To create the spectrograph, we calculated an aperiodic multilayer Mo/Si structure (40 layer pairs) optimized for the maximally uniform reflectance in the wavelength range of 12.5–25 nm at the normal incidence of radiation. Based on these calculations, the first aperiodic MMs were produced at the Kharkov Polytechnic Institute. These MMs were shown to have an almost optimum structure and even reflectance (ranging within 11–15%) in the spectral range of interest. The short-wavelength boundary of the MM operation range is determined by the *L*-edge of Si absorption (12.5 nm), whereas there is no sharp long-wavelength boundary. Thus, we observed the $1s^22s^2S_{1/2}$–$1s^22p^2P_{3/2,1/2}$ doublet of a Mg X ion with λ = 60.979 and 62.495 nm. The spectrograph is described in more detail in [9–11].

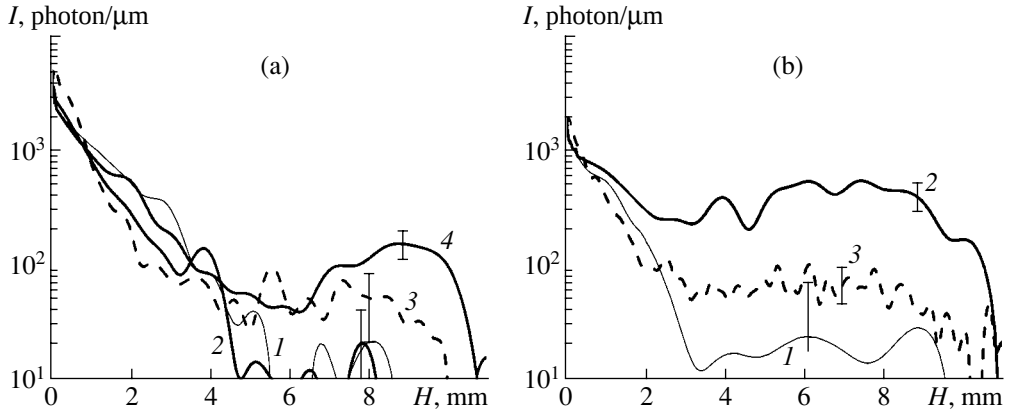

Fig. 6. Exposure from the (a) $1s2s\ ^3S$–$1s4p\ ^3P$ (λ = 17.328 nm) and (b) $1s2p\ ^3P$–$1s3s\ ^3S$ (λ = 26.018 nm) C V ion lines vs. distance *H* from a carbon target: (*1*) without a gas and in the presence of (*2*) He, (*3*) Kr, and (*4*) Xe.

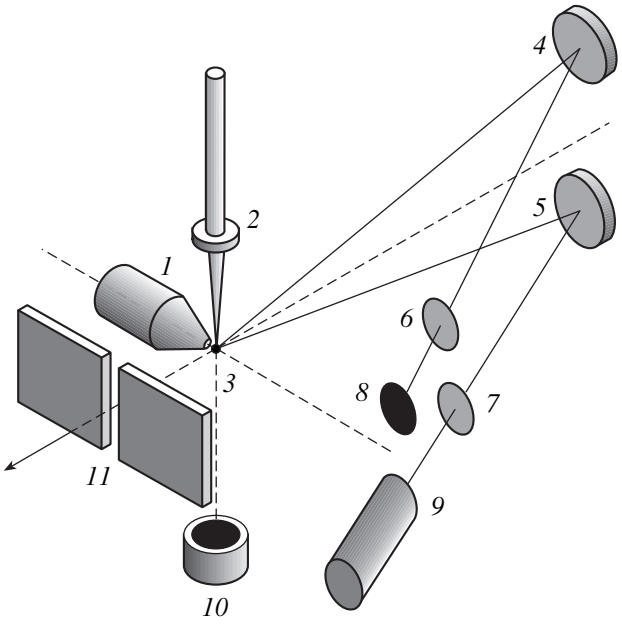

Fig. 7. Arrangement of the diagnostic tools in the experiments with a pulsed gas target: (*1*) pulsed high-pressure gas valve, (*2*) focusing lens, (*3*) Xe plasma in the focal region, (*4*, *5*) identical periodic MMs (λ_0 = 18 nm, $\Delta\lambda_{1/2}$ = 1 nm), (*6*, *7*) Al filters, (*8*) cassette with an UF-4 X-ray film, (*9*) AXUV-5 photodiode, (*10*) VCHD-2 calorimeter, and (*11*) entrance slit of the diffraction spectrograph.

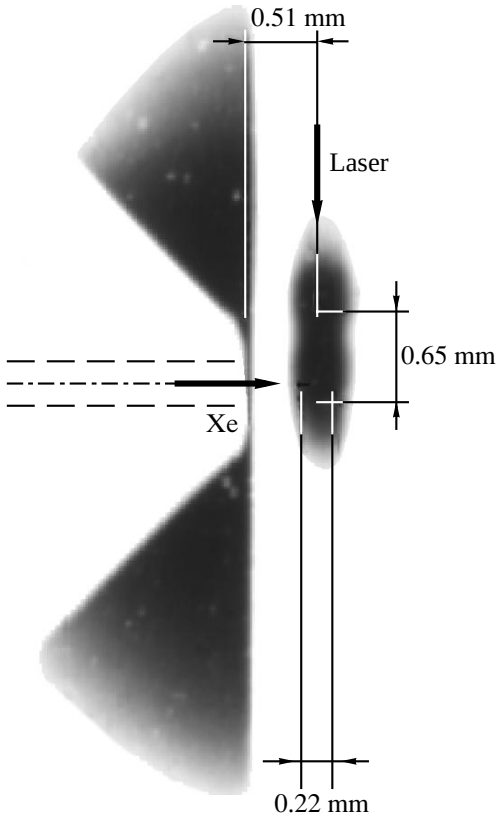

Fig. 8. X-ray image of a xenon plasma in the wavelength range 17.5–18.5 nm and a visible-light shadowgraph of the nozzle (both are obtained using MM 4 shown in Fig. 7).

3. INTERACTION OF A GAS JET WITH PLASMA

The laser plasma produced due to the irradiation of a solid target with nanosecond Nd laser pulses was directed toward the gas (Kr, Xe, or He) jet (Fig. 3). The target was placed at a distance of 7–11 mm from the nozzle axis. The target materials were metallic Mg, LiF crystal, CF_4, or $(CH_2)_n$. The field of view of the spectrograph included both the target surface and the plasma–gas interaction region. The spectrum of plasma emission near the target surface contained the lines of multicharged ions of the corresponding elements: C IV–VI, Li II–III, etc. At a distance of a few millimeters from the target, the line intensities either decreased radically compared to those at the target surface or vanished almost completely. However, in all our experiments, the emission of certain spectral lines was again observed in the plasma–gas interaction region (Fig. 4). We relate this phenomenon to the intense population of the excited states of plasma ions in the course of charge exchange with neutral gas atoms.

In charge-exchange reactions proceeding via the Landau–Zener mechanism (in contrast to recombination processes), the levels of multicharged ions are mainly populated whose ionization energy exceeds the ionization energy of the donor atoms. The ionization energies of Kr and Xe are 14.0 and 12.1 eV, respectively, whereas the ionization energy of He is 24.6 eV. The spectra observed in the interaction of plasma with He differ from those observed in the interaction with Kr or Xe. Thus, the levels of a C V ion with the principal number $n = 4$ (these levels lie higher than the ground state of He but lower than ground state of Kr) are not populated in the interaction of a carbon plasma with helium and are populated in the interaction with krypton (see Figs. 5 and 6). This is direct experimental evidence that the excited states of multicharged ions in the plasma–gas interaction region are populated via charge-exchange processes.

From the intensity ratio of the H_α ($3 \longrightarrow 2$, λ = 18.2 nm) and H_β ($4 \longrightarrow 2$, λ = 13.5 nm) lines of C VI ions, one can determine the ratio between the cross sections of charge-exchange processes resulting in the excitation of the levels with $n = 3$ and 4. To do this, it is necessary to take into account the fact that the electron density is relatively low, so that the levels with $n = 4$ and 3 reside in a pure radiative zone ($A_n \gg N_e c(n, n-1)$), and that the electron temperature is also low and, hence, collisional excitation is exponentially weak (at a distance of 7 mm from the solid target, the estimated values of N_e and T_e do not exceed $\sim 5 \times 10^{16}$ cm^{-3} and 2 eV, respectively). Then, we have

$$\frac{D_{13.5}}{D_{18.2}} = \frac{A_{42}W_3}{A_{32}W_4}\left(\frac{\sigma_3}{\sigma_4} + \frac{W_{43}}{W_4}\right)^{-1}\frac{k_{13.5}}{k_{18.2}},$$

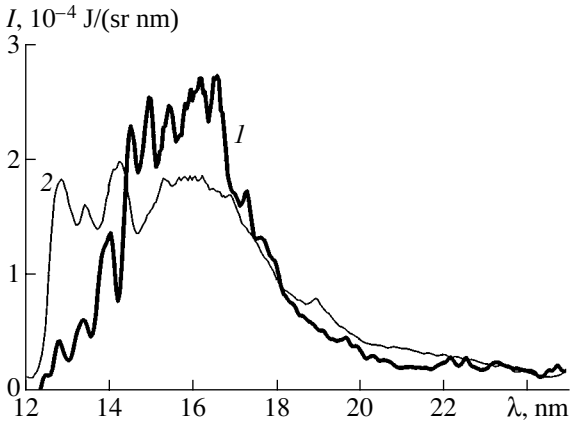

Fig. 9. Emission spectra from (*1*) a pulsed Xe target and (*2*) a plane solid tungsten target for the same exposures. In the case of the tungsten target, the observation direction is nearly parallel to the target surface.

where σ_3/σ_4 is the sought ratio between the cross sections of charge-exchange processes resulting in the excitation of the levels with $n = 3$ and 4 (it is assumed that $\sigma_5 \approx 0$), D_λ is the exposure in the corresponding lines, k_λ is the sensitivity (in units of photon/mm^2) of the recording system (this sensitivity is assumed to be constant), A_{ij} is the radiation transition probability for an $i \longrightarrow j$ transition, $W_{43} = A_{43} + N_e c(4, 3)$ is the total probability (in s^{-1}) of the $4 \longrightarrow 3$ transition with a minor correction for collisional deexcitation, $W_n = A_n + N_e c(n, n-1)$ is the total probability of quenching the nth level, and $c(n, n-1)$ is the collisional quenching rate of the nth level. In the plasma–gas interaction region, where the levels are populated via charge exchange, the ratio $D_{18.2}/D_{13.5}$ is 3 ± 1. In the limit $N_e \longrightarrow 0$, this corresponds to the ratio $\sigma_3/\sigma_4 = 1.7^{+0.7}_{-0.7}$. Considering N_e to be nonzero in the interaction region leads to a minor change in this value. For example, at $N_e = 5 \times 10^{16}$ cm^{-3}, we have $\sigma_3/\sigma_4 = 1.6^{+0.7}_{-0.6}$.

4. CLEAN SXR SOURCE

We also performed experiments on creating a clean (debris-free) SXR source excited by laser pulses focused into a pulsed Xe jet. The diagnostic complex used to measure the source parameters is shown in Fig. 7. An X-ray image of a source at the wavelength 18 nm was obtained using a focusing MM (see Fig. 8). In the horizontal direction, the effective width of the source is ~0.2 mm and the full width is ~0.4 mm. The height of the emitting region is about 0.7 mm. Figure 9 shows the absolute X-ray yield measured with an AXUV-5 X-ray photodiode and the radiation spectrum in the wavelength range of 12.5–25 nm. The absolute spectral luminosity at a wavelength of 18 nm in the direction perpendicular to the propagation direction of the laser beam and the jet axis (Fig. 7) is 1.1×10^{-4} J/(sr nm). Assuming that the plasma luminosity is isotropic, we find that the conversion efficiency of laser radiation is about 3×10^{-4} (sr nm)$^{-1}$. It is found that the source parameters in the wavelength range $\lambda < 14.5$ nm are determined by photoabsorption at the periphery of the gas jet.

5. CONCLUSIONS

Spectroscopic studies of the interaction of noble gas (Kr, Xe, He) jets with a laser plasma ejected from a solid target were carried out in a wavelength range of $\lambda > 12.5$ nm. The SXR line emission from the plasma–gas interaction region was shown to be caused by the charge exchange of multicharged ions with noble gas atoms via the Landau–Zener mechanism.

A compact repetitively pulsed debris-free SXR laser plasma source excited in a pulsed Xe jet by a focused laser beam has been created.

ACKNOWLEDGMENTS

This study was supported in part by the Integratsia Russian Federal Program (project no. B-0049), the Optical Spectroscopy and Frequency Standards Fundamental Research Program of the Department of Physical Sciences of the Russian Academy of Sciences, and the Russian Federal Program on State Support of Leading Scientific Schools (grant nos. NSh-1254.2003.2 and CRDF Y1-P-11-04).

REFERENCES

1. L. P. Presnyakov and V. P. Shevel'ko, Pis'ma Zh. Éksp. Teor. Fiz. **13**, 286 (1971) [JETP Lett. **13**, 203 (1971)].
2. A. V. Vinogradov and I. I. Sobel'man, Zh. Éksp. Teor. Fiz. **63**, 2113 (1972) [Sov. Phys. JETP **36**, 1115 (1972)].
3. L. P. Presnyakov and A. D. Ulantsev, Kvantovaya Élektron. (Moscow) **1**, 2377 (1974).
4. R. C. Isler, Phys. Rev. Lett. **38**, 1359 (1977).
5. R. H. Dixon, J. F. Seely, and R. C. Elton, Phys. Rev. Lett. **40**, 122 (1977).
6. M. G. von Hellermann, W. Mandl, H. P. Summers, *et al.*, Rev. Sci. Instrum. **61**, 3479 (1990).
7. I. L. Beĭgman, A. S. Pirozhkov, and E. N. Ragozin, Pis'ma Zh. Éksp. Teor. Fiz. **74**, 167 (2001) [JETP Lett. **74**, 149 (2001)].
8. V. G. Kapralov, R. Korde, V. E. Levashov, *et al.*, Kvantovaya Élektron. (Moscow) **32**, 149 (2002).
9. V. V. Kondratenko, V. E. Levashov, Yu. P. Pershin, *et al.*, Kratk. Soobshch. Fiz., No. 7, 32 (2001).
10. S. Yu. Zuev, V. V. Kondratenko, V. E. Levashov, *et al.*, in *Proceedings of the All-Russia Conference on X-ray Optics, Nizhni Novgorod, 2002*, p. 52.
11. E. N. Ragozin, V. V. Kondratenko, V. E. Levashov, *et al.*, Proc. SPIE **4782**, 176 (2002).

Translated by N.N. Ustinovskiĭ

Plasma Physics Reports, Vol. 30, No. 2, 2004, pp. 154–158. Translated from Fizika Plazmy, Vol. 30, No. 2, 2004, pp. 175–179.

PLASMA DIAGNOSTICS

Diagnostics of a High-Temperature Laser Plasma by Measuring the Spectral and Temporal Parameters of the $3\omega_0/2$-Harmonic Emission

V. N. Kondrashov

Troitsk Institute for Innovation and Fusion Research, Troitsk, Moscow oblast, 142190 Russia

Received July 24, 2003

Abstract—The results of measurements of the spectral and temporal parameters of the $3\omega_0/2$-harmonic emission in experiments on irradiating burning-through thin foils by laser pulses with intensities of $\sim 10^{14}$ W/cm^2 are presented and analyzed. The time-dependent scale length of the plasma density and the temperature at a level of one-fourth the critical density are estimated from the measured splitting between the spectral components and the measured ratio of their intensities by using a simplified model that takes into account the detailed mechanism for $3\omega_0/2$-harmonic generation. © *2004 MAIK "Nauka/Interperiodica".*

1. INTRODUCTION

The possibility of using the spectral and temporal parameters of the $3\omega_0/2$-harmonic emission (where ω_0 is the frequency of the heating laser radiation) to measure the parameters of laser-produced inhomogeneous high-temperature plasma is restricted by the fact that the mechanisms for generating this harmonic are incompletely understood. The $3\omega_0/2$-harmonic emission has been studied in many papers (see [1] and the literature cited therein). In early investigations [2, 3], the $3\omega_0/2$-harmonic generation in a laser-produced plasma was explained as being due to the following two effects: a sequence of the processes of excitation of Langmuir waves in two-plasmon decay instability in the regions where the plasma density is about one-fourth the critical density ($n_c/4$) and the subsequent Thomson upscattering of the heating laser beam by these waves. These views about the harmonic generation mechanisms were confirmed by measurements of the harmonic emission spectrum, which was found to consist usually of two components—red and blue broad peaks (see, e.g., [3, 4] and the literature cited therein). Many regular features of the phenomenon in question (in particular, the threshold for two-plasmon decay instability and its saturation, as well as the correlation of the $3\omega_0/2$-harmonic emission intensity with the generation of fast electrons) were observed and discussed in further experimental and theoretical papers. Based on the results of these investigations, a method was proposed and approved for determining the local electron temperature T_e from the splitting $\Delta\lambda_{3/2}$ between the components in the spectrum of the generated harmonic (we note that this method gives somewhat overestimated values of the temperature T_e as compared to other methods [5]). At the same time, many details of the mechanism for harmonic generation in a laser plasma corona are still controversial and remain to be clarified (thus, in a number of papers, the blue spectral component was not observed at all). The authors of some papers [6, 7] doubted the possibility of using the $3\omega_0/2$ harmonic emission to diagnose the parameters of a laser plasma and the turbulence in it. They proposed explaining the features of the harmonic spectrum as being due to a more complicated sequence of processes: (i) two-plasmon decay, (ii) decay of a primary plasmon into a plasmon and a phonon, and (iii) Raman scattering of the heating laser light by the secondary plasmons. The problem of clarifying the mechanism for the generation of the $3\omega_0/2$-harmonic emission is still of interest and requires more extensive experimental investigations with additional diagnostic tools. One can hope that checking such regular features as the dependences of the harmonic emission intensity on the plasma-density scale length L ($L = [n/dn/dx]_{n = n_c/4}$), plasma temperature, and target material will make it possible to determine the processes that play the dominant role in harmonic generation.

The aim of this paper is to analyze the spectral and temporal parameters of the $3\omega_0/2$-harmonic emission that have been obtained in experiments at moderate laser intensities [8]. The analysis is carried out in terms of the linear theory of two-plasmon decay instability [3, 4]. A simplified model of harmonic generation is developed and used as a basis for discussing the possibility of determining the plasma-density scale length L from the measured intensities of the red and blue components in the harmonic spectrum.

2. EXPERIMENT

New arguments clarifying the main mechanism for the $3\omega_0/2$-harmonic generation have been provided by

1063-780X/04/3002-0154$26.00

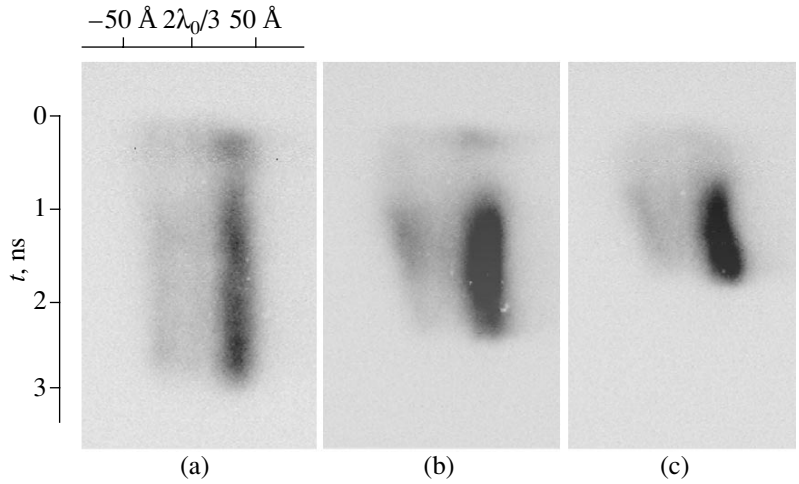

Fig. 1. Streak images of the $3\omega_0/2$-harmonic emission spectra in experiments with Mylar targets with thicknesses of (a) 3, (b) 1.5, and (c) 0.8 μm. The laser intensity is $I = 10^{14}$ W/cm^2.

the spectral and temporal data from recent experiments on laser irradiation of polymer and metal foils that burned through during the laser pulse and of thick targets made of low-density porous materials [8]. These experiments were carried out in the Mishen facility with the following parameters of laser radiation: the wavelength was 1.055 μm, the spectral width was <0.5 Å, the pulse duration at the base was ~3 ns, the contrast was ~10^6, and the energy was as high as 100 J. The mean laser intensity achieved with a focusing lens (f/10) at nearly normal incidence of the laser beam on the target in the vacuum chamber was varied within the range of 5×10^{13}–2×10^{14} W/cm^2, in which case the thresholds for two-plasmon decay instability were overcome for all types of targets used in experiments. The spectral and temporal parameters of the $3\omega_0/2$-harmonic emission collected in the aperture of the focusing lens were analyzed (with spectral and temporal resolutions of ~1 Å and ~ 50 ps, respectively) by a combination of an MDR-3 diffraction monochromator and an Agat streak camera. The images at the exit from the streak camera, which provided the time scans of the harmonic spectra, were recorded by means of a Leptonar 1P-4.5 objective and a VS-tandem/s 56 video system connected to a PC.

Let us consider Fig. 1, which shows typical streak images of the $3\omega_0/2$-harmonic emission spectra recorded in experiments with planar Mylar films with thicknesses of d = (a) 3, (b) 1.5, and (c) 0.8 μm [8]. The spectra are seen to consist of two components, the red component being far more intense than the blue. At the beginning of the $3\omega_0/2$-harmonic generation process, a short intense spike is often observed in the time behavior of both components. As a rule, the intensity of the $3\omega_0/2$-harmonic emission increases slower than does that of the pump laser pulse (at the frequency ω_0). For polymer targets, the intensities of the red and blue components reach their maxima when the laser pump intensity is already decreasing. For targets with thicknesses of up to ~2 μm, the emission duration of both components is shorter than the laser pulse duration. This indicates that, during the irradiation, the maximum plasma density in the interaction region falls below one-fourth of the critical density. It follows from the experimental data (Fig. 1) that Mylar targets thinner than 3 μm burn through in the course of irradiation; i.e., as the heated plasma expands, its maximum density falls below the critical density n_c and becomes even lower than $n_c/4$. For targets of thickness 3 μm and more, the maximum density does not fall below one-fourth of the critical density during irradiation. The spectral distribution of the intensity of harmonic emission from the foils that burn through (Figs. 1b, 1c) is seen to change with time. However, such issues as the interpretation of the spectral shifts, the asymmetry of the spectrum with respect to the exact frequency value $3\omega_0/2$ due to the plasma motion, and the short-wavelength cutoff of the blue component (Figs. 1b, 1c) go beyond the scope of the present paper, although, in principle, information about the velocity profile in the plasma corona of burning-through targets can be derived from an analysis of the Doppler shift measurements at different harmonic frequencies (ω_0, $3\omega_0/2$, and $2\omega_0$). Note that, by the time at which the target has burned through, the plasma regions where the density is equal to n_c or $n_c/4$ move in the propagation direction of the heating laser beam.

3. ANALYSIS OF THE EXPERIMENTAL DATA

The above experimental data were used to study the time evolutions of the red and blue spectral components and the ratio of their intensities. As an example, Fig. 2 shows the time evolution of the intensity ratio between

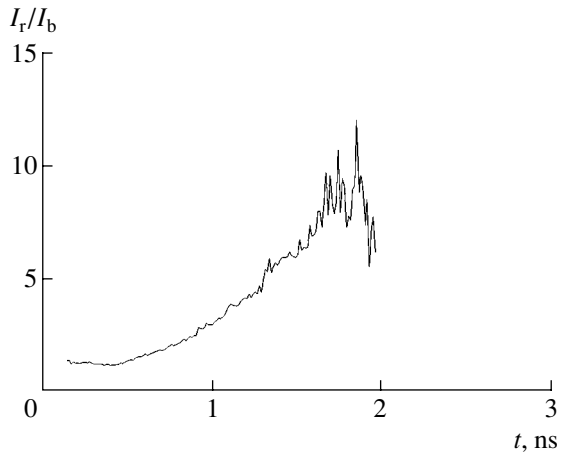

Fig. 2. Intensity ratio between the red and blue components, I_r/I_b, in the $3\omega_0/2$-harmonic emission spectrum measured in experiments on irradiating a 1-μm aluminum foil by laser light with an intensity of 2×10^{14} W/cm^2.

the red and blue components, I_r/I_b, in the $3\omega_0/2$-harmonic emission spectrum measured in the experiment on irradiating a 1-μm aluminum foil by laser light with an intensity of 2×10^{14} W/cm^2. Note that, in order to increase the accuracy of the measurements of the intensity ratio between the red and blue components, the red component was attenuated (by a factor of 5) by a thin neutral filter. The figure shows that, up to the time at which the foil has burned through (~2 ns), the intensity ratio I_r/I_b increases monotonically up to a value of ~8. At other times, the red and blue components are indistinguishable against the background signal, so that their intensity ratio becomes meaningless. It is reasonable to associate the increase in the ratio I_r/I_b with the dynamics of the expanding plasma, since it is well known [3, 4] that the threshold and amplification of convective two-plasmon decay instability depend on the plasma-density scale length L. An analysis of the above experimental data by the model described below shows that the characteristic scale length L increases in time (for the data of Fig. 2, the scale length L increases to about 150 μm by the second nanosecond), which is quite natural for the dynamics of burning-through foils [9].

In analyzing the intensities of the components of the $3\omega_0/2$-harmonic emission spectrum, it is necessary to consider the particular diagram of the wave interaction. It is well known that two-plasmon decay far above the instability threshold gives rise to plasmons with a broad **k** spectrum. In the experiments in [8], the heating laser radiation was focused on the target by a lens with a fairly large value of f/d (~10) and the radiation emitted from the plasma at the frequency $3\omega_0/2$ was focused by the same lens. In this case, at nearly normal incidence of the pump wave on the target and when the observations are made in the direction opposite to that of the incident laser beam, the mechanism for generating $3\omega_0/2$-harmonic photons becomes far simpler to analyze, because, of the entire spectrum of plasmons produced in the three-wave interaction, it is sufficient to consider only longitudinal plasma waves with a zero transverse wave-vector component $k_\perp$. Each of the red photons ($\omega_r < 3\omega_0/2$) emitted from the plasma and recorded in the experiments is produced from the merging of a pump photon with a red plasmon that propagates in the plasma from the point of two-plasmon decay toward the region of lower density. The blue component ($\omega_b > 3\omega_0/2$) in the observed spectrum is thought to form through several theoretically possible mechanisms [3, 5]: (i) the merging of a pump photon with a blue plasmon that propagates along the density gradient toward the region of higher density and is reflected from the region with the density ~$n_c/4$; (ii) the merging of a pump photon reflected from the region with the critical density (n_c) with a blue plasmon propagating toward the region of higher density, followed by the reflection of the generated $3\omega_0/2$-harmonic photon from the region with the density ~$9n_c/4$; and (iii) the merging of a pump photon with a blue plasmon that propagates toward the region of higher density, followed by the reflection of the generated blue photon from the region with the region with the density ~$9n_c/4$. In experiments on irradiating thin polymer foils (thinner than 2 μm) and thin metal foils (thinner than 1 μm) [8], the time during which the $3\omega_0/2$ harmonic was emitted was shorter than that in experiments with thick targets, in which the harmonic was generated throughout the entire laser pulse (Fig. 1). Although the maximum density of the expanding plasma produced by laser irradiation of these burning-through thin foils fell even below one-fourth the critical density ($n_c/4$) during the laser pulse, the intensities of the spectral components at the times at which the plasma density was equal to $9n_c/4$ or n_c were observed not to decrease sharply, and the spectral shifts at these times did not exhibit any unusual temporal behavior [8]. These experimental results provide evidence in favor of mechanism (i) and confirm the estimates made in [10].

4. MODEL

Here, for the chosen mechanism of the wave interaction, we determine which of the plasma parameters can be derived from the above experimental data. The electron temperature in the laser plasma corona was estimated from the formula [2, 5] $\Delta\omega_{b,r} \approx \pm 9/8\omega_0(V_{T_e}/c)^2$. Under the conditions of our experiments, the distance between the spectral components, $\Delta\lambda_{3/2}$, increases from 30 to 60 Å with increasing laser intensity and atomic number Z of the target foil material (we used polystyrene, Mylar, aluminum, titanium, copper, nickel, and scandium foils). The calculated electron temperature T_e was found to be from 0.6 to 1.2 keV.

The intensity ratio I_r/I_b between the red and blue components in the spectra of the $3\omega_0/2$-harmonic emission from a plasma with a specified electron temperature T_e and an exponential electron density profile characterized by the scale length L was calculated from a simplified numerical model in the following three steps. First, for the chosen mechanism of three-wave interaction, the wavenumbers of the generated plasmons were calculated from the energy and momentum conservation equations with allowance for the dispersion of electromagnetic and Langmuir waves in the plasma. This step also implies the calculation of the points x_0, $x_{3/2,\,b}$, and $x_{3/2,\,r}$ in the plasma density profile that correspond to the two-plasmon decay, the reflection of the blue plasmon, and the generation of the blue and red components of the $3\omega_0/2$-harmonic emission, respectively. Second, the amplification coefficient χ of the generated Langmuir waves was calculated for the excitation conditions of convective two-plasmon decay instability (the amplification coefficients were the same for both of the plasmons) [2, 10]:

$$\chi = (v_E/v_{T_e})^2 k_0 L/24,$$

where v_{T_e} is the electron thermal velocity, v_E is the electron oscillatory velocity in the region where the plasma density is about one-fourth the critical density, and k_0 is the wavenumber of the incident electromagnetic wave in this region. Finally, we calculated the integral attenuation coefficients τ_b and τ_r of the blue and red plasmons due to collisional damping during their propagation to the points at which they merged with the pump photons (the absorption of the incident laser radiation and the emitted harmonic in the plasma corona at $n < n_c/4$ is insignificant and was not taken into account):

$$\tau_{b,r} = \int_{x = x_0}^{x_{3/2,\,b,r}} \frac{\nu_{ei}(x)}{v_g(x)} dx,$$

where $\nu_{ei}(x)$ is the electron–ion collision frequency, $v_g(x)$ is the group velocity of the plasma wave, and x is the spatial coordinate in the direction of $\mathbf{k}_0$. For the above temperatures at the points $x_{3/2,\,b,\,r}$, at which the $3\omega_0/2$ harmonic is generated, the wavenumbers of the plasmons did not exceed $0.3/\lambda_D$ (where λ_D is the Debye radius), so that Landau damping can be ignored. The change in the radiation intensity at the frequencies ω_0 and $3\omega_0/2$ due to the classical collisional damping in the plasma region under consideration was also ignored. The intensities of the components of the $3\omega_0/2$-harmonic emission spectrum were proportional to $I_0(t)W_l(t)\exp(2\pi\chi - \tau_{b,\,r})$ (where I_0 is the heating radiation intensity and $W_l(t)$ is the spectral density of the energy flux of the Langmuir waves) [11], and their ratio was proportional to $I_r/I_b \sim \exp(\tau_b - \tau_r)$. It is important to note that the arguments of the exponentials depend on the atomic number Z of the target material and also on T_e and L. By analyzing the temporal behavior of the harmonic emission and the intensity ratio of the spectral components, it is possible to study Langmuir turbulence (and, accordingly, the development of two-plasmon decay instability) in the region where the plasma density was about one-fourth the critical density and also to estimate how the electron plasma density profile changes. Figure 3 shows the results of calculations of the intensity ratio I_r/I_b between the red and blue components in the $3\omega_0/2$-harmonic emission spectrum as a function of the scale length L of the plasma density at fixed values of the electron temperature of the plasma produced by irradiating a Mylar target. It can be seen that the intensity ratio between the red and blue components increases exponentially with L. As T increases, a less intense collisional damping of Langmuir waves leads to a smaller difference between the intensities of the components of the emitted harmonic. It should be noted that the actual streak cameras have limited dynamic range; hence, for any temperature, the values of the scale length L can be found such that the intensity of the blue component of the $3\omega_0/2$-harmonic emission spectrum does not exceed the background level, provided that the red component is recorded in the linear regime. Therefore, it is natural to expect that the spectrum of the harmonic emitted from the extended coronas characteristic of laser fusion targets (and also under the conditions corresponding to preheated targets) will contain only one (red) component.

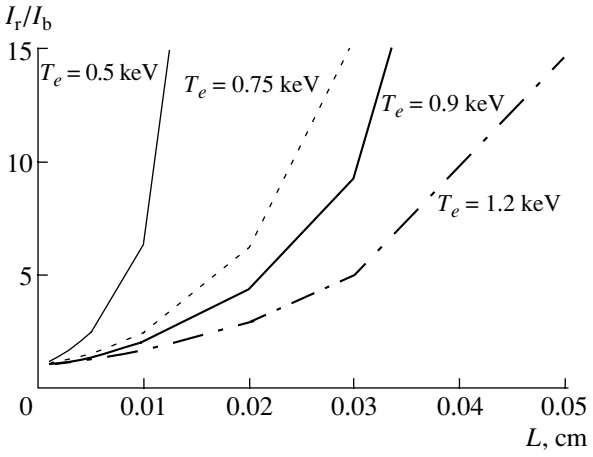

Fig. 3. Calculated dependence of the intensity ratio between the red and blue components, I_r/I_b, in the $3\omega_0/2$-harmonic emission spectrum on the plasma-density scale length L at fixed values of the electron temperature T_e.

5. CONCLUSIONS

In this paper, an analysis has been made of the regular features of the $3\omega_0/2$-harmonic emission in the interaction of high-power (5×10^{13}–2×10^{14} W/cm^2) neodymium laser pulses with burning-through planar targets. The experimental data on the spectral and tem-

poral parameters of harmonic generation are satisfactorily explained by linear theory. Along with the splitting between the red and blue components in the $3\omega_0/2$-harmonic emission spectrum, the time evolutions of the components and their intensity ratio can be used to estimate such important parameters of a nonuniform high-temperature plasma as the electron temperature and the scale length of the density profile. The diagnostic method proposed here, on the one hand, imposes restrictions on both the angles of incidence of the laser beam on the target and the focusing of the backscattered radiation emitted at the frequency $3\omega_0/2$ and, on the other hand, implies the use of measurement equipment with a sufficiently broad dynamic range. It should be noted that, in order to test the diagnostic method, it is necessary to make a detailed comparison of its results with data obtained from other diagnostics.

ACKNOWLEDGMENTS

I am grateful to N.G. Koval'skiy and V.Yu. Bychenkov for discussing the results obtained and to the Mishen team for their help in carrying out the experiments. This work was supported in part by the Russian Foundation for Basic Research (project no. 01-02-17336) and INTAS (grant no. 2001-0572).

REFERENCES

1. N. G. Basov, Yu. A. Zakharenko, N. N. Zorev, *et al.*, in *Itogi Nauki Tekh., Ser. Radiotekhnika* (VINITI, Moscow, 1982), Vol. 26, Part 1.
2. H. A. Baldis, E. M. Campbell, and W. L. Kruer, *Handbook of Plasma Physics*, Vol. 3: *Physics of Laser Plasmas*, Ed. by A. M. Rubenchik and S. Witkowski (North-Holland, Amsterdam, 1991), p. 361.
3. V. V. Aleksandrov, S. I. Anisimov, M. V. Brenner, *et al.*, Zh. Éksp. Teor. Fiz. **71**, 1826 (1976) [Sov. Phys. JETP **44**, 958 (1976)].
4. E. Z. Gusakov, Pis'ma Zh. Tekh. Fiz. **3**, 1219 (1977) [Sov. Tech. Phys. Lett. **3**, 504 (1977)].
5. *Diagnostic of Dense Plasmas*, Ed. by N. G. Basov (Nauka, Moscow, 1989), p. 91.
6. D. F. DuBois, D. A. Russell, and H. A. Rose, Phys. Rev. Lett. **74**, 3983 (1995).
7. Laboratory for Laser Energetics Reviews (University of Rochester) **57**, 27 (1993).
8. V. N. Kondrashov, G. M. Yankovskii, I. N. Burdonskii, *et al.*, in *Inertial Fusion Sciences and Applications 2001*, Ed. by K. Tanaka, D. D. Meyerhofer, and J. Meyer-ter-Vehn (Elsevier, Paris, 2002), p. 319.
9. N. G. Basov, V. Yu. Bychenkov, A. A. Zozulya, *et al.*, Zh. Éksp. Teor. Fiz. **92**, 1700 (1987) [Sov. Phys. JETP **65**, 954 (1987)].
10. R. A. London and M. D. Rosen, Phys. Fluids **29**, 3813 (1986).
11. V. Yu. Bychenkov, A. A. Zozulja, V. P. Silin, and V. T. Tikhonchuk, Beitr. Plasmaphys. **23**, 331 (1983).

Translated by G.V. Shepekina

Plasma Physics Reports, Vol. 30, No. 2, 2004, pp. 159–163. Translated from Fizika Plazmy, Vol. 30, No. 2, 2004, pp. 180–184.

PLASMA DIAGNOSTICS

Studies of Runaway Electrons in the Globus-M Tokamak

A. E. Shevelev*, I. N. Chugunov*, V. K. Gusev*, Yu. V. Petrov*, V. V. Rozhdestvenskiĭ*, A. B. Mineev, N. V. Sakharov*, D. N. Doĭnikov*, A. L. Izotov*, S. V. Krikunov*, V. O. Naĭdenov*, K. A. Podushnikova*, I. A. Polunovskiĭ*, D. B. Gin*, and A. I. Chugunov***

** Ioffe Physicotechnical Institute, Russian Academy of Sciences, Politekhnicheskaya ul. 26, St. Petersburg, 194021 Russia*

*** Efremov Research Institute of Electrophysical Apparatus, St. Petersburg, 189631 Russia*

Received July 24, 2003

Abstract—Results are presented from experimental studies of runaway electrons in the ohmic heating regime in the Globus-M tokamak. The periodical hard X-ray bursts observed with the help of two hard X-ray spectrometers with high time resolution are attributed to MHD oscillations in the plasma core and at the periphery.

1. INTRODUCTION

One of the methods for studying fusion plasmas is the investigation of runaway electrons by analyzing hard X-ray emission arising due to deceleration of these electrons in the structural components of the vacuum chamber (limiters). A specific feature of runaway electrons is that their number and maximum energy depend on the plasma parameters and vary during the discharge. Such studies usually employ scintillation gamma spectrometry, which makes it possible to measure the energy spectrums of hard X-ray (HXR) emission [1, 2].

Interest in the studies of runaway electrons in spherical tokamaks (STs) is motivated by the fact that, in STs, the structure of the magnetic and electric fields in the plasma differs substantially from that in conventional tokamaks, giving rise to some new specific features in the particle behavior. Previous studies performed in the Globus-M spherical tokamak [3, 4] showed that the current of runaway electrons, which is usually dominant in conventional tokamaks in low-density regimes, is lower than 10–20% of the total plasma current even in regimes with very low plasma densities of $(0.15–0.3) \times 10^{19}$ m^{-3}. All attempts to reach discharge regimes with the dominant current of runaway electrons in the Globus-M tokamak were unsuccessful. Moreover, the maximum energy of runaway electrons (about 3 MeV) at very low densities did not increase with increasing plasma current. In the case of a major disruption in the final stage of the discharge, unlike in conventional tokamaks, no substantial population of runaway electrons was observed over a wide range of plasma parameters.

The present paper describes the experimental setup, as it was modified in order to study the behavior of runaway electrons in more detail, and presents the results obtained in this way.

2. EXPERIMENTAL SETUP

At present, two methods are used to study runaway electrons by analyzing HXR emission in the Globus-M tokamak (R = 0.36 m, a = 0.24 m, $B_T < 0.6$ T, and $I_p <$ 0.5 MA). The first (earlier) method uses a spectrometric analog-to-digital converter (ADC) that digitizes signals from the photomultiplier anode of a scintillation detector. The amplitude of this signal is proportional to the energy of a photon recorded by the detector. Prototypes of this device were used by us in the T-10, FT-2, and Tuman-3M tokamaks [5–7]. The second method uses a fast ADC, the operation of which is based on the periodical digitizing of signals from the scintillation detector. The high sampling rate (15 MHz) and the large data memory (128 MB) of the diagnostics allow us to trace variations in the photomultiplier anode voltage during the discharge and to reconstruct the time and energy distributions of HXR photons by processing the data obtained.

The next step in the development of the experimental base was the installation of the second NaI (Tl) scintillation detector. Figure 1 shows the arrangement of the detectors. Both detectors are protected from scattered radiation by lead blocks and have collimators directed to the corresponding limiters in the equatorial plane of the tokamak chamber. The signal from detector D1 (a NaI (Tl) crystal 150 mm in diameter and 100 mm in length) is processed by both the spectrometric ADC and the first fast ADC. The signal from detector D2 (a NaI

1063-780X/04/3002-0159$26.00 © 2004 MAIK "Nauka/Interperiodica"

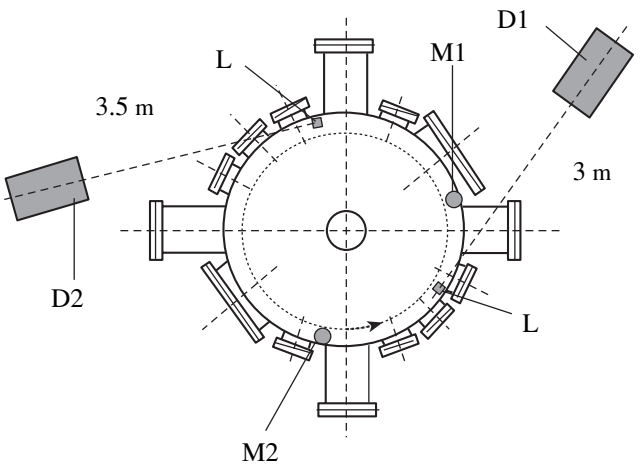

Fig. 1. Arrangement of scintillation detectors D1 and D2 relative to the tokamak vacuum chamber (top view): (L) limiters toward which collimators are directed and (M1, M2) Mirnov coils. The distances from detectors D1 and D2 to the corresponding limiters are 3 and 3.5 m, respectively. The arrow shows the rotation direction of runaway electrons.

(Tl) crystal 70 mm in diameter and 70 mm in length) is processed by the second fast ADC. The measurements are usually performed in the energy range 0.1–8 MeV, which, however, can be extended to 20 MeV. The spectrometric system is activated by the start pulse of the tokamak, which ensures synchronization with other diagnostics.

Figure 2 shows the electronic block diagram of the diagnostic system, which consists of two blocks. One of them (B1) is made in the CAMAC standard, whereas the other (B2) is integrated in a PC. The time during which block B1 measures each single energy spectrum can be varied from 10 μs to 100 ms. The number of energy spectra measured in one discharge is up to 128; therefore, the time interval in which each spectrum is measured is typically no shorter than 1 ms. This block allows us to obtain 128 energy spectra just after the plasma discharge and, consequently, to determine the time behavior of the X-ray intensity with a fixed time step that is specified before the measurements. From the energy spectra, we can estimate the maximum energy of runaway electrons at different instants during the discharge.

The high sampling rate of block B2, which is based on fast ADCs (Fig. 2), and its large data memory (128 MB) allow us to trace the escape dynamics of the accelerated electron beam onto the tokamak wall with high time resolution. Since the waveform of the photomultiplier anode voltage during the discharge is stored in the computer memory, we can use it to reconstruct the time and energy distributions of X-ray photons. It is well known [8, 9] that, in the linear range of a scintillation spectrometer, the pulse shape does not depend on its amplitude and is determined by the deexcitation

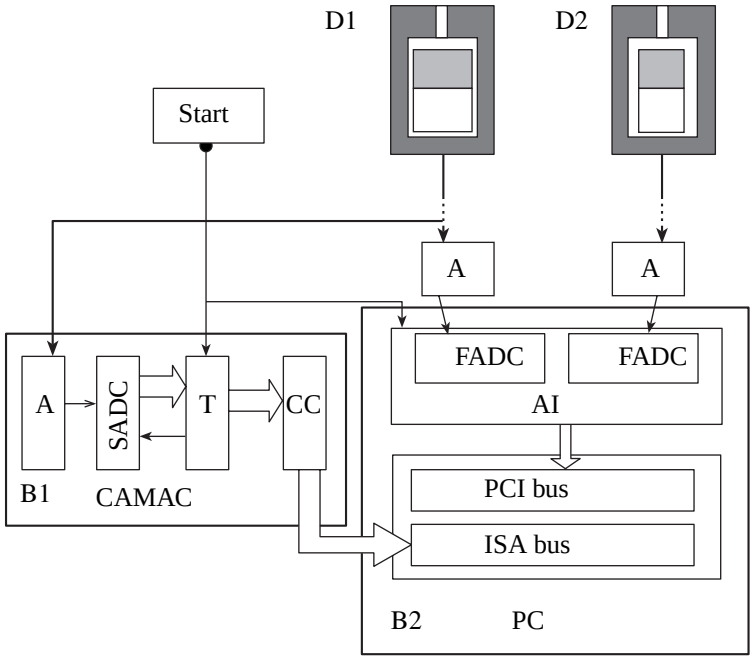

Fig. 2. Block diagram of the measurement system: (D1, D2) detectors, (B1) CAMAC block, (B2) measurement block integrated into a PC, (A) amplifiers, (SADC) spectrometric ADC, (T) timer, (CC) crate controller, (FADC) fast ADC, and (AI) analog input.

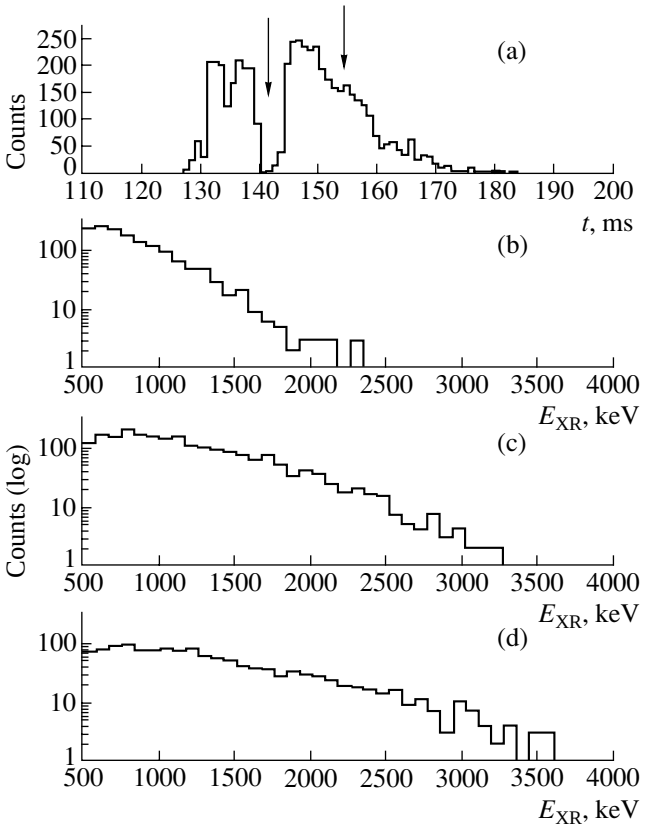

Fig. 3. (a) Time dependence of the HXR intensity measured in shot no. 5926 and the HXR spectra integrated over the time intervals (b) 100–142, (c) 142–154, and (d) 154–190 ms. The arrows in plot (a) show the boundaries of the time intervals.

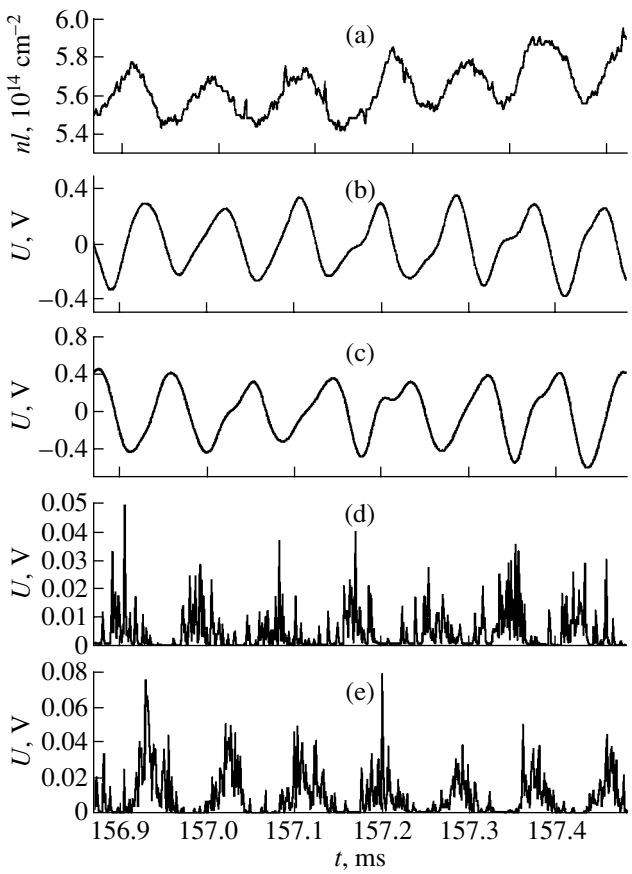

Fig. 4. (a) Waveform of the plasma density averaged over the vertical chord R = 42 cm in shot no. 5660 and signals from (b) Mirnov coil M1, (c) Mirnov coil M2, (d) HXR detector D1, and (e) HXR detector D2. The period of HXR bursts is 85 μs.

time of the crystal and by the RC constants of the circuit elements. To a high degree of accuracy, the signal shape is described by the formula:

$$U(E,t) = A(E)\left(1 - e^{-\frac{t-t_0}{\tau_1}}\right)^P e^{-\frac{t-t_0}{\tau_2}},$$

where $A(E)$ is the signal amplitude, proportional to the measured photon energy; t_0 is the signal start time; and τ_1, τ_2, and P are parameters that depend on a particular electronic scheme of signal conversion and on the time characteristics of the crystal deexcitation pulse, which are determined from the measured shape of individual pulses. In processing the data stored during the discharge, a special program is used to separate superimposed pulses, calculate their amplitudes, and plot the amplitude spectra (energy distributions). The time intervals in which the amplitude spectrum is plotted can be specified and changed by an operator in the course of processing. Figure 3 shows (a) the time dependence of the HXR intensity measured during shot no. 5926 and (b–d) three energy spectra integrated over different time intervals. The maximum energy of HXR photons in these time intervals is 2.3, 3.3, and 3.6 MeV, respectively. The corresponding time intervals are shown in Fig. 3a by the arrows.

3. RESULTS AND DISCUSSION

The above diagnostics, consisting of two detector units, the signals from which were processed by both a spectrometric ADC and new fast ADCs, was applied to studying runaway electrons in the Globus-M tokamak in the ohmic heating regime (OH) over a wide range of the plasma parameters. The plasma current was varied from 0.1 to 0.25 MA, the plasma density was varied over the range of $(0.5–5) \times 10^{19}$ m^{-3}, and the magnetic field on the plasma axis was varied from 0.29 to 0.45 T. The results obtained were analyzed simultaneously with the data from the detectors of MHD oscillations, soft X-ray (SXR) detectors, and an HXR flux detector.

The simultaneous use of two HXR spectrometers with fast ADCs allowed us to detect a sequence of bursts with a period of 0.07–1.5 ms against the background of continuous HXR emission during the dis-

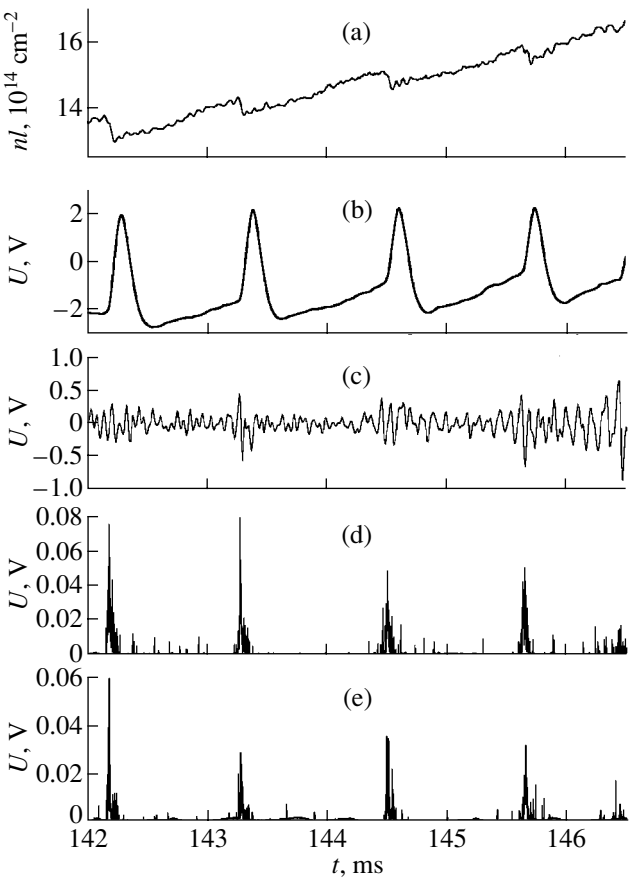

Fig. 5. (a) Waveform of the plasma density averaged over the vertical chord R = 42 cm in shot no. 6557 and signals from (b) an SXR detector, (c) Mirnov coil M1, (d) HXR detector D1, and (e) HXR detector D2. The period of HXR bursts is 1100 μs.

charge current plateau. It turned out that HXR bursts with a period in the range of 70–300 μs correlated with developed MHD oscillations measured by Mirnov coils, whereas bursts with a period of 400–1500 μs correlated with sawtooth oscillations of the SXR signal from the plasma core.

In discharges with developed MHD oscillations, the period of HXR bursts in the stage of the current plateau coincided with the period of MHD oscillations. Figure 4 shows the waveforms of oscillations measured by Mirnov coils MHD-1 and MHD-2 and signals from two HXR detectors (shot no. 5660, I_p = 95 kA, and n_e = 1.3×10^{19} m^{-3}; the arrangement of probes and detectors is shown in Fig. 1). In this case, the phase shift between the signals from two probes spaced at an angle of 115° along the torus corresponds to the m/n = 2/1 mode. The phase shift between the signals from the HXR detectors also corresponds approximately to the m/n = 2/1 mode, taking into account the relative positions of the limiters spaced at an angle of 135° along the torus and viewed by the HXR detectors. It follows from the signal behavior that the periodicity of HXR bursts is related to the modulation of the runaway electron flux onto the limiters by the rotating magnetic islands of the developed m/n = 2/1 mode.

In discharges with developed sawtooth oscillations, HXR bursts with periods of longer than 350 μs were in phase for both detectors and correlated well with the magnetic reconnection phase. In Fig. 5 (shot no. 6557, I_p = 190 kA, and $n_e = 4 \times 10^{19}$ m^{-3}), signals from the Mirnov coils show weak MHD activity at the plasma periphery. In this case, the waveforms of both the density integrated over the central chord and the SXR signal display sawtooth oscillations with a period of 1.0–1.1 ms. Every reconnection phase is accompanied by intense HXR bursts, whose intensity is usually higher than the background level by a factor of 10–100. Apparently, these bursts are related to the escape of a fraction of the accelerated electron beam from the region $q \le 1$ onto the plasma periphery during magnetic reconnection. The synchronism between the signals from both detectors corresponds to the m/n = 0/0 mode.

In recent experiments, an ohmic heating regime with a current of I_p = 150–200 kA in the plateau phase was achieved at a loop voltage lower than in previous experiments [3] and, consequently, at a lower vortex electric field E. In this regime, the electron density profile is broader and the level of plasma MHD activity in the quasi-steady stage of the discharge is low. In spite of the rather small ratio between the mean values of the vortex field E and the Dreicer field ($E/E_{cr} < 2\%$) in this discharge stage, we detected HXR emission with a maximum photon energy of 5–7 MeV; this was markedly higher than in the previous experiments (3 MeV). This fact is evidence of the improved confinement of runaway electrons, and consequently, of an increase in their lifetime.

4. CONCLUSIONS

The use of two HXR spectrometers with high time resolution in experiments carried out in the Globus-M spherical tokamak made it possible to detect HXR bursts correlating with different MHD modes. The increased energy of HXR photons in regimes with a loop voltage lower than in the previous experiments points to the improved confinement of runaway electrons.

ACKNOWLEDGMENTS

This work was supported in part by the Sixth Competition of Scientific Projects for Young Scientists of the Russian Academy of Sciences (project no. 12), the Russian Foundation for Basic Research (project no. 03-02-17659), and the Dynasty Foundation.

REFERENCES

1. S. V. Mirnov, *Physical Processes in Tokamak Plasma* (Énergoatomizdat, Moscow, 1983).

2. N. A. Vartanov and P. S. Samoĭlov, *Applied Scintillation Gamma Spectrometry* (Atomizdat, Moscow, 1969).

3. V. K. Gusev, I. N. Chugunov, A. V. Dech, *et al.*, in *Proceedings of the 29th EPS Conference on Plasma Physics and Controlled Fusion, Montreux, 2002*; ECA **26B**, 4.104 (2002).

4. A. S. Anan'ev, V. K. Gusev, S. V. Krikunov, *et al.*, in *Proceedings of the 12th Joint Workshop on Electron Cyclotron Emission and Electron Cyclotron Heating, Aix-en-Provence, 2002*, p. 191; http://wshop.free.fr/ec12/PAPERS, 048-Rozhdestvensky.pdf.

5. E. P. Its, V. G. Kiptilyĭ, S. V. Krikunov, *et al.*, Fiz. Plazmy **20**, 24 (1994) [Plasma Phys. Rep. **20**, 18 (1994)].

6. L. A. Esipov, E. R. Its, V. G. Kiptilyĭ, *et al.*, Fiz. Plazmy **24**, 257 (1998) [Plasma Phys. Rep. **24**, 228 (1998)].

7. V. N. Budnikov, L. A. Esipov, E. R. Its, *et al.*, in *Proceedings of the 26th EPS Conference on Plasma Physics and Controlled Fusion, Maastricht, 1999*; ECA **23J**, 4.097 (1999); ECA **23J**, 1741 (1999).

8. A. I. Abramov, Yu. A. Kazanskiĭ, and E. S. Matusevich, *Basic Experimental Methods of Nuclear Physics* (Atomizdat, Moscow, 1970).

9. I. S. Krasheninnikov, S. S. Kurochkin, A. V. Matveev, and E. I. Rekhin, *Modern Nuclear Electronics* (Atomizdat, Moscow, 1974), Vol. 1.

Translated by E.L. Satunina

Plasma Physics Reports, Vol. 30, No. 2, 2004, pp. 164–168. Translated from Fizika Plazmy, Vol. 30, No. 2, 2004, pp. 185–189.

PLASMA DIAGNOSTICS

Formation of a Charge-Exchange Target for Fast Ions in the Plasma of Large-Scale Toroidal Devices under NBI Conditions

M. I. Mironov*, A. V. Khudoleev*, and Y. Kusama**

** Ioffe Physicotechnical Institute, Russian Academy of Sciences, Politekhnicheskaya ul. 26, St. Petersburg, 194021 Russia*

*** Japan Atomic Energy Research Institute, Naka-machi, Naka-gun, Ibaraki-ken, Japan*

Received July 24, 2003

Abstract—High-energy ($E > 0.2$ MeV) charge-exchange diagnostics allow the determination of the distribution function of fast atoms produced via the neutralization of hydrogen isotope ions by target hydrogen-like impurity ions. To derive the distribution function from the experimental data requires knowledge of the composition and spatial distribution of the target ions in a tokamak plasma. A charge-exchange target forms as a result of the interaction between the main impurity nuclei and the heating neutral beams. In different devices, the heating beams are arranged in different ways with respect to the diagnostics; hence, in order to accurately estimate the contribution of the secondary ions to the detected signal, it is necessary to calculate their trajectories for every particular case. A model is proposed that takes into account elementary processes resulting in the ionization equilibrium of the ions of different impurities with allowance for ion motion in a specific tokamak configuration. As an example, the model is applied to the plasma of the JT-60U tokamak. Mechanisms for the formation of charge-exchange atomic flows in various energy ranges are considered. The relative contributions of different heating injectors to the charge-exchange flow are estimated. Based on the calculated results, a method is proposed for local measurements of the ion distribution function with the help of a stationary analyzer. © *2004 MAIK "Nauka/Interperiodica".*

1. INTRODUCTION

High-energy ($E > 0.2$ MeV) charge-exchange diagnostics have long been employed to measure the distribution function of fast particles appearing in plasma in the course of fusion reactions, ion-cyclotron heating, or neutral beam injection (NBI). An analyzer detects the atoms that are produced due to charge exchange of fast ions with the target donor particles from which fast ions gain electrons to become fast atoms [1, 2]. Fast atoms are produced along the entire line of sight of the analyzer; hence, the detection signal is integral in character and can be expressed as follows:

$$J(E) \sim \int_L n_{\text{fast}}(E, l) \sum (n_{\text{donor}} \langle \sigma_{cx} v \rangle) Loss(E, l) dl, \quad (1)$$

where $J(E)$ is the detected atomic flux; L is the integration path; n_{fast} and n_{donor} are the densities of the fast and target ions, respectively; $\langle \sigma_{cx} v \rangle$ is the charge-exchange rate; and $Loss(E, l)$ is the attenuation of the output beam. The attenuation is mainly related to the ionization of atoms by plasma ions. In the absence of a neutral injector, the profile of the neutralization source along the line of sight of the analyzer has the form of a broad peak extended towards the plasma core. The peak usually occupies half of the plasma column and is more or less uniform in the poloidal and toroidal directions. As a rule, the source of fast particles is more localized than the neutralization source and the neutral particle spectrum detected by the analyzer is averaged over the region occupied by the former. Under the conditions of highly intense NBI that are typical of large devices, the target ions form mainly in the injection region due to charge exchange between the beam neutrals and plasma ions. The formed target spreads over the plasma; however, in large devices, it does not have enough time to occupy the entire plasma volume. The resulting distribution of the target ions is highly inhomogeneous, which complicates the interpretation of the measured particle fluxes.

One of the purposes of charge-exchange diagnostics is the reconstruction of the local ion distribution function (IDF). To this end, a target with a peaked profile whose width is much smaller than the region occupied by fast particles is produced with the help of diagnostic beams. However, this method cannot be applied to modern large-scale devices. The heating beams mentioned above also produce a charge-exchange target for fast ions and, hence, may appear to be helpful in performing local IDF measurements. The problem is complicated by the nonoptimal mutual disposition of the heating beams and neutral particle analyzers. The injector may be located in another cross section, so that the beam and the line of site of the analyzer do not inter-

1063-780X/04/3002-0164$26.00 © 2004 MAIK "Nauka/Interperiodica"

sect. Therefore, in order to determine the local target density at the analyzer site, it is necessary to consider in more detail the process of the formation and subsequent evolution of the target in a tokamak plasma.

2. TARGET FORMATION

In the high-energy range, the hydrogen ions exchange their charge mainly with hydrogen-like ions of the main impurities, such as Be^{3+} and C^{5+} (or with He^+ ions in the case of a helium plasma). These ions are generated in the plasma core due to the recombination and charge exchange of impurity nuclei with neutral particles arriving from the plasma periphery or, in the presence of high-power injection, due to the charge exchange of nuclei with fast beam atoms. In large tokamaks, the latter mechanism for the formation of hydrogen-like impurity ions is dominant. Fast atoms penetrating the plasma can be ionized due to their interaction with electrons, main plasma ions, and impurity ions. The atoms can also exchange their charge with the main plasma ions and impurity ions. The rate of charge exchange with impurities is rather high due to the relatively large cross section of this process. The probability of charge exchange with impurity ions is comparable to that of charge exchange with the main plasma ions, although the density of the impurity ions is substantially lower. Hence, a neutral beam penetrating the plasma gives rise to a cloud of thermal hydrogen-like ions whose density is usually several times higher than the beam density.

The generated ions begin to spread along the magnetic field lines in both directions along the torus and fall on the line of sight of the analyzer. The density of hydrogen-like ions along their propagation direction is determined by a number of processes. First, they may be ionized by the plasma electrons and ions. Furthermore, they may undergo charge exchange with the main plasma ions, yielding new hydrogen-like ions that move with a different velocity and, possibly, in the opposite direction. Therefore, some ions will move back to the ion source, thus enhancing the ion density in the vicinity of the beam. A similar effect is produced by another process related to the specific character of charged particle motion in a tokamak: the reflection of trapped particles from magnetic mirrors.

In view of the variety of processes outlined above, as well as the complexity of a particular experimental geometry, it obviously makes sense to perform numerical simulations in order to determine the distribution of the target ion density in a tokamak plasma.

3. NUMERICAL CODE

A computer code based on the Monte Carlo method for calculating the 3D distribution of the target ions was developed with regard for the following factors:

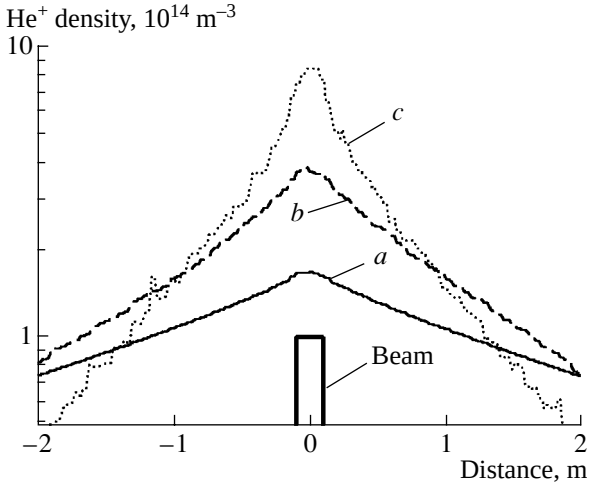

Fig. 1. Influence of different processes on the propagation of target ions: (*a*) electron-impact ionization, (*b*) ionization + charge exchange with the main plasma ions, and (*c*) ionization + charge exchange + reflection from magnetic mirrors.

(i) the real geometry of the heating neutral beams, including the number and arrangement of the sources in the injectors, the distribution of the source intensities over energy, and the transverse beam profiles;

(ii) the real plasma geometry, i.e., the real configuration of the magnetic field and 2D distributions of the plasma density and temperature;

(iii) the atomic processes accompanying the beam injection into the plasma and the generation and propagation of the target ions; and

(iv) the motion of the target ions along actual trajectories in the tokamak magnetic field (since the Larmor radius for the thermal target ions is much smaller than the typical plasma size, the drift approximation is used, which substantially reduces the computation time).

4. INFLUENCE OF VARIOUS PROCESSES ON THE PROPAGATION OF THE TARGET IONS

Let us consider the results obtained with the above code for a helium plasma with $n_e = 2 \times 10^{19}$ m^{-3} and $T_e = T_i = 3$ keV. Figure 1 illustrates the effect of different factors on the propagation of He^+ ions along the magnetic field line starting from the place of their birth. Curve *a* corresponds to free expansion with account taken of electron-impact ionization only. Curve *b* is obtained with allowance for both electron-impact ionization and charge exchange of He^+ ions with the main plasma ions He^{++}, resulting in the formation of a He^+ halo [3]. Finally, curve *c* takes into account both the above processes and the reflection of charged particles from magnetic mirrors. The latter process results in an even narrower profile of the charge-exchange target and increases the density of ions in the region where they are produced.

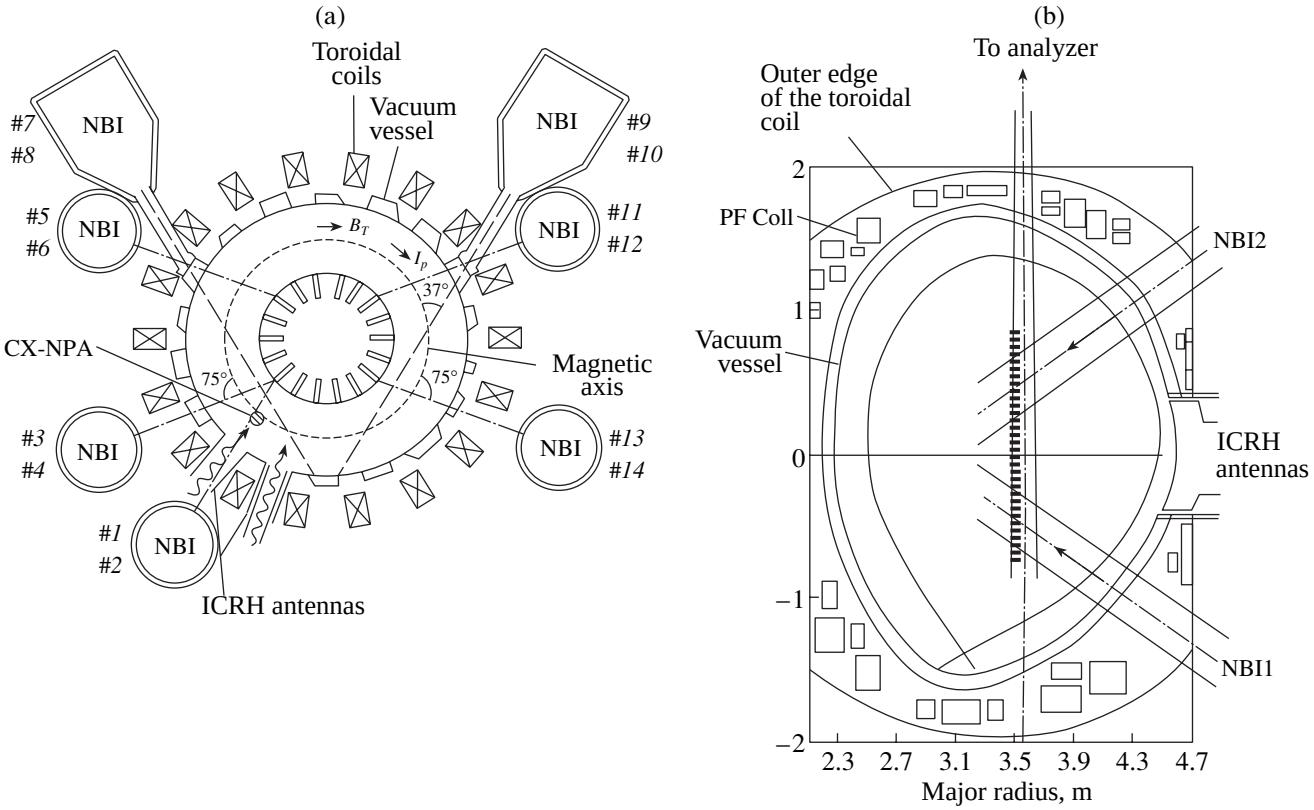

Fig. 2. JT-60U tokamak: (a) top view and (b) vertical cross section.

5. CALCULATION OF A CHARGE-EXCHANGE TARGET FOR JT-60U

The above Monte Carlo code was applied to calculating the target ion density under the conditions of the JT-60U tokamak (Fig. 2a). This is a large tokamak with major and minor plasma radii of 3.5 and 1 m, respectively. In the JT-60U tokamak, experiments on the combined ion-cyclotron-resonance (ICR) and NBI heating are carried out. The NBI system consists of five pairs of perpendicular injectors arranged around the torus. In each pair, one injector is directed upward and the other is directed downward. There are also two tangential injectors oriented in opposite directions along the torus. The diagnostic system also includes the GEMMA-2 analyzer of fast atoms [4] with a vertical line of sight (Fig. 2b). The ICR heating antenna is installed in the same vertical cross section. In this arrangement, the neutral beams do not cross the line of sight of the analyzer.

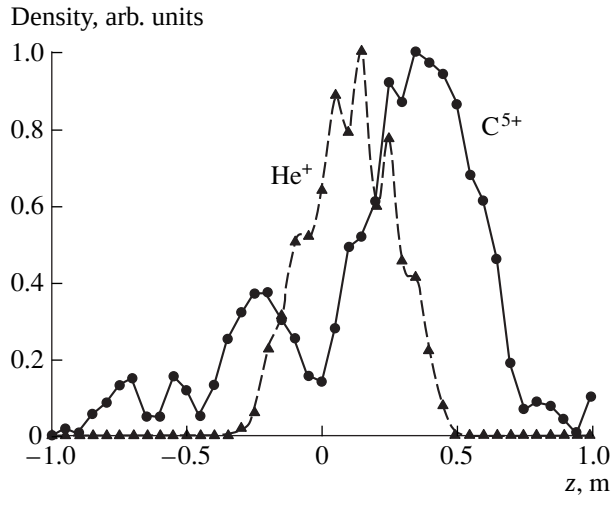

Fig. 3. Density profiles (along the line of sight of the analyzer) of He^+ (dashed line) and C^{5+} (solid line) target ions produced by one hydrogen beam.

To calculate the spatial distribution of the target ions, the following scenario was assumed: We considered the combined ICR heating (in the H minority regime) and NBI heating of a helium plasma. Since the internal surface of the JT-60U vessel is covered by carbon plates, the main plasma impurity is carbon. This scenario suggests that the charge-exchange target for high-energy protons consists of hydrogen-like helium and carbon ions (He^+ and C^{5+}).

The behavior of He^+ and C^{5+} ions in plasma is different. Specifically, the cross section for the electron-impact ionization of C^{5+}, which is the main loss channel, is small. Under the JT-60U conditions, this corre-

sponds to a mean free path of about 20 m. This value is comparable to the plasma length around the torus, which means that C^{5+} ions may revolve several times around the torus before getting ionized by electron impact. As a result, C^{5+} ions arrive at the analyzer cross section from both sides and occupy a major fraction of the plasma column, so that they produce a less localized target. In contrast, the ionization rate of He^+ ions is higher, their mean free path is about 2 m, and only the ions that have followed the shortest path from the beam to the analyzer can appear on the line of sight of the analyzer. The target is more localized in this case. Figure 3 shows the He^+ and C^{5+} targets that are formed with a beam spaced 80° apart in the toroidal direction from the analyzer. The two peaks in the C^{5+} target profile can be attributed to the ions propagating clockwise and counter-clockwise along the torus. In the He^+ profile, the peak corresponding to the longer path is absent.

Such ion behavior results in the neutral beams situated along the torus making comparable contributions to the density of C^{5+} ions at the analyzer site. In contrast, the density of He^+ ions is only determined by the nearest injectors.

6. FEASIBILITY OF LOCAL IDF MEASUREMENTS WITH A STATIONARY ANALYZER

Let us now consider the target profile along the line of sight of the analyzer. Figure 4 shows the distributions of He^+ ions generated by different injecting beams. The profiles are numbered in accordance with the number of the injector with which they are produced. Injectors *2* and *6* both belong to the perpendicular injection system but differ in their positions in the toroidal direction. Injector *2* is situated in the immediate vicinity of the analyzer, and injector *6* is spaced 80° apart from the analyzer. This is also the position of tangential injector *8*. It can be seen that, as they more along the magnetic field lines, the target ions fall into different regions along the line of sight of the analyzer. This fact can be used to perform local measurements of the IDF using a stationary analyzer. The use of He^+ ions is preferable for such measurements because, as was mentioned above, their profile is more localized. Although the injection gives rise to both types of ions, the signals from He^+ and C^{5+} targets can be separated with the help of the code developed and with allowance for the difference in the energy dependences of the cross sections for the charge-exchange of protons with He^+ and C^{5+} ions (Fig. 5).

By the alternate switching-on of the neutral beams, one can separate out the contribution from a particular beam to the analyzer signal and associate it with a certain plasma region. According to Fig. 4, this method allows one to attain a spatial resolution of about 0.5 m. To illustrate, the approximate size of the region occupied by the fast ions in JT-60U during ICR heating is also shown.

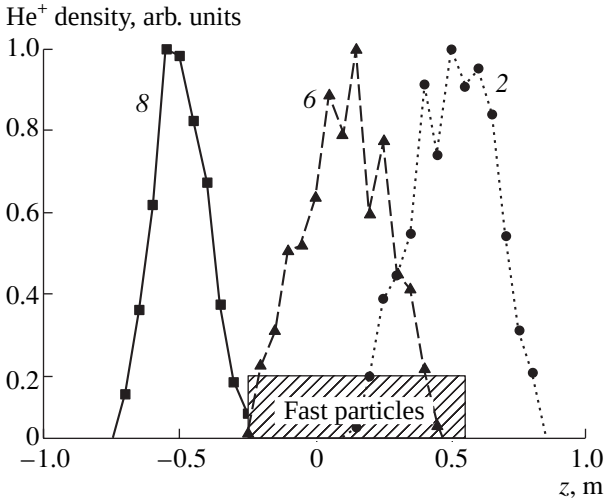

Fig. 4. Density profiles (along the line of sight of the analyzer) of He^+ target ions produced by different beams. The numerals by the curves correspond to the number of the injector producing the target.

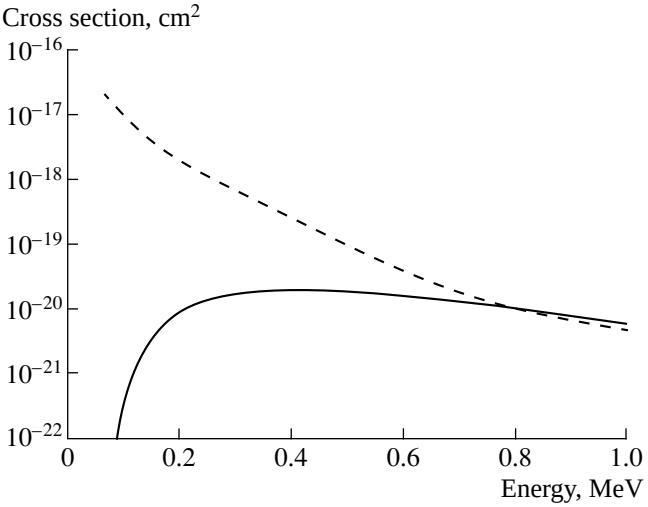

Fig. 5. Cross sections for the charge exchange of protons with He^+ (dashed line) and C^{5+} (solid line) ions.

7. CONCLUSIONS

(i) Under the conditions of modern large tokamaks, the charge-exchange target for fast particles is highly nonuniform. Numerical simulations are required for an adequate interpretation of the data from neutral particle diagnostics in the energy range $E > 0.2$ MeV.

(ii) A Monte Carlo code was developed for calculating the target density with allowance for the actual device configuration, the atomic processes accompany-

ing the production and transport of the target ions, and the target ion motion along real trajectories in the plasma.

(iii) Target profiles were calculated for the JT-60U tokamak. The density profiles of He^+ and C^{5+} ions generated by different beams were found. The feasibility of using these profiles for local IDF measurements with a stationary analyzer has been demonstrated.

REFERENCES

1. M. P. Petrov, V. I. Afanasyev, S. Corti, *et al.*, in *Proceedings of the 19th EPS Conference on Plasma Physics and Controlled Fusion, Innsbruck, 1992*; ECA **16C** (II), 1031 (1992).
2. A. A. Korotkov, A. Gondhalekar, and A. J. Stuart, Nucl. Fusion **37**, 35 (1997).
3. A. V. Khudoleev, V. I. Afanasiev, and M. I. Mironov, in *Proceedings of the 23rd EPS Conference on Plasma Physics and Controlled Fusion, Kiev, 1996*; ECA **20C** (II), 1039 (1996).
4. V. I. Afanasiev, Y. Kusama, M. Nemoto, *et al.*, Plasma Phys. Controlled Fusion **39**, 1509 (1997).

Translated by A. Sidorova

Plasma Physics Reports, Vol. 30, No. 2, 2004, pp. 169–172. Translated from Fizika Plazmy, Vol. 30, No. 2, 2004, pp. 190–194.

PLASMA DIAGNOSTICS

Thomson Scattering System for Direct Observation of Langmuir Cavities

V. S. Burmasov, L. N. Vyacheslavov, I. V. Kandaurov, É. P. Kruglyakov, O. I. Meshkov, and S. S. Popov

Budker Institute of Nuclear Physics, Russian Academy of Sciences, Siberian Division, pr. Akademika Lavrent'eva 11, Novosibirsk, 630090 Russia

Received July 24, 2003

Abstract—An incoherent Thomson scattering system for observing local unsteady cavities that form in a turbulent plasma in the course of Langmuir collapse is described. Using this diagnostics, the density cavities in a laboratory plasma with developed strong Langmuir turbulence were directly observed for the first time and their spatial and temporal characteristics were determined. © *2004 MAIK "Nauka/Interperiodica".*

1. INTRODUCTION

One of the most important effects in a plasma with well-developed Langmuir turbulence ($W/nT_e \gtrsim (kr_D)^2$) is the wave collapse predicted by Zakharov in 1972 [1]. Since that time, this effect has been confirmed in a great number of theoretical studies and numerical simulations (see reviews [2–5]). However, reliable experiments indicating the existence of the Langmuir collapse are still few in number. In this connection, it was even suggested in [6] that Langmuir collapse can be observed only under certain specific conditions, such those as in the well-known work [7], in which the experimental parameters allowed one to obtain a single collapsing cavity whose space and time positions were highly determinate, which is inconsistent with the general picture of developed strong Langmuir turbulence (SLT). Present-day experimental studies of developed SLT [6, 8–10] (i.e., that in the absence of a determinate system behavior, characteristic of [7]) usually deal with its general consequences (the generation of short-wavelength ion acoustic waves, the formation of a non-Maxwellian tail in the electron energy distribution function, the generation of high-power radiation at frequencies close to the plasma frequency and its harmonics, etc.) and yield only indirect evidence for the existence of the Langmuir collapse. To draw more definite conclusions, it is necessary to directly observe occasional collapse events in plasmas. This requires the elaboration of appropriate diagnostics. The creation of such a multichannel system of transverse Thomson laser scattering with high spatial and time resolution was reported for the first time in [11].

In this paper, we present a substantially modified Thomson scattering diagnostics with a higher sensitivity and higher noise immunity. With the help of this diagnostics, small dynamic plasma density cavities were detected and studied in the GOL-M device in a plasma with developed SLT [12]. The experiments were carried out with a dense plasma in a magnetic field ($n_e \sim 10^{15}$ cm^{-3}, $B = 2.5$ T). The level of Langmuir turbulence excited by a high-power relativistic electron beam (REB) ($E \approx 300$–500 keV, $I_b \approx 10$ kA, $\Delta t_b \approx 100$ ns) was $W/nT_e > 0.2$ [10].

2. THOMSON SCATTERING SYSTEM FOR OBSERVING UNSTEADY PLASMA CAVITIES

The diagnostics employs the fundamental-harmonic neodymium laser radiation. A schematic of the laser is shown in Fig. 1. The driving oscillator operates with an optical shutter based on a Pockels cell with a KDP crystal. The duration of the driving oscillator pulse is varied in the range from 10 to 60 ns by varying the cavity length. After passing the preamplifier, the laser beam passes through a 3-mm-diameter coupling hole into a five-pass telescopic amplifier, the active element of

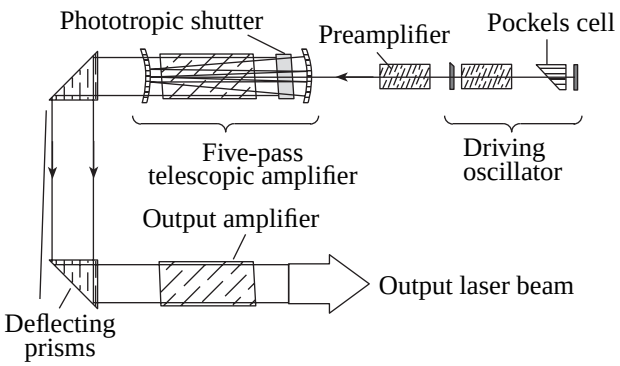

Fig. 1. Schematic of the neodymium laser ($\lambda = 1.06$ μm, $E \sim 20$ J, and $\tau \sim 60$ ns).

1063-780X/04/3002-0169$26.00 © 2004 MAIK "Nauka/Interperiodica"

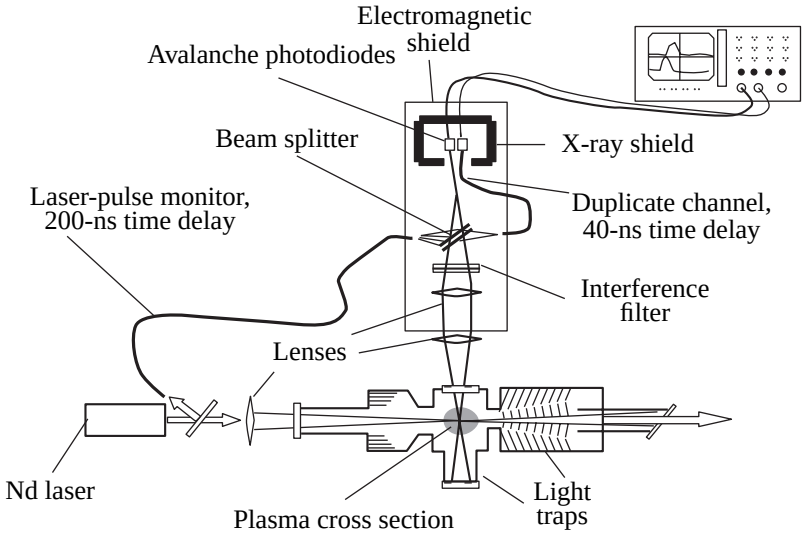

Fig. 2. Thomson scattering system with duplicate optical recording for observing Langmuir cavities. The laser parameters are λ = 1.06 μm, $E \sim 20$ J, and $\tau \sim 60$ ns.

which is a phosphate glass. Self generation in this amplifier is suppressed using a phototropic shutter. After the amplifier, the laser beam is fed with the help of glass prisms to a single-pass final amplifier with an active element made of silicate glass. The amplifier active elements 45 mm in diameter and 640 mm in length are pumped with IFP-20000 flash lamps. The output laser beam has the following parameters: λ = 1.06 μm, $E \approx 20$ J, $\Delta t_{laser} \approx 60$ ns, and a diameter of 40 mm.

Figure 2 shows a scheme of laser radiation input/output and a system for recording scattered radiation. The laser beam passing through the plasma perpendicularly to the magnetic field is focused by a lens (F = 50 cm) onto the chamber axis to a diameter of 0.2 mm and is output through a window positioned at the Brewster angle. The image of a small ($0.2 \times 0.2 \times 1$ mm in size) volume of the focused laser beam is projected at an angle of 90° by a telescopic objective with a focal length of F = 13 cm and a diameter of 5.5 cm onto the ends of light-guiding fibers, and is then fed to C30955E avalanche diodes with a sensitivity of 35 A/W and a time resolution of 2 ns.

To determine the time behavior of the plasma density, the shape of the scattered laser signal was compared to that of an original laser pulse recorded at the same oscilloscope trace. For this purpose, a portion of the laser pulse (a reflex from a deflecting prism) was directed to the recording system with a time delay of 200 ns with respect to the scattered signal. A comparison of the shapes of the recorded signals allowed us to trace the time behavior of the plasma density over the time interval Δt_{laser} with an accuracy of 5–10%. To verify that the change in the shape of the scattered signal was not caused by an electromagnetic pickup induced by the REB in the recording system, the recorded signal was optically duplicated. For this purpose, a portion of the scattered radiation was split off by a 50% mirror and was then directed through a 40-ns optical delay line to an independent recording channel (see Fig. 2). A comparison of the waveforms of the signals in the main and duplicate channels allowed us to reliably recognize the features related to the time behavior of the plasma density against the background of the electromagnetic pickup.

The Thomson scattering system was adjusted in several steps. First, with the help of a helium–neon laser, we roughly positioned all the optical components. Then, using an infrared image intensifier, we accurately adjusted the focusing lens and the objective. Finally, the optical system was adjusted and the recording system was calibrated by Rayleigh scattering in sulfur hexafluoride (SF_6) at a pressure of 0.05 atm.

Stray light at the laser frequency was suppressed by an interference filter with a passband of 40 nm. We note that the recording system with this filter is sensitive to both plasma-density and electron-temperature variations. However, calculations show that the intensity of scattered radiation passed through the filter changes by only 10% as the electron temperature varies from 50 to 250 eV, which covers the range of possible electron temperature variations in our experiments.

Experiments performed with the above Thomson scattering diagnostics showed the presence of dynamic cavities in a plasma with SLT. Figure 3 shows the scattered signals observed in two different shots (Figs 3a, 3c) and the corresponding time behavior of the relative plasma density (Figs. 3b, 3d). It can be seen that the minima in the signals recorded in different channels, as well as the signals themselves, are shifted by 40 ns, which means that they are not related to the electromagnetic pickup. The depth of these minima can attain

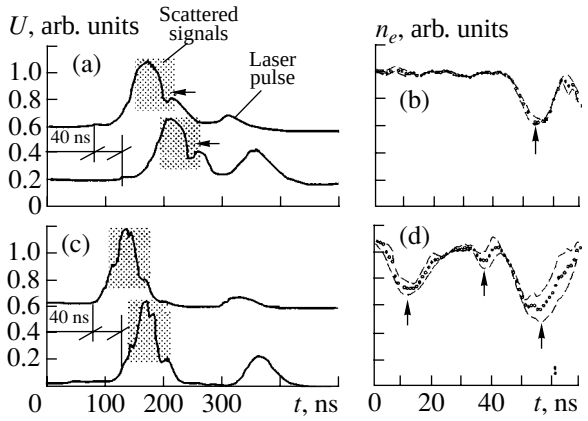

Fig. 3. Observation of plasma-density cavities (indicated by arrows) using duplicate optical recording of the scattered signals with a 40-ns time delay: (a, c) scattered signals and (b, d) the time evolution of the density n_e calculated in the time intervals marked by rectangles. The dotted lines show the average between the density values recorded in two different channels.

30%, and their duration is τ_{cav} = 10–30 ns. Such scattering signals can hardly be explained by temperature variations, since it is difficult to find a plausible explanation for such considerable and fast heating and, especially, cooling. Therefore, the minima in the signals observed in the duplicate-recording scheme are most likely related to plasma density variations.

3. MEASUREMENTS OF THE CAVITY DIMENSIONS

Figure 4a shows a scheme of an experiment on the measurements of the transverse (with respect to the magnetic field) cavity size $l_\perp$. The scattered radiation from four neighboring regions (0.2 × 1 mm in size) along the focused laser beam was directed by a lens to four independent recording channels. The experiments performed by this scheme allowed us to trace the time evolution of the density profile over a distance of 4 mm with a spatial resolution of 1 mm. Typical scattered signals are shown in Fig. 5. Curves in Figs. 5c and 5d demonstrate the most typical situation when the density minimum is observed in only one of the channels. Figures 5a and 5b show time-separated density minima in two adjacent scattering volumes. It follows from these figures that the transverse size of the density cavity is on the order of $l_\perp \lesssim 1$ mm.

In order to demonstrate that the observed cavities were local in character and to estimate their length along the magnetic field, special experiments were carried out by the following scheme. The laser beam was divided into two parts as is shown in Fig. 4b. For this purpose, the middle part of the focusing lens was cut out and the remaining parts were jointed together. Such a composite lens divides the laser beam into two spatially separated focused beams. The distance between

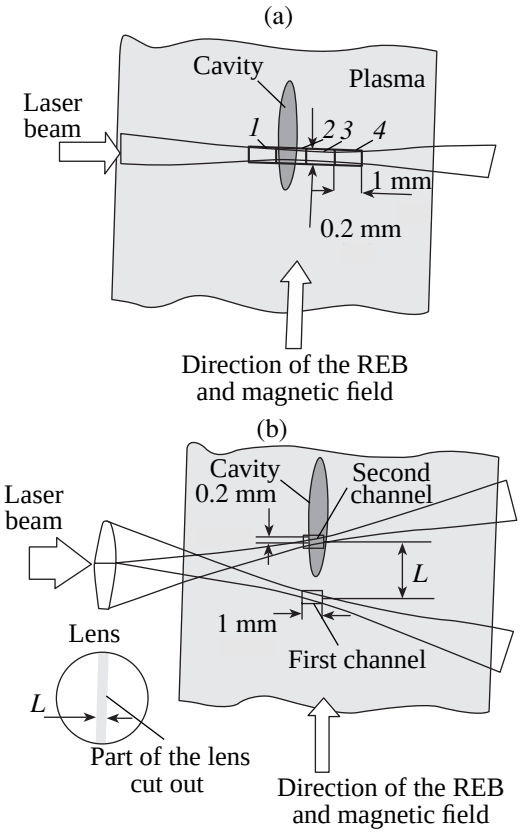

Fig. 4. Scheme of the measurements of the (a) transverse (with respect to the magnetic field) and (b) longitudinal cavity dimensions (*1*, *2*, *3*, and *4* denote the recording channels). The distance between the scattering volumes is L = 3 and 8 mm.

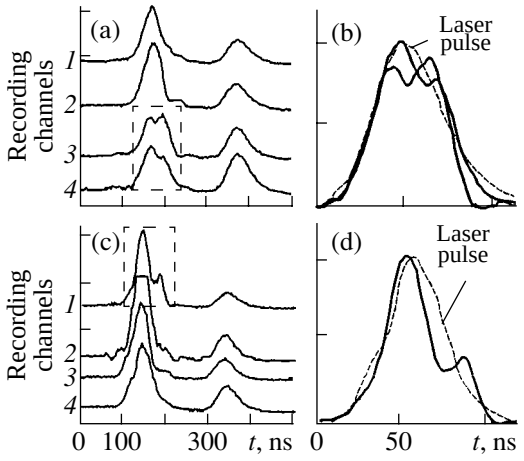

Fig. 5. Determination of the transverse (with respect to the magnetic field) cavity size with the use of a four-channel recording system: (a, c) typical waveforms of the scattered signals and (b, d) signal fragments with density minima brought into coincidence with the laser pulse and marked by frames in plots (a) and (c).

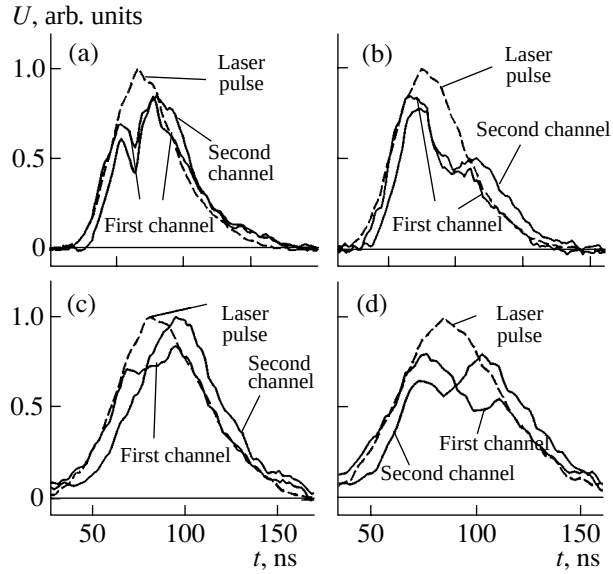

Fig. 6. Determination of the cavity length along the magnetic field with the use of the two-channel recording system at two different distances between the scattering volumes: L = (a, b) 3 and (c, d) 8 mm.

the focuses depends on the width L of the removed part of the lens. In the experiments, we used two such lenses of L = 3 and 8 mm. The beam focuses were adjusted to lie at the same magnetic line by displacing the composite lens and rotating it about the axis of the primary laser beam. The scattering volumes (0.2×1 mm in size) were imaged onto the inputs of two independent recording channels. The finite length of the density cavities was established from the presence (or absence) of simultaneous minima in the waveforms of the scattered signals in the two recording channels. In experiments with L = 3 mm, the density minima observed in both recording channels coincided in time (Figs. 6a, 6b). In experiments with L = 8 mm, either the density minimum was observed in only one of the recording channels (Fig. 6c) or the minima were separated in time (Fig. 6d). From these data, we can infer that the lengths of the Langmuir cavities lie in the range $3 < l_{\|} \lesssim 8$ mm.

4. CONCLUSIONS

An incoherent Thomson scattering system has been created that allows direct observations of local dynamic plasma-density cavities. Necessary conditions for the operation of this system are a sufficient duration and smooth shape of the laser pulse and a high time resolution and high noise immunity of the recording system. With this diagnostics, density cavities arising randomly in time and space have been observed for the first time in a laboratory plasma with developed SLT. The cavities are most likely generated due to Langmuir collapse. The parameters of the observed density cavities are as follows: $\delta n/n$ = 10–40%, τ_{cav} =10–30 ns, $l_{\perp} \le 1$ mm, and $3 < l_{\|} \lesssim 8$ mm.

However, the results obtained give no direct answer to the question of whether the observed density minima are indeed related to Langmuir collapse. This question can be answered, e.g., by examining the evolution of the Langmuir oscillation spectrum in the cavity. Indeed, according to the classical concept [1], Langmuir wave packets in the initial stage of collapse are trapped in a cavity. Then, as the cavity becomes deeper, the amplitude of the trapped Langmuir waves increases and the energy of oscillations is transferred to the short-wavelength region of the spectrum. In a certain stage of this process, dissipation stops the collapse, the Langmuir waves are damped, and the cavity disappears. To perform such observations, it is necessary that the Nd laser scattering system operate simultaneously with a collective CO_2 laser scattering system for studying the time evolution of the spectrum of Langmuir oscillations trapped in the cavity. Work on a diagnostic of this kind is now in progress in the GOL-M device.

ACKNOWLEDGMENTS

This work was supported in part by the Russian Foundation for Basic Research, project nos. 01-02-17492 and 03-02-16352.

REFERENCES

1. V. E. Zakharov, Zh. Éksp. Teor. Fiz. **62**, 1745 (1972) [Sov. Phys. JETP **35**, 908 (1972)].
2. A. G. Litvak, in *Reviews of Plasma Physics*, Ed. by M. A. Leontovich (Atomizdat, Moscow, 1980; Consultants Bureau, New York, 1986), Vol. 10, p. 164.
3. A. S. Kingsep, Itogi Nauki Tekh., Ser. Fiz. Plazmy, No. 4, 48 (1983).
4. V. D. Shapiro and V. I. Shevchenko, in *Basic Plasma Physics*, Ed. by A. A. Galeev and R. N. Sudan (Énergoatomizdat, Moscow, 1984; North-Holland, Amsterdam, 1984), Vol. 2.
5. P. A. Robinson, Rev. Mod. Phys. **69**, 507 (1997).
6. D. M. Karfidov, A. M. Rubenchik, K. F. Sergeĭchev, and I. A. Sychev, Zh. Éksp. Teor. Fiz. **98**, 1592 (1990) [Sov. Phys. JETP **71**, 892 (1990)].
7. A. Y. Wong and P. Y. Cheung, Phys. Rev. Lett. **52**, 1222 (1984).
8. F. Do Prado, D. M. Karfidov, M. Virginia Alves, and R. S. Dallaqua, Phys. Lett. A **248**, 86 (1998).
9. M. P. Brizhinev, S. V. Egorov, B. G. Eremin, and A. V. Kostrov, Pis'ma Zh. Éksp. Teor. Fiz. **43**, 232 (1986) [JETP Lett. **43**, 295 (1986)].
10. L. N. Vyacheslavov, V. S. Burmasov, I. V. Kandaurov, *et al.*, Phys. Plasmas **2**, 2224 (1995).
11. L. N. Vyacheslavov, V. S. Burmasov, I. V. Kandaurov, *et al.*, Magn. Plasma Space Res. **11**, 49 (2002).
12. L. N. Vyacheslavov, V. S. Burmasov, I. V. Kandaurov, *et al.*, Plasma Phys. Controlled Fusion **44**, B279 (2002).

Translated by N.F. Larionova

Plasma Physics Reports, Vol. 30, No. 2, 2004, pp. 173–177. Translated from Fizika Plazmy, Vol. 30, No. 2, 2004, pp. 195–199.

PLASMA DIAGNOSTICS

MHD Diagnostics in the T-11M Tokamak

A. M. Belov and I. N. Makashin

Troitsk Institute for Innovation and Fusion Research, Troitsk, Moscow oblast, 142190 Russia

Received July 24, 2003

Abstract—An MHD diagnostic system for investigating the dynamics of disruption and the preceding phase of the discharge in the T-11M tokamak is described. This system makes it possible to study the structure of magnetic fluctuations in the plasma column. The diagnostic system includes a set of magnetic pick-up loops (Mirnov coils) arranged in several poloidal cross sections of the tokamak, a data acquisition system that provides synchronous recording of Mirnov coil signals, a synchronization system for triggering the data acquisition system during a disruption, and a system for processing and representation of the experimental data on magnetic fluctuations in the plasma column. Examples of how the MHD diagnostic system operates in the T-11M tokamak are presented. © *2004 MAIK "Nauka/Interperiodica".*

1. INTRODUCTION

The problem of eliminating the self-destruction of the magnetic thermal insulation of the plasma in future fusion reactors is of current interest for physical research in existing tokamaks. In this respect, a major disruption is generally considered to be the most dangerous. The problem of investigating the disruption dynamics imposes rigid requirements on the temporal and spatial resolution of a system for measuring MHD perturbations in plasma. In this paper, we describe an MHD diagnostic system created in the period 1994–2000 for the purpose of studying the dynamics of disruption and the preceding phase of the discharge in the T-11M tokamak. The main results obtained with the help of the MHD diagnostic system of the T-11M tokamak were published previously in [1–11].

2. MHD DIAGNOSTIC SYSTEM OF THE T-11M TOKAMAK

The MHD diagnostic system of the T-11M is intended for studying both fast MHD plasma perturbations (such as major disruptions) with a characteristic time on the order of several hundred microseconds and slower processes (such as the development of locked modes) with a characteristic time of up to several tens of milliseconds. This diagnostics should also provide information on the structure of magnetic perturbations in plasma and MHD activity during the discharge. Hence, this diagnostic should satisfy the following requirements:

(i) A great number of magnetic pick-up loops (Mirnov coils) should be arranged in several poloidal cross sections of the tokamak in order to provide space-resolved measurements of magnetic fluctuations in plasma.

(ii) The Mirnov coils should have high temporal resolution of in order to provide a detailed study of the disruption process.

(iii) A fast multichannel data acquisition system (DAS) with the synchronous recording of Mirnov coil signals should be capable of operating in both an ordinary continuous mode with recording signals within prescribed time intervals during the discharge and a continuous mode with the storage of prehistory information for recording processes occurring at time intervals that are not known in advance (disruptions).

(iv) There should be a special synchronization system for triggering the DAS when recording a disruption.

The MHD measurements are performed with several Mirnov coil arrays (MCAs) installed in different poloidal cross sections. The coils in each array are arranged uniformly along the poloidal circumference of the torus. To protect the coils and provide their faster operation, the coils are placed in metal tubes that are mounted inside the tokamak vessel along the poloidal circumference. The tubes are open to the atmosphere. The upper operating frequency of the coils is determined by the time constant of the tubes, $\tau_t \approx 2$ μs. An RC circuit ($\tau_{RC} \approx 88.4$ μs) was used as an output element of the coil. This was motivated not only by the requirement that the output signal be proportional to the field, but also the necessity of providing the maximum temporal resolution of the signal in the dynamic range of the analog-to-digital converter both before and during a disruption, when the amplitude and frequency of the signal increase manyfold. The field fluctuation magnitude B_p was reconstructed by numerically integrating the coil signals with allowance for the time constants of both the RC circuits and the protecting tubes surrounding the coils. Taking into account the factor λ characterizing the phase asymmetry of MHD perturbations over the poloidal angle θ, we can determine the

1063-780X/04/3002-0173$26.00 © 2004 MAIK "Nauka/Interperiodica"

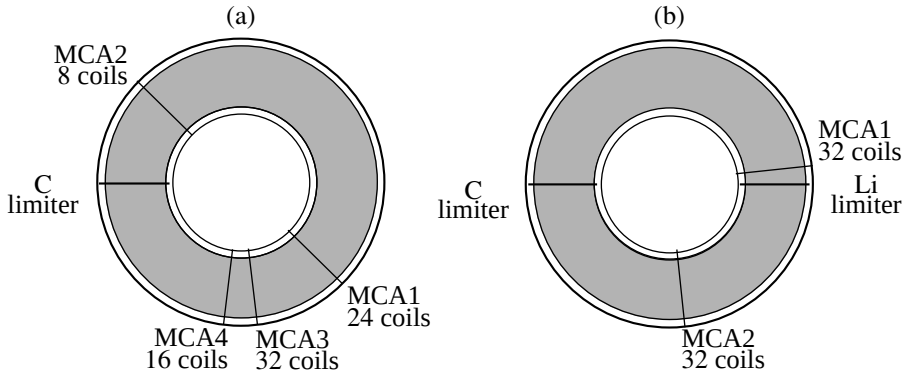

Fig. 1. Arrangement of the MCAs in the T-11M tokamak (a) before and (b) after its modification.

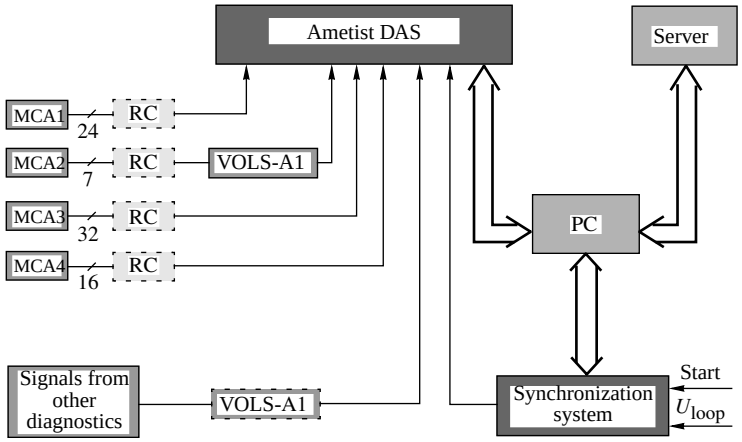

Fig. 2. Block diagram of the recording of Mirnov coil signals in T-11M.

amplitude and phase of the mth poloidal harmonic according to the so-called Merezhkin transformation: $\theta^* = \theta + \lambda\sin\theta$, where $\theta = 0$ on the high-field side of the torus and $\lambda = \dfrac{a}{R_p}\left(\beta_J + \dfrac{l_i}{2} + 1\right)$ [12]. Using the data from magnetic measurements in several poloidal cross sections, we can compare the difference between the phases of helical perturbations $B_\theta(\theta, \varphi) = B_\theta\cos(m\theta - n\varphi)$ with the same poloidal mode number m determined from the harmonic analysis of the coil signals. If the helical symmetry of perturbations is conserved, then, from the found phase difference, we determine the toroidal mode number n and, finally, the location of these perturbations over $q(r)$ ($q(r_s) = m/n$, assuming that $\nabla p = 0$ near the rational surface, where p is the plasma pressure). Figure 1 shows the arrangement of the Mirnov coils in the two different versions of T-11M.

Figure 2 shows the block diagram of a system for recording the signals from the Mirnov coils in T-11M (before the modification of the device). The block diagram that is presently used is almost the same except for the number of the arrays and coils. Signals from other diagnostics are recorded simultaneously with the coil signals, which provides additional information for the subsequent analysis. The galvanic decoupling of the detectors from the recording system is ensured by using an analog fiber-optical transmission line VOLS-A1. The Ametist DAS is built to the CAMAC standard on the basis of FK 4225 analog-to-digital converters and is controlled by a PC. The main parameters of the DAS are as follows: the number of synchronous recording channels is 86, the sampling rate is as high as 1 MHz, and the buffer memory per channel is 4 k. The system is able of operating in both an ordinary continuous mode and a continuous mode with prehistory.

The DAS is synchronized with the help of a synchronization unit that ensures the timing of the system with respect to the discharge. The synchronization unit is built to the CAMAC standard and is controlled by a PC. Recording within a prescribed time interval does not present problems and proceeds in a standard way

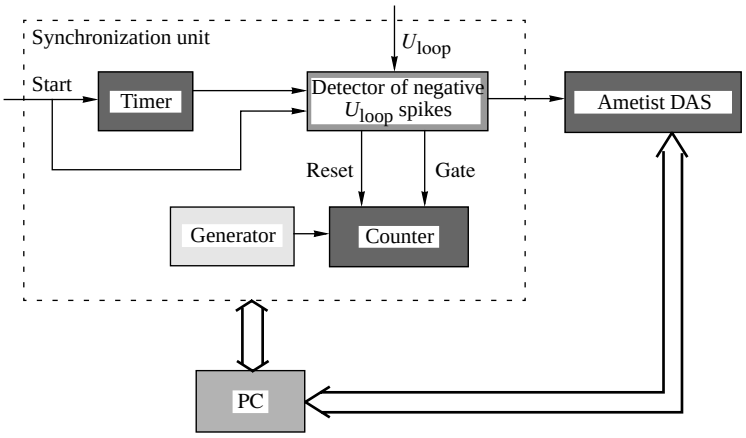

Fig. 3. Block diagram of the synchronization unit of the Ametist DAS.

(the DAS operates in the continuous mode and is triggered by a timer signal). The main problem is to synchronize the DAS when recording a disruption because the disruption time is not known in advance. To solve this problem, the DAS operates in the continuous mode with prehistory. As a synchronizing pulse, we use a negative spike in the loop-voltage U_{loop}, which is generated at the instant of the disruption onset and, therefore, is a convenient signal for triggering the recording system. Consequently, the problem reduces to the measurement of the time delay of the negative U_{loop} spike with respect to the beginning of the discharge. Figure 3 shows the block diagram of the synchronization unit of the Ametist DAS. The synchronization unit operates as follows. A synchronizing pulse corresponding to the start of a discharge (start signal) is simultaneously fed to the synchronization unit, a timer programmed with a PC, and a detector of negative U_{loop} spikes. In response to the start signal, the detector of negative U_{loop} spikes generates two signals that are fed to a counter: a reset signal, which zeroes the counter, and a gate signal, during which the counter counts pulses fed from a generator. The generator operates in a continuous mode with a frequency of 1 MHz. Upon receiving the negative U_{loop} spike, the gate signal ends, the counting stops, and a synchronizing pulse for starting the DAS is generated. After the data recording is finished, the content of the counter is read by the PC and the DAS start time is determined. In this way, the MHD diagnostic system can automatically record Mirnov coil signals in discharges with disruptions over the entire experimental session, skipping disruption-free discharges.

The operation of the Ametist DAS and the synchronization system are controlled by a PC. The data recording and primary processing are performed at the same computer. After each tokamak shot, the data are transmitted to a server. The information gathered in one shot totals ~0.7 MB.

The MHD diagnostic system includes a program package for the processing and representation of the recorded MHD perturbations. This program package provides the following operations:

(i) visual representation of the original and processed data,

(ii) output of the original and processed Mirnov coil signals from several arrays in polar coordinates with the use of animation,

(iii) summation/subtraction of the coil signals,

(iv) generation of the horizontal and vertical shift signals u_h and u_v and the signal of the plasma current increment ΔI,

(v) correction of the coil signals for the plasma shifts and current increment,

(vi) mathematical integration of the coil signals with/without allowance for τ_t and τ_{RC},

(vii) mathematical filtering with a time constant τ,

(viii) correlation analysis,

(ix) calculation of the amplitude and phase characteristics of the mth harmonic with/without allowance for the phase symmetry of the magnetic field perturbation over the poloidal angle θ,

(x) modeling of the coil signals in the absence of some mth harmonics,

(xi) calculation of the toroidal mode numbers n, and

(xii) conversion of the acquired data into text files.

3. EXAMPLES OF HOW THE MHD DIAGNOSTICS OPERATES IN THE T-11M TOKAMAK

Figure 4 shows examples of the data representation by the system for processing the results of MHD measurements. Figure 4a shows the signals from the first MCA after mathematical filtering. No RC circuit was used. Figure 4b demonstrates a frame obtained using

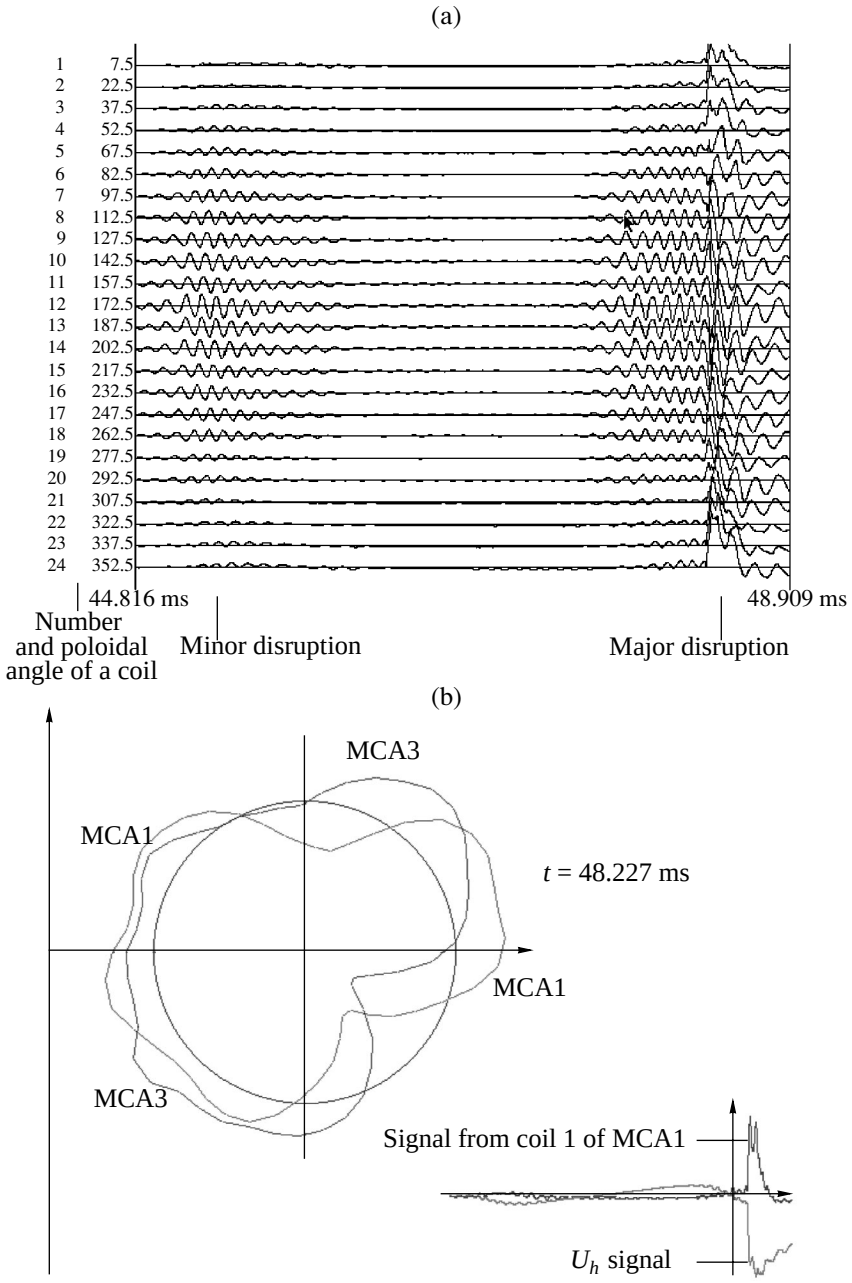

Fig. 4. Example of the data representation by the system for processing and the results of MHD measurements: (a) the time evolution of the signals from the first MCA after mathematical filtering (τ_{filter} = 100 μs, shot no. 10 053) and (b) a frame obtained using signals from the first and third MCAs for the same shot.

the signals from the first and third MCAs for the same shot.

Figure 5 [9] illustrates the results of processing the signals from the first and third MCAs with a sampling time of 1 μs. The figure represents a minor disruption followed by a locked mode that ends with a major disruption (only the beginning of the major disruption is shown in the figure). It can be seen that, after the minor disruption, the locked mode with a dominant $m = 2$ perturbation develops and exists for nearly 0.5 ms. The figure also shows the result of the harmonic analysis of magnetic perturbations, specifically, the time evolution of the amplitudes of the $m = 2$ helical harmonics in two different poloidal cross sections. The plot of the time evolution of the amplitudes of the $m = 2$ helical harmonics demonstrates a fair correlation between them in two different poloidal cross sections. The mathematical treatment of signals from the first and third MCAs was

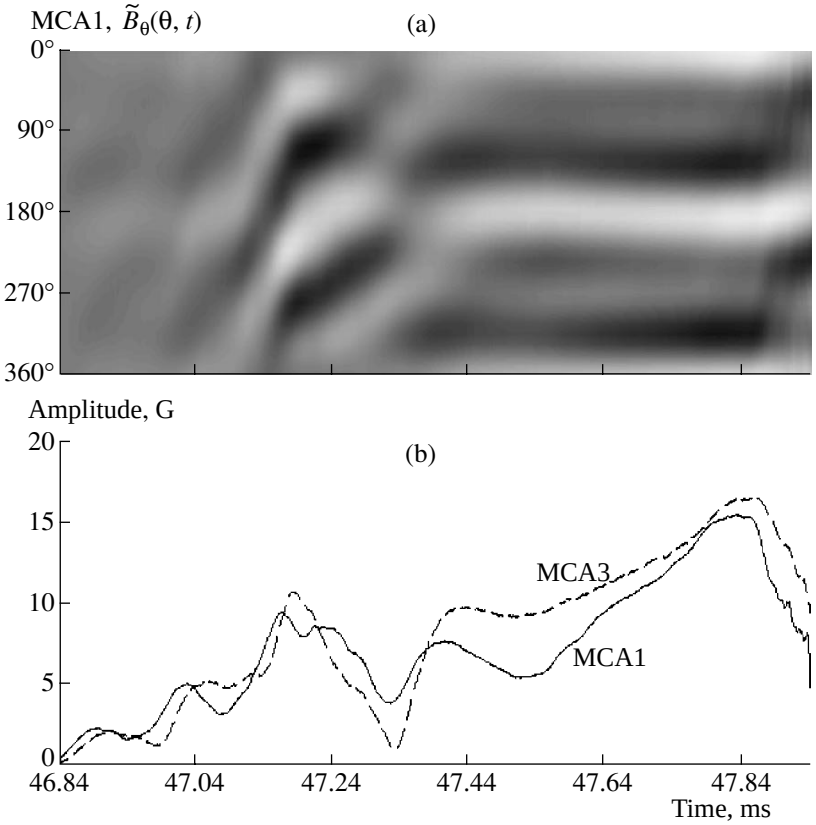

Fig. 5. Minor disruption and the subsequent development of a locked mode with a dominant $m = 2$ perturbation, ending in a major disruption (shot no. 12460): (a) the visualization of MHD perturbations (0° and 360° correspond to the high-field side, while 180° corresponds to the low-field side of the torus) and (b) the time evolution of the amplitudes of the $m = 2$ helical harmonics obtained for two different poloidal cross sections of the tokamak ($\lambda = 0.3$) [9].

performed with allowance for the phase asymmetry of MHD perturbations over the poloidal angle θ ($\lambda = 0.3$).

REFERENCES

1. É. A. Azizov, A. M. Belov, O. I. Buzhinskiĭ, *et al.*, Fiz. Plazmy **20**, 1060 (1994) [Plasma Phys. Rep. **20**, 950 (1994)].
2. I. B. Semenov, A. M. Belov, I. N. Makashin, *et al.*, in *Proceedings of the 22nd EPS Conference on Plasma Physics and Controlled Fusion, Bournemouth, 1995*; ECA **19C** (1), 421 (1995).
3. S. V. Mirnov, A. M. Belov, I. N. Makashin, *et al.*, in *Proceedings of the 16th International Conference on Fusion Energy, Montreal, 1996* (IAEA, Vienna, 1997), Vol. 1, p. 763.
4. A. M. Belov, S. V. Mirnov, I. B. Semenov, *et al.*, in *Proceedings of the 24th EPS Conference on Plasma Physics and Controlled Fusion, Berchtesgaden, 1997*; ECA **21A** (1), 485 (1997).
5. A. M. Belov, S. V. Mirnov, I. B. Semenov, *et al.*, in *Proceedings of the 25th EPS Conference on Plasma Physics and Controlled Fusion, Praha, 1998*; ECA **22C**, 611 (1998).
6. A. G. Alekseyev, A. M. Belov, E. A. Azizov, *et al.*, in *Proceedings of the 26th EPS Conference on Plasma Physics and Controlled Fusion, Maastricht, 1999*; ECA **23J**, 833 (1999).
7. A. G. Belov, S. V. Mirnov, A. G. Alekseyev, and I. N. Makashin, in *Proceedings of the 27th EPS Conference on Plasma Physics and Controlled Fusion, Budapest, 2000*; ECA **24B**, 596 (2000).
8. S. V. Mirnov, A. M. Belov, D. Yu. Prokhorov, *et al.*, in *Proceedings of the 18th IAEA Fusion Energy Conference, Sorrento, 2000*, Paper IAEA-CN-77/EXP3/08.
9. S. V. Mirnov, A. M. Belov, and D. Yu. Prokhorov, Preprint No. 0081A (Troitsk Institute for Innovation and Fusion Research, Troitsk, 2001).
10. A. M. Belov, V. B. Lazarev, A. G. Alekseyev, *et al.*, in *Proceedings of the 28th EPS Conference on Plasma Physics and Controlled Fusion, Funchal, 2001*; ECA **25A**, 2125 (2001).
11. A. M. Belov, S. V. Mirnov, A. G. Alekseev, and V. B. Lazarev, in *Collection of Articles of the TRINITI Department of Physics of Tokamak Reactors* (TRINITI, Troistk, 2002), No. 2.
12. V. G. Merezhkin, Fiz. Plazmy **4**, 275 (1978) [Sov. J. Plasma Phys. **4**, 152 (1978)].

Translated by N.F. Larionova

Plasma Physics Reports, Vol. 30, No. 2, 2004, pp. 178–182. Translated from Fizika Plazmy, Vol. 30, No. 2, 2004, pp. 200–204.

PLASMA DIAGNOSTICS

Monitoring of the Plasma Isotope Composition by Charge-Exchange Neutral Fluxes in a Rippled Toroidal Magnetic Field

A. V. Khudoleev*, H.-U. Farhbach, and ASDEX-Upgrade team****

** Ioffe Physicotechnical Institute, Russian Academy of Sciences, Politekhnicheskaya ul. 26, St. Petersburg, 194021 Russia*

*** Max-Planck Institut für Plasmaphysik, IPP–Euratom Association, D-85748 Garching, Germany*

Received July 24, 2003

Abstract—To determine the hydrogen isotope ratio in plasma from charge-exchange neutral fluxes, certain assumptions are traditionally adopted, the most restrictive of which concerns the form of the ion distribution function, which is usually assumed to be Maxwellian. For large tokamaks, however, additional analysis is required in order to determine the energy range in which distortions of the distribution function will not lead to errors in isotope ratio measurements. The possible influence of drift motion on the ion distribution function is considered. Experimental results obtained in the ASDEX-Upgrade tokamak are presented. The role this mechanism plays during the transition to the H-mode in the auxiliary heating regime is compared to that in the ohmic heating regime. © *2004 MAIK "Nauka/Interperiodica".*

1. INTRODUCTION

The analysis of charge-exchange neutral fluxes is commonly used to measure the isotope composition of the hydrogen component in a high-temperature plasma. It was proposed in [1] that this method be used to monitor the deuterium and tritium contents in the ITER tokamak reactor. To relate the ion isotope ratio in the plasma to the corresponding charge-exchange neutral fluxes, it is necessary to know such plasma parameters as the ion temperature profile and the profiles of the electron and impurity densities. Another parameter that must be known is the local ion distribution function (IDF), which is usually assumed to be Maxwellian [1, 2]. Then, at the same temperatures of different isotopes, the ion density ratio is proportional to the corresponding flux ratio, corrected to the plasma opacity. In this model, an increase in the energy range of detected particles makes it possible to obtain information about the isotope composition in the interior of the plasma column.

At present, however, the main operating scenario of ITER is considered to be one with auxiliary neutral-beam-injection (NBI) and ion-cyclotron-resonance (ICR) heating [3]. It is well known that, in this case, the high-energy part of the IDF is distorted and can no longer be used for conventional measurements of the isotope composition. The experimental data from existing tokamaks show that the upper limit of the energy range in which the IDF can be considered Maxwellian in such an auxiliary heating regime can be estimated at 50–100 keV.

2. IDF BEHAVIOR DURING A TRANSITION TO THE H-MODE

Another important factor affecting the formation of the IDF is the presence of ripples of the toroidal magnetic field. Since charge-exchange diagnostics are usually situated near the minimum of the magnetic field, it is necessary to take into account the effects associated with the drift of locally trapped particles. Kinetic convective ion transport can lead to either the enrichment or depletion of the IDF with high-energy particles. The ion behavior depends of the ion mass and energy, the topology of the magnetic field, and the profile and magnitude of the radial electric field in the plasma. Since the basic ITER operating mode is assumed to be an ELMy H-mode [3], the influence of the electric field can be significant. If the sign of the electric field is such that the drift in the crossed electric and magnetic field is directed oppositely to the gradient drift, then for ions with a certain energy, these drifts cancel each other. During the H-mode quiescent phase, locally trapped particles are confined in plasma due to the generated radial electric field. After the onset of instability, the electric field disappears and the particles leave the plasma with drift velocities. Phenomenologically, this manifests itself in the modulation of charge-exchange neutral fluxes. Such an effect was observed in the ASDEX-Upgrade tokamak during NBI [4]. The IDF behavior during the L–H transition is shown in Fig. 1. It can be seen that, as the electric field increases, the fast particles are accumulated until the first ELM appears. In this case, over a time of 50–100 μs, the accumulated particles escape onto the wall, and the IDF relaxes to that in the L-mode. The influence of convective trans-

1063-780X/04/3002-0178$26.00 © 2004 MAIK "Nauka/Interperiodica"

port on the dynamics of fast particles in the presence of a radial electric field was theoretically studied in [5], where the source of ions was assumed to be the ionization of the heating-beam neutrals.

Later experiments carried out in the ASDEX-Upgrade tokamak showed that similar effects take place when the source of fast particles is the tail of the Maxwellian distribution. Figure 2 shows the time dependences of the parameters of a discharge in which, after the heating beam is switched off, the H-mode survives for quite a long time and the beam ions have time to be thermalized. The behavior of the IDF during the heating phase and after the beam is switched off is shown in Fig. 3. It can be seen that, in both cases, the flux modulation at high energies due the onset of instability is observed. This allows us to conclude that the influence of the electric field in the presence of convective transport does not depend on the type of the fast-ion source.

Since, in the present ITER design, the magnetic field ripple at the periphery is substantial and reaches about 0.5% at the separatrix, it is necessary to examine the possible influence of kinetic convective transport on the formation of a local IDF.

3. A MODEL OF THE IDF FORMATION IN THE PRESENCE OF MAGNETIC FIELD RIPPLE

Let us consider a qualitative model that takes into account the IDF distortion caused by diamagnetic drift [7]. The model uses a number of simplifying assumptions; in particular, it ignores the influence of the electric field on the ion drift trajectories. Nevertheless, this model allows one to determine the energy range in which kinetic convective transport significantly affects IDF formation.

The characteristic energy at which the drift length of locally trapped ions becomes comparable to the minor radius of the plasma column and the ions leave the plasma can be estimated as

$$E_{dr} \approx 2\left(aBR_0\left\langle\frac{n}{10\Delta}\right\rangle 1/\sqrt{A_i}\right)^{2/5}, \qquad (1)$$

where a is the minor radius, R_0 is the major radius, B is the magnetic field, n is the plasma density, A_i is the atomic weight of an ion, and Δ is the ripple depth (here, energy is in keV, dimensions are in m, the magnetic field is in T, and the density is in 10^{19} m^{-3}). For typical ITER parameters, this energy amounts to nearly 40–50 keV for deuterium and tritium.

The kinetic equation for the IDF of trapped ions under the assumption of their adiabatic trapping in magnetic field ripple has the form [7]

$$\frac{\partial^2 f}{\partial\xi^2} + \frac{\partial f}{\partial\xi} - \lambda H(E - E_{dr})\xi^{3/2} f = 0, \qquad (2)$$

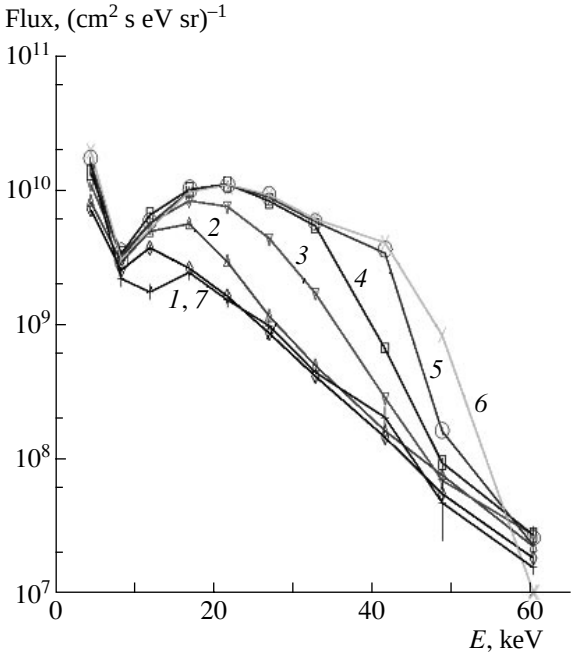

Fig. 1. Energy spectra of charge-exchange neutral fluxes in the ASDEX-Upgrade tokamak in deuterium discharge no. 8595 in successive time intervals during the L–H transition: t = (*1*) 1.6800–1.6900, (*2*) 1.6900–1.7000, (*3*) 1.7000–1.7100, (*4*) 1.7100–1.7200, (*5*) 1.7300–1.7400, (*6*) 1.7650–1.7720, and (*7*) 1.7725–1.7735 s. Spectrum *1* is measured in the L-mode, spectra *2–6* correspond to the H-mode quiescent phase, and spectrum *7* is measured in the H-mode during the onset of an ELM.

where $H(E - E_{dr})$ is the Heaviside function and the other parameters are defined by the formulas

$$\xi = \frac{E}{T_i}; \quad \lambda = \sqrt{2}\frac{\nu_{ad}(E)}{\nu_{T_i}}\frac{T_i}{E} \approx \left(\frac{T_i}{E_{ad}}\right)^{3/2}\frac{1}{30\sqrt{\varepsilon\Delta}}, \qquad (3)$$
$$\varepsilon = r/R_0.$$

The solution to Eq. (2) can be obtained in the Wentzel–Kramers–Brillouin approximation. For the IDF normalized to its value at zero energy, we have

$$f(E) = \exp\left(-\frac{E}{T_i}\right) - \frac{Q_0^* - 1}{Q_0^* + 1}\exp\left(-\frac{E_{ad}}{T_i}\right) \quad E \le E_{ad}$$
$$f(E) = \left(\frac{Q_0^*}{Q^*}\right)^{1/2}\frac{2}{1 + Q_0^*} \qquad (4)$$
$$\times \exp\left[-\frac{1}{2}\left(\frac{E + E_{ad}}{T_i} + \int_{E_{ad}}^{E} Q^*\frac{dE}{T_i}\right)\right] \quad E \ge E_{ad}$$

$$Q^*(E) = \left[1 + 4\lambda\left(\frac{E}{T_i}\right)^{3/2}\right]^{1/2} \approx \left[1 + \frac{0.1}{\sqrt{\varepsilon\Delta}}\left(\frac{E}{E_{ad}}\right)^{3/2}\right]^{1/2},$$

where E_{ad} is the energy corresponding to the adiabatic trapping of ions in magnetic field ripple and $Q_0^* =$

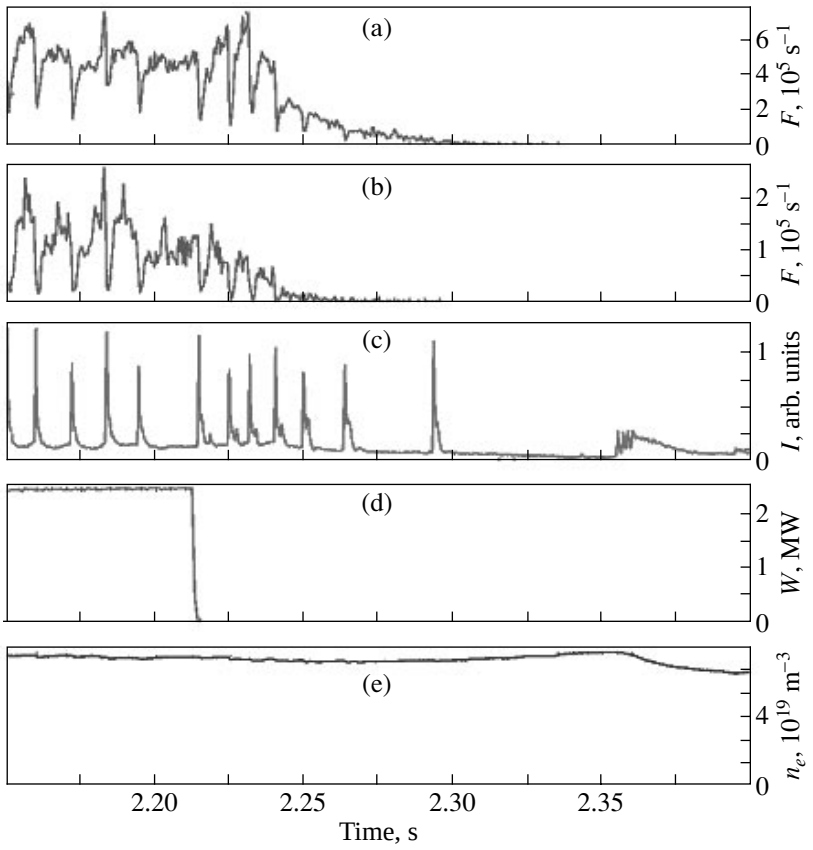

Fig. 2. Time behavior of the signals in the H-mode in the ASDEX-Upgrade tokamak (shot no. 10891): the counting rates F of charge-exchange deuterium neutrals for energies of E = (a) 4.0 and (b) 12.6 keV, (c) the hydrogen line intensity I, (d) the NBI power W, and (e) the plasma electron density n_e.

$Q^*(E_{ad})$. It can be seen that the integral term in the exponent results in an energy dependence of the IDF at $E \geq E_{ad}$ that differs substantially from the Maxwellian and is a function of the ion atomic weight; i.e., it is different for different hydrogen isotopes.

4. RESULTS OF THE IDF MEASUREMENTS IN THE OHMIC HEATING REGIME

Let us compare the results predicted by the above model with the experimental results obtained in the ASDEX-Upgrade tokamak, in which the IDFs of hydrogen and deuterium ions were found to be different in the ohmic heating regime. The ASDEX-Upgrade experiments showed that, in an ohmically heated plasma with $T_i \sim 1$ keV, the ratio between the hydrogen and deuterium atomic fluxes at energies above 4–5 keV depends on the energy and differs substantially from the expected value. The corresponding deuterium and hydrogen fluxes are shown in Fig. 4. The figure also shows the isotope ratio and the effective isotope temperatures $T_{\text{eff}}(E) = -(\partial \ln f/\partial E)^{-1}$ deduced from measured energy spectra. At low energies, the values of $T_{\text{eff}}(E)$ for deuterium and hydrogen almost coincide and increase with increasing energy E (the higher energy particles arrive from the deeper plasma regions with higher ion temperatures). The isotope ratio measured from the charge-exchange fluxes in this energy range does not depend on the energy, which can be interpreted as the constancy of this parameter along the analyzer's line of sight. At energies above 4 keV, the deuterium and hydrogen temperatures $T_{\text{eff}}(E)$ depend only slightly on E (i.e., they correspond to the maximum ion temperatures at the analyzer's line of sight), but their values differ by 20–25%. The same results were obtained at different plasma isotope compositions (the hydrogen concentration in these experiments was varied from 10 to 90%).

A standard analysis of the measured fluxes shows that the isotope ratio depends on the energy, which is clearly not the case. Since the diagnostic complex of the ASDEX-Upgrade allows one to scan the plasma column, the isotope ratio was measured at different spatial points. The results of these measurements showed that the hydrogen-to-deuterium concentration ratio in the plasma did not depend on the radius. Numerical simulations of charge-exchange fluxes under the assumption of a Maxwellian IDF confirmed that the result obtained cannot be consistently explained by variations in the plasma density, ion temperature, or the

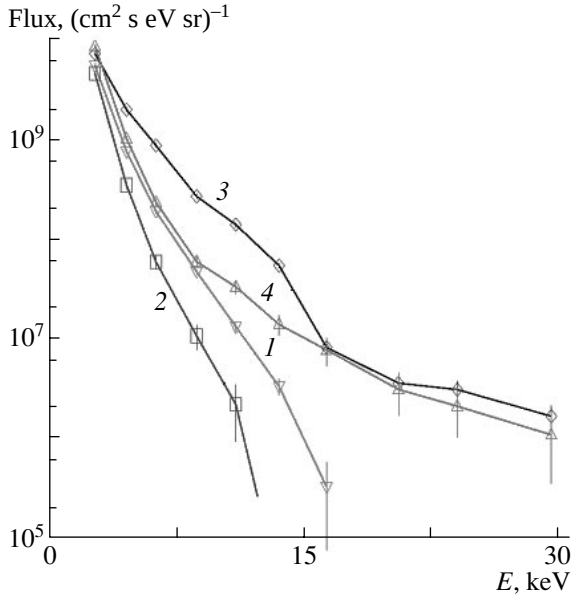

Fig. 3. Influence of ELMs on the energy spectra of charge-exchange neutrals (*1*, *2*) in the Ohmic heating phase and (*3*, *4*) during NBI in the ASDEX-Upgrade tokamak (shot no. 10891) before (curves *1*, *3*) and during (curves *2*, *4*) an ELM.

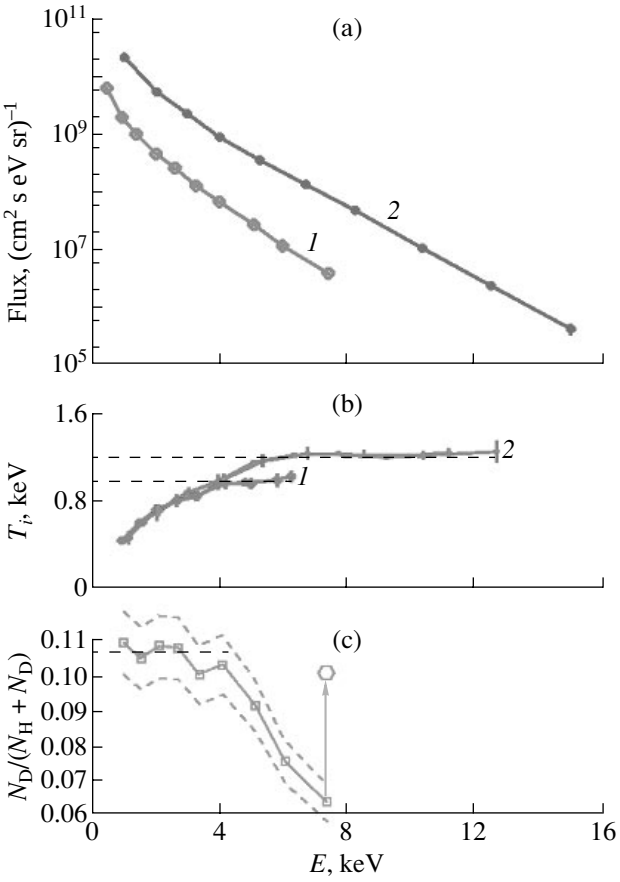

Fig. 4. Ohmic discharge no. 12619 in hydrogen with a deuterium admixture: (a) energy spectra of charge-exchange neutral fluxes of (*1*) deuterium and (*2*) hydrogen, (b) their effective temperatures, and (c) the relative deuterium concentration (the dashed lines indicate the confidence interval of errors). In plot (c), the arrow shows the relative density corrected for the difference in the effective temperatures of deuterium (1.0 keV) and hydrogen (1.2 keV).

radial profile of the isotope ratio [6]. Hence, the analysis of the available experimental data allows us to conclude that the assumption concerning the radial dependence of the isotope ratio that was made in [8] to explain a similar behavior of charge-exchange fluxes in the JET tokamak is not valid. Analyzing the ion energy balance equations, it can also be shown that, in view of the high ion–ion collision frequency, the radial dependence of the isotope ratio cannot be a mere consequence of the difference in the hydrogen and deuterium temperatures.

Let us consider the experimental data from the standpoint of the possible distortion of the IDF due to convective transport. We calculated the local IDF with allowance for convective transport effects in the ASDEX-Upgrade tokamak for the following discharge parameters: B_{tor} = 2.5 T, T_i = 1 keV, and $N_e = 1.4 \times 10^{19}$ m^{-3}. The dependence of the ripple depth on the normalized radius ρ was given by the approximate formula $\delta = \Delta_0 \exp(\rho/\omega)$, where $\Delta_0 = 2.4 \times 10^{-4}$ and $\omega = 0.32$. The radial profile of the neutral hydrogen density in the plasma was then calculated in the standard way. To model the flux measured by the analyzer, the drift IDF was integrated along the analyzer's line of sight with account taken of the charge exchange with ions and the ionization of escaping atoms. Figure 5 shows the calculated values of $T_{eff}(E)$ for deuterium and hydrogen and the ratio between their fluxes as a function of E. The stepwise behavior of the flux ratio is related to the presence of the Heaviside function in the kinetic equation. Taking into account the above simplifying assump-

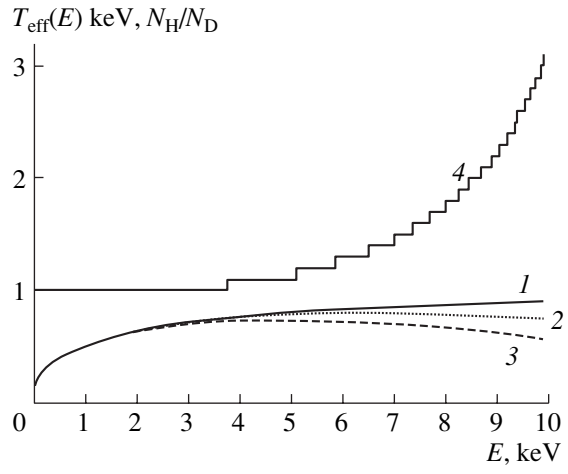

Fig. 5. Calculated energy dependences of the effective ion temperature T_{eff} for a Maxwellian distribution (curve *1*) and for hydrogen and deuterium with account of kinetic convective transport (curves *2* and *3*, respectively) and the hydrogen-to-deuterium isotope ratio (curve *4*).

tions, we can conclude that the drift model satisfactorily describes the experimental results.

For the ITER tokamak with $T_i \sim 30$ keV and, accordingly, higher energies of the detected particles, the effects under discussion may be important for the interpretation of the experimental data. To analyze the influence of the drift motion and electric field on the IDF, it is necessary to carry out calculations similar to those performed in [5] and based on the exact solution of the kinetic convective transport equation with account taken of all the sources of high-energy ions.

5. CONCLUSIONS

The interpretation of the results from the charge-exchange diagnostics of hydrogen ions in large modern tokamaks should be based on an analysis of the specific operating regime of particular devices.

The observed difference between the effective hydrogen and deuterium temperatures that leads to the energy dependence of the isotope ratio is attributable to kinetic effects.

The presence of the electric field and toroidal magnetic field ripple is of crucial importance for the interpretation of the experimental data.

The extrapolation of the results from charge-exchange diagnostics to large devices such as ITER requires the detailed analysis of the IDF and accurate numerical simulations.

REFERENCES

1. A. V. Khudoleev, V. I. Afanas'ev, and F. V. Chernyshev, Fiz. Plazmy **24**, 185 (1998) [Plasma Phys. Rep. **24**, 161 (1998)].
2. A. I. Kislyakov, M. P. Petrov, and E. V. Suvorkin, Plasma Phys. Controlled Fusion **43**, 1775 (2001).
3. *ITER Physics Basis*, Nucl. Fusion (Special Issue) **39**, 2137 (1999).
4. W. Herrmann, Tech. Rep. No. IPP 1/315 (Max-Planck Institut für Plasmaphysik, Garching, 1998).
5. J. A. Heikkinen, W. Herrmann, and T. K. Kurki-Sounio, Nucl. Fusion **38**, 419 (1998).
6. C. Niemann, Diplomarbeit, IPP 1/316 (Max-Planck Institut für Plasmaphysik, Garching, 1998).
7. A. V. Gurevich and Ya. S. Dimant, in *Reviews of Plasma Physics* (Énergoatomizdat, Moscow, 1987; Consultants Bureau, New York, 1990), Vol. 16.
8. D. Betella, A. Murari, M. Stamp, and D. Testa, Plasma Phys. Controlled Fusion **45**, 1893 (2003).

Translated by N.F. Larionova

Plasma Physics Reports, Vol. 30, No. 2, 2004, pp. 183–186. Translated from Fizika Plazmy, Vol. 30, No. 2, 2004, pp. 205–208.

PLASMA DIAGNOSTICS

Crater Formation in a Target under the Action of a High-Power Laser Pulse

E. A. Bolkhovitinov, B. L. Vasin, S. Yu. Gus'kov, I. Ya. Doskach, A. A. Erokhin, B. V. Kruglov, M. V. Osipov, V. N. Puzyrev, V. B. Rozanov, A. A. Rupasov, V. B. Studenov, S. I. Fedotov, L. P. Feoktistov, A. S. Shikanov, and O. F. Yakushev

Lebedev Physical Institute, Russian Academy of Sciences, Leninskiĭ pr. 53, Moscow, 119991 Russia

Received July 24, 2003

Abstract—The formation of craters in targets of various materials under the action of a high-power neodymium-laser pulse at radiation intensities from 10^{10} to 10^{14} W/cm^2 was studied experimentally and theoretically. The interaction between the laser beam and solid targets is investigated to determine the efficiency of the ablation loading of various materials and the transformation of the laser energy into the energy of a shock wave. *© 2004 MAIK "Nauka/Interperiodica".*

In studying the interaction of a laser beam with a solid target, it is important to determine the fraction of the absorbed laser energy that is transferred to the shock wave propagating in the target. The ratio of the shock-wave energy to the absorbed laser energy is called the ablation loading efficiency [1]. To measure this quantity is an important and a fairly complicated experimental task, especially when opaque materials, in which a shock-wave front is difficult to visualize, are used. In this paper, we propose a rather simple technique for determining the ablation loading efficiency using the aftereffect of a shock wave created by the pressure pulse of a high-temperature plasma produced at the target surface by a high-power laser pulse. As a result of this aftereffect, a crater forms on the target surface. The parameters of the crater are studied in this work.

Experiments were performed using a Kanal single-beam neodymium–phosphate glass laser (which was designed and fabricated at the Lebedev Physical Institute) at a pulse energy of up to 60 J and pulse duration of 1 ns. The experimental setup consisted of a master oscillator, a system for the formation of laser pulses, linear amplifying stages, spatial filter-translators, and a large-aperture Pockels switch to prevent the reflection of radiation from the target back to the amplifiers. The master oscillator with a Q-switched Pockels cell generated a single 50-ns laser pulse with a diffraction-limited divergence and an energy of 50 mJ. A short laser pulse (with a full width at half-maximum of 1 ns) was formed using a two-pass Pockels cell made of a DKDP crystal. The cell is controlled with a laser-triggered spark gap. The formed short pulse goes to the linear amplifying stages that consist of a preamplifier and six amplifiers having apertures increasing from 10 to 45 mm. To prevent small-scale self-focusing, we used spatial filter-translators between the amplifiers to transfer the image of a forming diaphragm to the active elements of the amplifying stages. At the output of the last amplifying stage, the beam divergence is $2\alpha = 1.3 \times 10^{-4}$ rad and the pulse energy contrast is 10^5.

The laser beam was focused by an aspheric lens with a focal length of 48 cm on a target placed in a vacuum chamber. This allowed us to achieve a focal spot $2R_L \sim 100$ μm in diameter with a flux density of $I \leq 5 \times 10^{14}$ W/cm^2 at the target surface. With our computer-assisted system for positioning the target, we were able to place the target at a given point in the vacuum chamber near the center of the beam waist with an accuracy of 10 μm. The Kanal diagnostic system included X-ray, optical, and particle diagnostics, making it possible to measure the main parameters of the laser beam and to study the laser–plasma interaction at targets of various shapes and compositions.

In our experiments, we used solid targets made of aluminum, copper, titanium, lead, tin, germanium, carbon, brass, polyethylene, and other solids. We found the experimental dependences of the parameters of the formed craters on the laser pulse energy and the properties of the target material. The crater profiles were measured using a Form Talysurf computer-assisted profilometer (Taylor Hobson, UK) with an accuracy of 10 μm (Fig. 1). The table gives the crater depths L and the corresponding masses M of ejected material for aluminum, copper, and lead at various laser pulse energies E_{Las}.

To interpret the experimental data, we used the analytical theory of shock-wave propagation in a solid and the model of the ablation destruction of a material when a semi-infinite solid target is subjected to a high-power plasma-forming laser pulse at intensities corresponding to the hydrodynamic regime of interaction [1]. In this regime, energy transfer in a plasma corona proceeds

1063-780X/04/3002-0183$26.00 © 2004 MAIK "Nauka/Interperiodica"

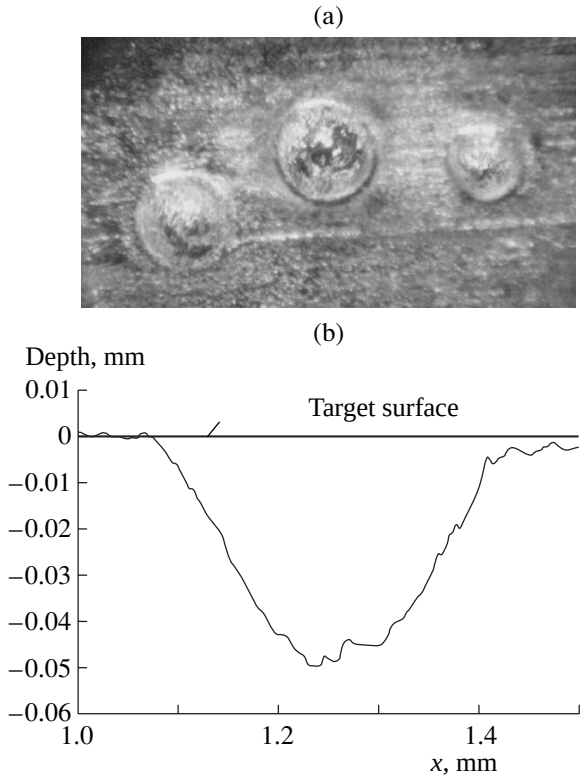

Fig. 1. (a) Photograph of craters formed on the surface of an aluminum target and (b) the measured profile of one of the craters in its diametral section.

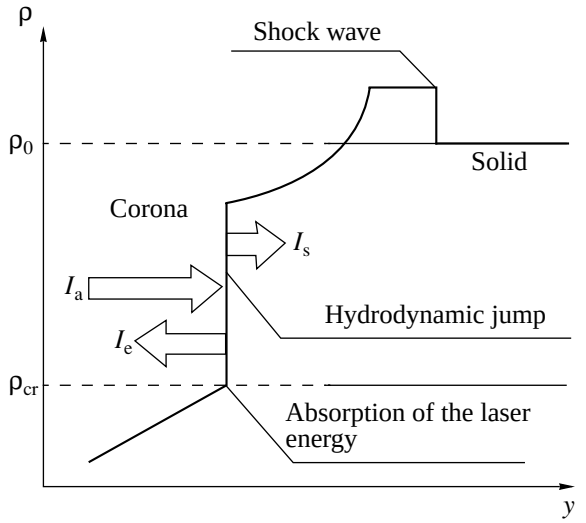

Fig. 2. Schematic diagram of the density profile and energy fluxes for the interaction of a laser beam with a solid target (the *y* axis is directed along the normal to the target surface).

mainly via the plasma hydrodynamic motion rather than due to electron heat conduction and plasma radiation. This condition results in the intensity restriction $I\lambda^2 < 10^{14}$ W μm^2/cm^2 (where λ is the laser wavelength in μm) for low-*Z* materials and $I\lambda^2 < 5 \times 10^{12}$ W μm^2/cm^2 for high-*Z* materials at a pulse duration of $\tau > 0.1$ ns [2, 3].

The interaction of laser radiation with a target results in the melting and evaporation of the target material. The evaporated material forms a plasma corona. The laser radiation is absorbed in the corona in the region with the critical density

$$\rho_{cr}\ [\mathrm{g/cm^3}] \approx 1.83 \times 10^{-3} \frac{\mu}{z\lambda^2}, \qquad (1)$$

where μ is the atomic mass of the material, *z* is the degree of ionization of the plasma corona, and λ is in μm. In the hydrodynamic ablation regime, the region with a critical density is located near the evaporated surface. Therefore, to develop a model, we assume that the radiation is absorbed at the evaporation boundary, which is considered to be a hydrodynamic jump at the target surface. The absorbed energy flux I_a entering the target through a hydrodynamic discontinuity from the side of a low-density plasma then separates into two parts at the jump: the energy flux I_e of the evaporated material ejected from the target and the energy flux I_s that is transferred to a shock wave (Fig. 2). From the continuity conditions of the plane flows of matter, momentum, and energy at the evaporation boundary, we obtain the energy flux density of the evaporated material [3]

$$I_e = \rho_{cr} u_{cr} (\varepsilon_{cr} + p_{cr}/\rho_{cr} + u_{cr}^2/2) \approx \frac{3\gamma_{cr} - 1}{2(\gamma_{cr} - 1)} \rho_{cr} c^3, \qquad (2)$$

where p_{cr}, ρ_{cr}, and γ_{cr} are the pressure, density, and adiabatic exponent of the plasma corona at the point with

Table

Material	E_{Las}, J	Experiment		Theory		M^*/M^0
		L^0, μm	M_0, μg	L^*, μm	M^*, μg	
Al	4.1	89.1	8.26	112.1	8.28	1.00
Al	14.6	126.3	21.6	174.1	24.6	1.14
Al	15.1	164.9	21.5	174.6	25.8	1.19
Al	18.6	103.4	37.3	192.7	32.0	0.86
Cu	12.9	72.6	15.2	105.6	23.9	1.57
Pb	11.8	180.2	123.7	253.5	277.6	2.24

the critical density, respectively; c is the isothermal speed of sound at the critical point; and ε_{cr} and u_{cr} are the specific internal energy and the velocity of the corona material at this point. The velocity of the evaporation wave, which is derived from the continuity equation at the jump, is found to be $V_e = c\rho_{cr}/\rho_0$, where ρ_0 is the initial target density.

We determine the shock-wave energy under the assumption that the pressure behind the shock front (p_s) is equal to the pressure in the absorption region of laser radiation at the evaporation boundary and is the sum of the thermal and reactive components, which are close to one an other [3]. We then have $p_s = 2\rho_{cr}c^2$. In the parameter range under study, this wave travels a short distance within the pulse duration τ, compared to the laser spot radius. Therefore, the shock wave can be considered to be planar throughout the entire pulse. Using Eq. (2) and the expression for the pressure p_s, we obtain for the energy flux feeding the shock wave

$$I_s = \left[1 - \frac{(\gamma_s + 1)V_e}{(\gamma_s - 1)V_s}\right]\frac{2}{(\gamma_s + 1)}V_s p_s \cong \frac{4}{\sqrt{\gamma_s + 1}}\sqrt{\frac{\rho_{cr}}{\rho_0}}\rho_{cr}c^3, \quad (3)$$

where γ_s is the adiabatic exponent of the target material and $V_s = c(\gamma_s + 1)^{1/2}(\rho_{cr}/\rho_0)^{1/2}$ is the speed of the strong shock wave.

Analyzing the energy balance and setting the energy fluxes $I_e + I_s$ equal to I_a, we obtain the ablation loading efficiency $\sigma = I_s/I_a$:

$$\sigma = \left\{1 + \frac{\sqrt{\gamma_s + 1}}{4}\left[\frac{3\gamma_{cr} - 1}{2(\gamma_{cr} - 1)}\right]\sqrt{\frac{\rho_0}{\rho_{cr}}}\right\}^{-1}.$$

Taking into account that the critical density is lower than the initial material density, we arrive at the final simple expression for the ablation loading efficiency [1]:

$$\sigma \cong \frac{4}{\sqrt{\gamma_s + 1}}\frac{2(\gamma_{cr} - 1)}{3\gamma_{cr} - 1}\sqrt{\frac{\rho_{cr}}{\rho_0}}. \quad (4)$$

The ablation loading efficiency increases with decreasing initial material density and increasing critical density, which depends on the laser wavelength λ and z (i.e., the corona temperature). Assuming that $\mu/z \approx 2$ in the expression for the critical plasma density, $\gamma_{cr} = 5/3$ for the evaporated material (for ideal gas), and $\gamma_s = 3$ for the nonevaporated material (for metals) [4], we find that the ablation loading efficiency is 3% for aluminum and about 2% for lead.

Taking into account the smallness of σ, we can calculate the plasma parameters by assuming that the whole absorbed energy is located in the corona. The two-dimensional effects of the corona formation are taken into account using the following model. The cross section through which the energy flux passes from the corona to the dense material can be calculated assuming that the corona has the shape of a truncated cone with a base radius $R_L + \tau c$ and that the absorbed energy flux is uniformly distributed over the corona cross section. In this approximation, according to (2), we have

$$c = \left[\frac{2(\gamma_{cr} - 1)}{3\gamma_{cr} - 1}\frac{I_a}{\rho_{cr}}\frac{R_L^2}{\tau^2}\right]^{1/5}, \quad p_{cr} = 2\left\{\left[\frac{2(\gamma_{cr} - 1)}{3\gamma_{cr} - 1}\right]^2\rho_{cr}^3 I_a^2\left(\frac{R_L^2}{\tau}\right)^4\right\}^{1/5}. \quad (5)$$

In the shock adiabat of metals at pressures close to the elastic limit, the elastic component of the internal energy is about three times greater than the thermal component [4]. Therefore, we believe that the melting condition for a material consists in a fourfold excess of the internal energy of the material behind the shock front over the sum of the heat of melting and the heat consumed to heat the material to the melting temperature:

$$\sigma I_a \tau S \geq 4E_m M, \quad (6)$$

where S is the spot area through which the energy flux passes from the corona to the dense material, $E_m = \varepsilon_m + \int_{T_0}^{T_m} c_v(T)dT$, ε_m is the specific heat of melting, $T_0 = 300$ K is the initial temperature of the target, T_m is the melting temperature, $M = \pi L(L + R_L)^2\rho_0/3$ is the maximum material mass subjected to destruction, c_v is the specific heat, and L is the maximum destruction depth. The crater geometry (i.e., the shape of the region subjected to destruction) is taken to be close to a cone with a depth L and a radius $R_L + L$ at the surface level. Since the corona is two-dimensional, we have to take into account the increase in the spot area through which heat is transferred from the corona to the dense material. Our calculations showed that $S = \pi(R_L + 0.45c\tau)^2$ is a good approximation.

Using Eqs. (4) and (6), we find that, for the material to be melted, the intensity of the laser pulse should be

$$I_a > (\gamma_s + 1)^{3/2}\frac{3\gamma_c - 1}{2(\gamma_c - 1)}\frac{E_m^{3/2}}{\rho_c^{1/2}}\rho_0^{3/2}.$$

This condition was satisfied in all our experiments.

For aluminum, the calculated crater depths and volumes agree well with the experimental data (see table). For high-Z materials (copper and lead), a significant fraction of the energy absorbed by the corona is reradiated as soft X rays; this reduces the shock-wave energy and, hence, the material volume ejected by the shock wave as compared to the calculated values. To take this additional effect into account requires a separate analy-

sis. Note that this effect in copper should be substantially smaller than in lead. As follows from the table, the crater dimensions calculated without regard for reradiation exceed the experimental values by a factor of about 1.6 for copper and more than 2 for lead.

Since the model proposed agrees satisfactorily with the experiment for low-Z materials, it can be used to deduce some parameters of the laser-produced plasma from the measured volume and depth of the formed crater. For example, it is of interest to determine the pressure in the corona. Using Eq. (3) and taking into account $V_e \ll V_s$, we have

$$I_s = \sigma I_a = \sqrt{\frac{2p_s^3}{(\gamma_s + 1)\rho_0}}.$$

From here, using condition (6), we can find the pressure

$$p_{\rm cr} \equiv \frac{1}{2}p_s = (\gamma_s + 1)^{1/3}\left[\frac{E_{\rm m}M\sqrt{\rho_0}}{\tau\pi(R_L + 0.4\tau c)^2}\right]^{2/3},$$

where c is specified by Eq. (5). For aluminum, the pressures were found to be 2.07, 2.76, 2.80, and 2.95 Mbar for pulse energies of 4.1, 14.6, 15.1, and 18.6 J, respectively. Further development of a theory for high-Z materials with allowance for reradiation and the exact calculation of the degree of ionization in the corona will allow us to determine the pressure in the shock wave and in the corona for a wide class of materials by a rather simple method.

ACKNOWLEDGMENTS

This work was supported by the Russian Foundation for Basic Research, project nos. 01-02-17589 and 02-02-16966.

REFERENCES

1. K. S. Gus'kov and S. Yu. Gus'kov, Kvantovaya Élektron. (Moscow) **31**, 305 (2001).
2. S. I. Anisimov, Ya. A. Imas, G. S. Romanov, and Yu. A. Khodyko, *The Action of High-Power Radiation on Metals* (Nauka, Moscow, 1970).
3. Yu. V. Afanas'ev and S. Yu. Gus'kov, *Nuclear Fusion by Inertial Confinement*, Ed. by G. Velarde *et al.* (CRC, Ann Arbor, 1993), p. 99.
4. Ya. B. Zel'dovich and Yu. P. Raizer, *Physics of Shock Waves and High-Temperature Hydrodynamic Phenomena* (Nauka, Moscow, 1966; Academic Press, New York, 1967).

Translated by K. Shakhlevich

Plasma Physics Reports, Vol. 30, No. 2, 2004, pp. 99–110. Translated from Fizika Plazmy, Vol. 30, No. 2, 2004, pp. 115–128.

PLASMA DIAGNOSTICS

X-ray Backlighting of the Axial Region of a Multiwire Liner Plasma in the Angara-5-1 Facility

G. S. Volkov, E. V. Grabovskiĭ, K. N. Mitrofanov, and G. M. Oleĭnik

Troitsk Institute for Innovation and Fusion Research, Troitsk, Moscow oblast, 142190 Russia

Received July 22, 2003

Abstract—Results are presented from experiments on the X-ray backlighting of the axial region of an imploding high-current multiwire liner. Backlighting was performed with the use of an X-pinch serving as a source of soft X-ray emission, which was recorded by pin diodes. The use of several filters with different passbands in front of the pin diodes allowed the interpretation of the results of measurements in experiments with cascade composite liners. The sensitivity of the diagnostics was ≈125 μg/cm^2 for a plasma of high-Z elements (W) and ≈220 μg/cm^2 for a plasma of low-Z elements (C, O, N) at a photon energy of the probing radiation of 1.0–1.5 keV. An advantage of the method is its high time resolution (≈1 ns) and the possibility of the separation in time of the emission bursts from Z- and X-pinches on the liner axis. The method does not impose restrictions on the pulse duration of the backlighting radiation source. © *2004 MAIK "Nauka/Interperiodica".*

1. INTRODUCTION

At present, the implosion of high-current multiwire liners is being actively investigated. In the Angara-5-1 facility, the implosion of a multiwire liner under the action of a current pulse with an amplitude of 4 MA and a rise time of ≈100 ns is accompanied by the generation of a soft X-ray (SXR) pulse with a peak power of ~3–5 TW and full width at half-maximum of ~6–10 ns at the instant of plasma collapse on the liner axis. It has been shown that, in such systems, the plasma is produced over almost the entire implosion process (≈100 ns), until the wires that serve as the plasma sources completely evaporate (the so-called prolonged plasma production [1]).

In the context of prolonged plasma production, there is much physical interest in studying the mass spatial distribution inside the wire array in the course of implosion and especially at the instant of SXR burst.

One of the methods that can be used in such studies is backlighting the imploding liner with X radiation generated by an X-pinch [2]. In this case, the time behavior of the liner can be monitored by semiconductor detectors (pin diodes) equipped with different filters [3]. In our experiments on the absorption of X-ray emission in plasma, the plasma mass density integrated along the probing beam (in g/cm^2) was measured in the axial region of the liner.

In some experiments on the X-ray backlighting of the axial region of a wire liner, targets made of porous materials (e.g., agar–agar foam) with an average density $\rho_{AA} \approx 3$–20 mg/cm^3 and a characteristic linear mass density of 200–1100 μg/cm were placed on the liner axis. We also used agar–agar targets doped with a fine grain powder of refractory materials, e.g., 50–60% (by weight) of metallic tungsten powder with a mean grain diameter of 3–10 μm. The dopant was necessary to ensure the required X-ray emissivity of the foam plasma.

It should be noted that the degree of evaporation of tungsten grains embedded in a polymer foam under the action of SXR emission is still unknown. This knowledge is important in interpreting the experimental data and modeling the foam emission characteristics in experiments on creating dynamical hohlraums for irradiating thermonuclear targets [4]. This is why we performed experiments on the X-ray backlighting of a foam doped with a fine tungsten powder.

2. PROBING TECHNIQUE

The transmission coefficient K of probing radiation (the intensity ratio of the transmitted radiation to the radiation incident onto the plasma and recorded in the reference channel) depends on the plasma density ρ. The absorption coefficient is determined by the integral of the plasma mass density along the probing beam $\int \rho(x)dx$. We will call this integral the surface density ρl [g/cm^2] along the probing beam. The transmission coefficient K is equal to $\exp(-\mu(h\nu)\rho l)$, where $\mu(h\nu)$ [cm^2/g] is the mass absorption factor for photons with energy $h\nu$ (the absorption coefficient is $1 - K$). Thus, by measuring K, one can find ρl using Beer's law

$$\rho l = -\ln(K)/\mu(h\nu).$$

There are two problems that hinder the use of this formula:

The first of these is that the mass absorption factor at temperatures lower than the ionization energy differs from that seen in the course of implosion, when the temperature of the plasma varies from 20–30 eV before

1063-780X/04/3002-0099$26.00 © 2004 MAIK "Nauka/Interperiodica"

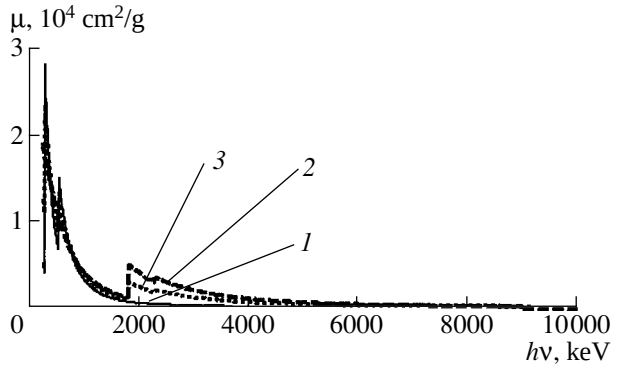

Fig. 1. Mass absorption factor μ of (*1*) an agar–agar polymer base, (*2*) tungsten, and (*3*) an agar–agar polymer base with a uniformly distributed tungsten powder (the weight fraction of tungsten is 50%).

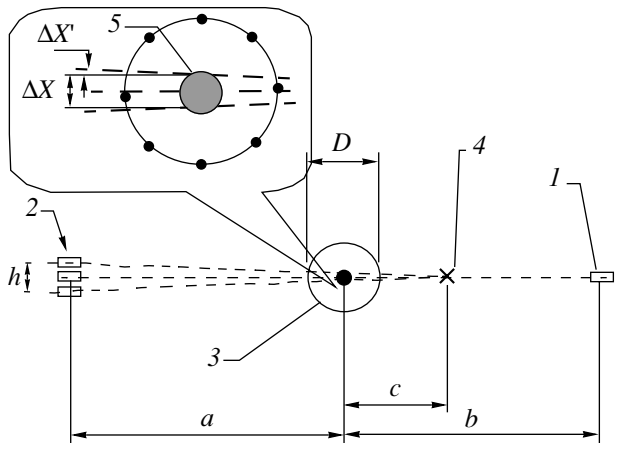

Fig. 2. Schematic of the experiment on X-ray backlighting of the liner axial region (top view): (*1*) reference pin diodes (3 diodes with different filters), (*2*) measuring pin diodes (3 diodes with the same filters), (*3*) multiwire array, (*4*) X-pinch radiation source, and (*5*) axial region of the discharge.

the collapse to 300–400 eV at the instant of maximum compression. Further, we use the values of the mass absorption factors at temperatures at which ionization is absent, assuming that, at least up to the instant of maximum compression (i.e., at plasma temperatures of 20–30 eV) and for photon energies higher than 1.0 keV, this difference will be insignificant.

The second problem is that the X-pinch emission spectrum is rather wide and the mass absorption factor $\mu(h\nu)$ strongly depends on $h\nu$; hence, the transmission coefficient K also depends strongly on $h\nu$. Therefore, it is necessary to know the shape of the X-pinch emission spectrum.

The mass absorption factors of composite substances are additive functions of the weight concentrations of the elements that are present in the substance in either free or bound states. Summation is performed over all the elements present in a complex molecule. Thus, the mass absorption factor $\mu_{AA}(h\nu)$ of the agar–agar $(C_{14}H_{18}O_9)_n$ polymer base, which contains mainly carbon, hydrogen, and oxygen, is

$$\mu_{AA}(h\nu) = \frac{m_c}{m_{AA}}\mu_C(h\nu) + \frac{m_H}{m_{AA}}\mu_H(h\nu) + \frac{m_0}{m_{AA}}\mu_O(h\nu),$$

where the $\mu_i(h\nu)$ are the mass absorption factors of the constituent elements, m_i/m_{AA} are the weight fractions of the elements (i = C, H, and O), and m_{AA} is the mass of agar–agar.

The mass absorption factor of agar–agar calculated in this way is shown in Fig. 1 (curve *1*). For comparison, the mass absorption factor of tungsten is also shown (curve *2*). The dependences of the mass absorption factors on the photon energy are taken from [5].

A specific feature of probing Z-pinches with X-pinch radiation is that the Z-pinch itself is a much more powerful X-ray source than the X-pinch; hence, it can significantly contribute to the output signal of the recording device (here, the pin diode).

It was shown in [3] that, in the photon energy range of 1–20 keV, the power and energy of X-pinch emission are ~200–300 MW and 200–700 mJ, respectively; i.e., they are lower than the power and energy of Z-pinch emission in the same photon energy range. Hence, to monitor the emission intensity of an X-pinch in the presence of intense Z-pinch emission, it is necessary to substantially reduce the intensity of Z-pinch emission in the region where the radiation detectors are placed. To do this, the radiation received by the pin diodes from the X- and Z-pinches was selected not only in photon energy (by the filter method) but also in time. The drawback of this method compared to the recording of X-pinch emission on an X-ray film is that, in this case, only a few probing beams (in our case, three) are used, whereas the recording on an X-ray film provides a two-dimensional image [6]. In the latter case, however, when recording the radiation passed through an object, one has to either know the film characteristic curve or use a special set of calibrated filters (the so-called step attenuator) made of the same material as the object under study. The latter method is rather difficult to implement because very thin filters are required (<1 μm for tungsten).

An advantage of monitoring with pin diodes is that there is no need to use a short-duration X-ray source. In contrast, the longer the probing radiation pulse, the more data about the object under study can be acquired.

In all the cases, the soft component of X-ray emission (with a photon energy of less than 1 keV) from both the X- and Z-pinches was cut off by filters placed in front of the detectors.

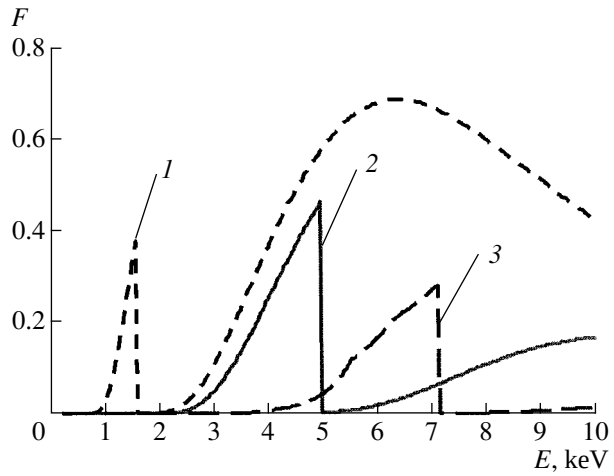

Fig. 3. Relative spectral sensitivity F of a pin diode equipped with (*1*) 10-μm Al, (*2*) 20-μm Ti, and (*3*) 26-μm Fe filters.

3. EXPERIMENTAL SETUP

A schematic of the experiment on X-ray backlighting of the axial region of the liner is shown in Fig. 2.

X-pinch radiation was monitored by six pin diodes. Three of these (*1*) served as reference diodes and monitored the nonattenuated X-pinch radiation, whereas the other three (*2*) monitored the X-pinch radiation passed through the axial region of the liner and attenuated by the substance residing at the moment in this region. The latter three diodes (measuring diodes) were located at a distance of $a \approx 2.6$ m from the liner axis, the distance between the two outmost detectors being $h = 6$ cm. The reference diodes were located at a distance of $b \cong 3.2$ m from the liner axis. The distance between the X-pinch source and the liner axis was $c \approx 4.5$ cm. The viewing fields of the group of the three measuring diodes, ΔX, and of one of them, $\Delta X'$, were

$$\Delta X = \frac{hc}{a+c} \cong 1.0 \text{ mm}, \quad \Delta X' = \frac{c}{a+c} d_w \approx 44 \text{ μm},$$

where d_w is the diameter of the detector input window. Therefore, the group of the three measuring diodes monitored a ≈1-mm region across the object, whereas an individual detector observed a narrow ≈44-μm region.

The three reference pin diodes were equipped with a 10-μm Al, 20-μm Ti, and 26-μm Fe foils. The same foils were set in front of the measuring diodes. In some experiments, a Ni mesh with a transmittance of 39% was set along with the Al foil. The relative spectral sensitivities of the detectors in combination with the foils is shown in Fig. 3.

In all the experiments, we used an X-pinch consisting of four 20-μm Mo wires. The X-pinch was set in such a way that the array wires did not to fall into the viewing field of the detectors.

By the sensitivity of this diagnostics, we mean the minimum surface density of an absorber at which the difference between the unity and the transmission coefficient K exceeds the relative error of detector calibration.

To estimate the sensitivity, we considered the radiation absorption in two different media: (i) a tungsten plasma with a surface density from 40 to 2100 μg/cm^2 and (ii) a plasma formed from a cylindrical column of agar–agar foam with a surface density in the range of 50–4000 μg/cm^2.

The spectral dependences of the absorption coefficients for tungsten and agar–agar are shown in Figs. 4a and 4b, respectively.

In our experiments, significant radiation absorption in tungsten and agar–agar was observed when the pin diodes were placed behind a 10-μm Al foil. The corre-

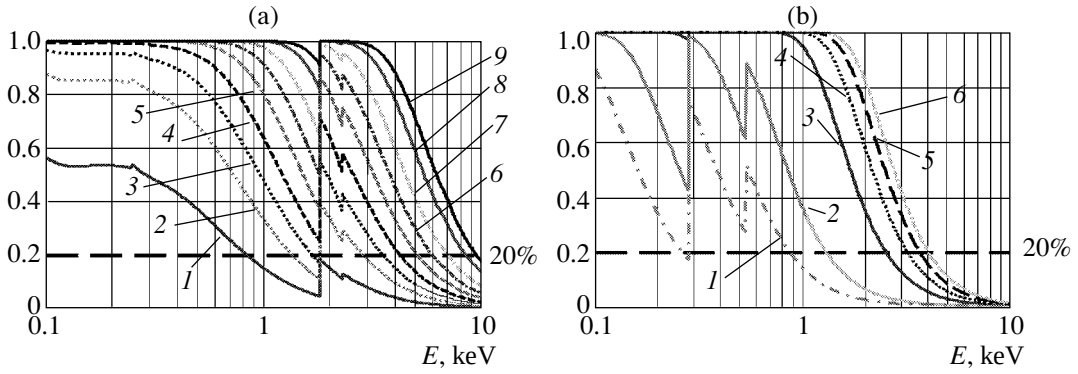

Fig. 4. Spectral dependence of the absorption coefficient in (a) tungsten with a surface density of (*1*) 40, (*2*) 100, (*3*) 160, (*4*) 250, (*5*) 400, (*6*) 600, (*7*) 900, (*8*) 1500, and (*9*) 2120 μg/cm^2 and (b) agar–agar foam with a surface density of (*1*) 50, (*2*) 150, (*3*) 1000, (*4*) 2000, (*5*) 3000, and (*6*) 4000 μg/cm^2.

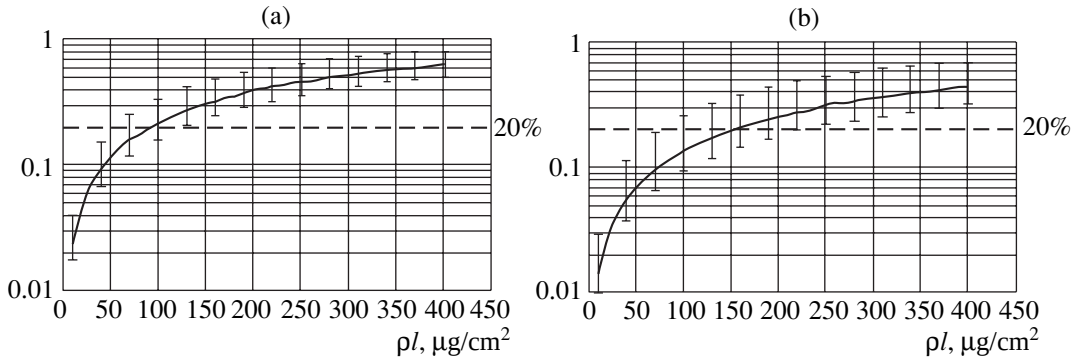

Fig. 5. Absorption coefficient of X-ray emission with a photon energy of E = 1.3 keV in (a) tungsten and (b) agar–agar foam as a function of the surface density ρl. The vertical bars show the range of the absorption coefficient values for X-ray emission with photon energies from 1 to 1.5 keV.

sponding photon energy range is 1–1.5 keV. The X-ray absorption coefficients for tungsten and agar–agar in this photon energy range as functions of the surface density are shown in Figs. 5a and 5b, respectively.

Since the detectors were calibrated with a relative error of 15–20% [3], the dynamic range of the recorded absorption coefficients is 0.2–0.8. It follows from Figs. 4 and 5 that, for photon energies of 1–1.5 keV (a pin diode behind a 10-μm Al foil), the dynamic range of the surface densities measured with this diagnostics is 125–1000 μg/cm^2 for tungsten and 220–1400 μg/cm^2 for agar–agar foam.

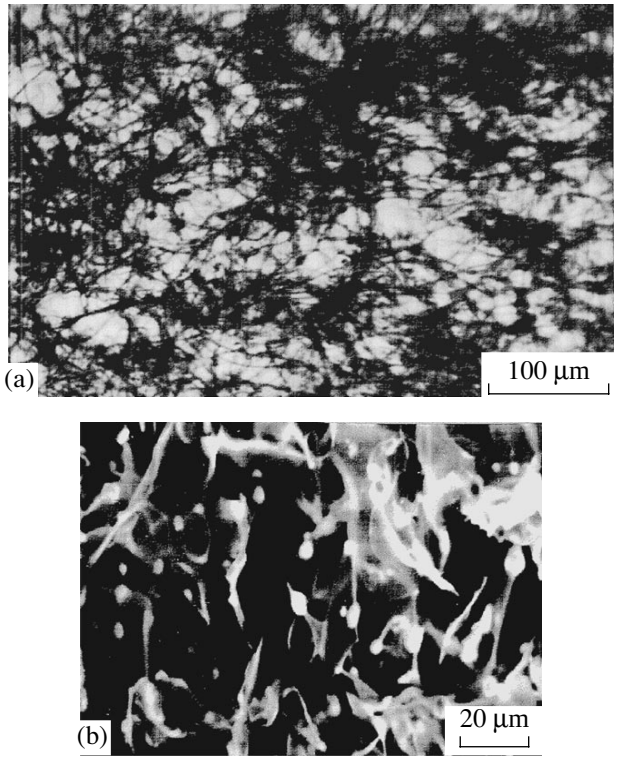

Fig. 6. Photographs of the agar–agar foam: (a) optical photomicrograph of the agar–agar polymer foam with a specific mass density of 2 mg/cm^3 and thickness of 150 μm and (b) X-ray photomicrograph of the agar–agar polymer foam with a specific mass density of 2 mg/cm^3 impregnated with a tungsten powder with a mass density of 2 mg/cm^3.

Thus, to allow the reliable interpretation of the data from the backlighting of the liner axial region, the latter must contain (at the instant of the X-pinch emission pulse) tungsten with a surface density of higher than 125 μg/cm^2 or agar–agar foam with a surface density of higher than 220 μg/cm^2. These values are the diagnostic sensitivities for probing radiation with photon energies from 1 to 1.5 keV. The sensitivity can be enhanced by a factor of 2–4 (to ≈50 μg/cm^2 for tungsten and to ≈60 μg/cm^2 for agar–agar foam) by operating in the photon energy range of 800–900 eV, in which the mass absorption factors of these materials is higher (see Fig. 4).

4. PARAMETERS OF THE LOADS

We used cylindrical tungsten wire arrays with the following parameters: the initial diameter of the array was 12 mm, the wire diameter was 6 μm, the number of wires in the array was 30 or 40, and the liner length was 15 mm.

Two types of agar-agar targets were placed on the liner axis:

(i) A hollow agar–agar cylinder (a diameter of ≈5 mm, wall thickness of ≈400 μm, and length of 9 mm) positioned in the interelectrode gap from the anode side in such a way as to fall into the viewing field of all of the three measuring detectors, as is schematically shown in Fig. 8a. The linear density of this foam column was 1100 μg/cm. The surface density of the agar–agar was $\rho l_{AA} \approx 1500$ μg/cm^2.

(ii) A solid cylindrical agar–agar column (Figs. 10 and 12) filled with a micron-size tungsten powder. The

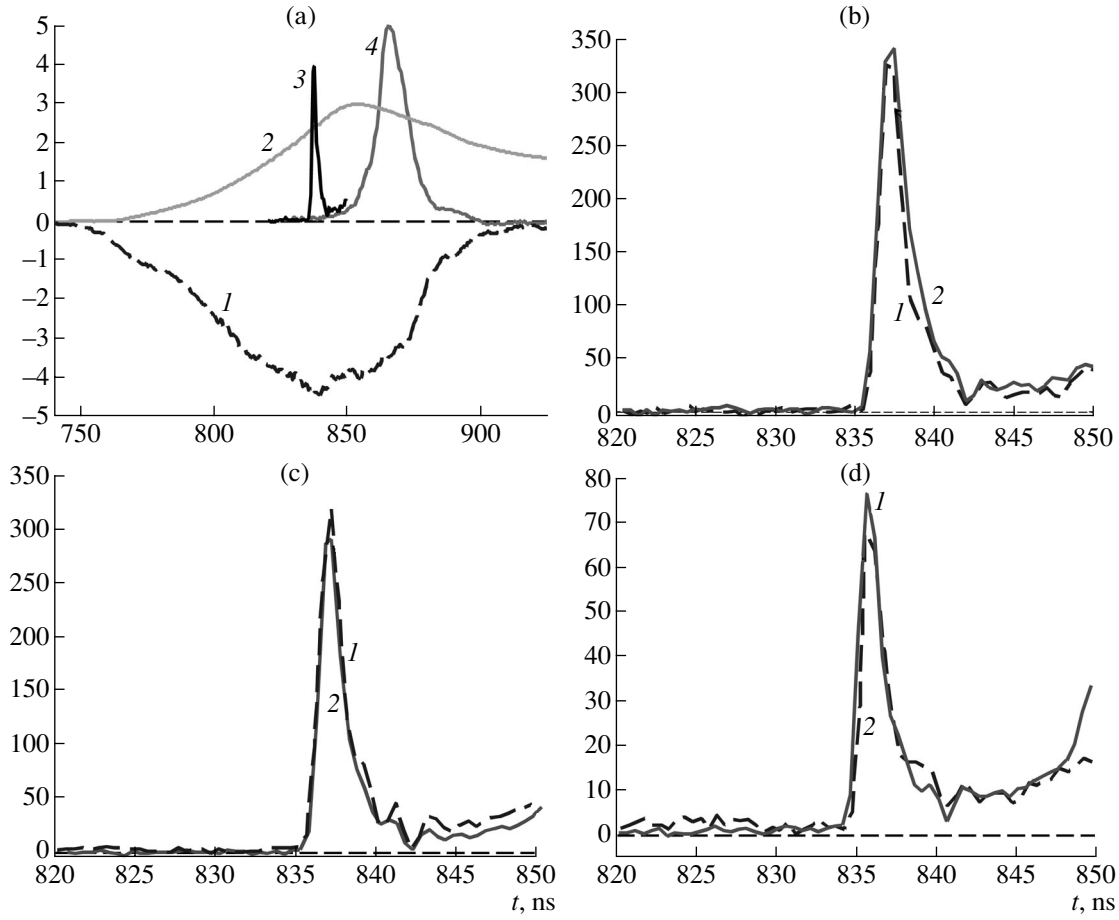

Fig. 7. Results of experiments with load 1: (a) waveforms of (*1*) the voltage across the interelectrode gap (in units of 100 kV), (*2*) the current within the region of radius $r = 55$ mm (in MA), (*3*) the X-pinch emission power (in arb. units), and (*4*) the power of SXR emission from the Z-pinch (in units of 0.75 TW) and (b)–(d) signals from the (*1*) reference and (*2*) measuring detectors (in arb. units) behind (b) a 10-μm Al foil plus a Ni mesh with a transmittance of 39%, (c) a 20-μm Ti foil, and (d) a 26-μm Fe foil. The curves in plots (b)–(d) present the signals from the detectors U_i multiplied by $U_i r_i^2$, where r_i is the distance between the X-pinch and the *i*th detector ($i = 1, 2$).

surface density of agar–agar, in this case, was $\rho l_{AA} \approx$ 770–970 μg/cm^2.

Experiments were performed with four combinations of the wire liner and foam target (see table).

5. COMPOSITION AND STRUCTURE OF THE AGAR–AGAR FOAM

Agar-agar is a natural water-soluble polymer $(C_{14}H_{18}O_9)_n$ derived from certain species of red sea-

Parameters of loads in experiments on X-ray backlighting of the liner axial region

No.	Parameters of the wire liner	Parameters of the foam target on the liner axis
1	40 6-μm tungsten wires. The liner diameter was 12 mm. The linear density was 220 μg/cm.	Absent
2	30 6-μm tungsten wires. The liner diameter was 12 mm. The linear density was 165 μg/cm.	Hollow agar–agar foam cylinder with a diameter of 5 ± 0.5 mm, wall thickness of ≈400 μm, and length of 9 mm. The linear density was 1100 μg/cm.
3	40 6-μm tungsten wires. The liner diameter was 12 mm. The linear density was 220 μg/cm.	Cylindrical agar–agar foam column (≈1.65 mm in diameter and 15 mm in length) filled with a tungsten powder with a grain size from 3 to 10 μm. The total mass density was 250 μg/cm (the weight fraction of tungsten was 60%).
4	40 6-μm tungsten wires. The liner diameter was 12 mm. The linear density was 220 μg/cm.	Cylindrical agar–agar foam column (≈2.9 mm in diameter and 15 mm in length) filled with a micron-size tungsten powder. The total linear mass density was 550 μg/cm (the weight fraction of tungsten is was 60%).

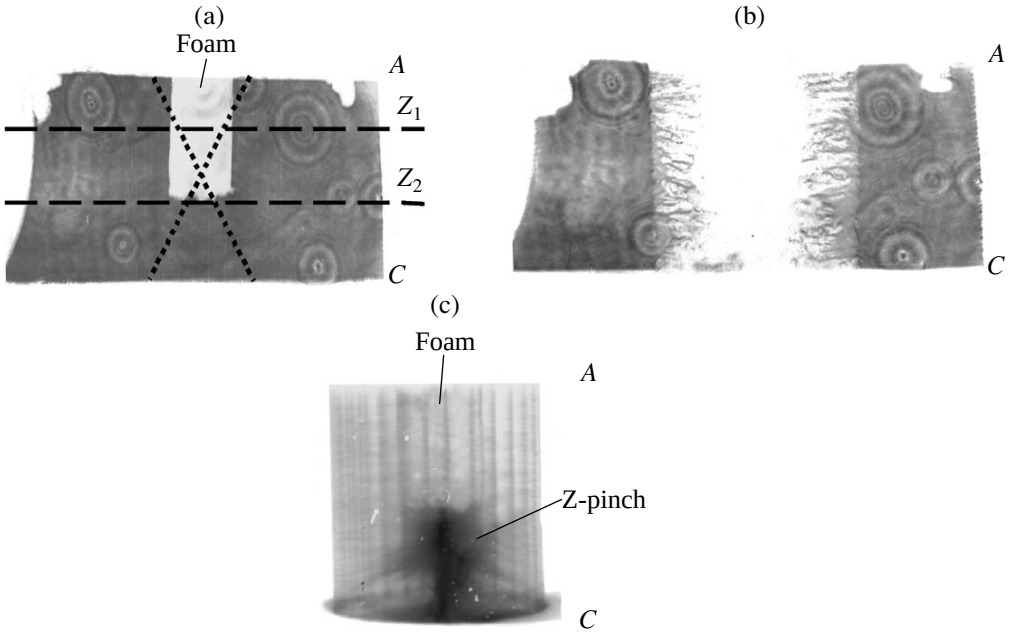

Fig. 8. Images of load 2: (a) laser shift interferogram of a multiwire liner with a hollow agar–agar foam cylinder on its axis before the discharge (the dashed lines show the positions of the X-pinch and the slits of the streak camera monitoring the radial distribution of the optical emission intensity at distances of Z_1 = 11 mm and Z_2 = 6 mm from the liner cathode), (b) laser shift interferogram of a multiwire liner at the 110th ns from the beginning of the discharge, and (c) time-integrated X-ray ($h\nu$ > 200 eV) pinhole image of a multiwire liner.

weed. It is 90% composed of hydrocarbons [7, 8]. An agar–agar target is a low-density microheterogeneous solidlike foam in the form of a solid or hollow cylinder. The deviation from the cylindrical shape is fractions of a millimeter. The foam consists of randomly directed solid fibers ($\rho \approx 0.9$–1 g/cm^3) with characteristic transverse dimensions of $d \approx 1$–5 μm and a distance between the fibers (the pore size) of $r_p \approx 10$–50 μm. There are also fibers with $d_f \approx 10$ μm, but they are small in number. The fiber length is $l_f \approx 10$–50 μm (so that $l_f \gg d_f$).

Figure 6 presents optical and electron photomicrographs of the foam. These two-dimensional images (with a depth resolution of ~150 μm) show that the solid phase has the form of a chaotic mesh. The tungsten powder grains are distributed relatively uniformly over the structure and do not form large clusters (agglomerates).

The question naturally arises as to the mechanism for X-ray absorption in such a fine-mesh medium impregnated with a fine grain powder. There may be two limiting situations:

(i) Radiation is completely absorbed in powder grains or microfibers and the attenuation of radiation is determined by the overlap of the probing beam by these structural elements.

(ii) Radiation is attenuated in a substance with a uniform distribution of the mass density $\rho(x, y, z)$.

However, an intermediate case is possible in which all the structural elements are semitransparent for photons with a given energy. In this case, it is necessary to consider not only the overlap of the beam by the structural elements but also the absorption of radiation in the individual elements.

To determine the degree of foam homogeneity, we estimated the coefficient of beam overlapping K_f by agar–agar fibers with characteristic dimensions d_f and l_f over the radiation path length l by the following formula [9]:

$$K_f = n_f S_f l,$$

$$n_f = \frac{\rho_{AA}}{\rho_f}\frac{1}{S_f l_f},$$

where $S_f = (0.5\ d_f)^2$ is the fiber cross-section area and n_f is the average number of fibers per unit volume of the substance under study. Depending on the characteristic size of the foam target ($l \approx 0.8$–2.9 mm), the coefficient K_f varied from 10 to 20.

Thus, it can be said with confidence that, at the probing length l, the X-ray beam completely overlapped with the agar–agar fibers. This case is similar to the that of a homogeneous substance.

During a liner implosion, the situation becomes more complicated because the tungsten grains expand under the action of high-power energy fluxes (SXR emission and Joule heating by a megaampere current) and gradually fill the pore space in the foam, the originally solid agar–agar fibers evaporate, and the degree of foam homogeneity gradually increases.

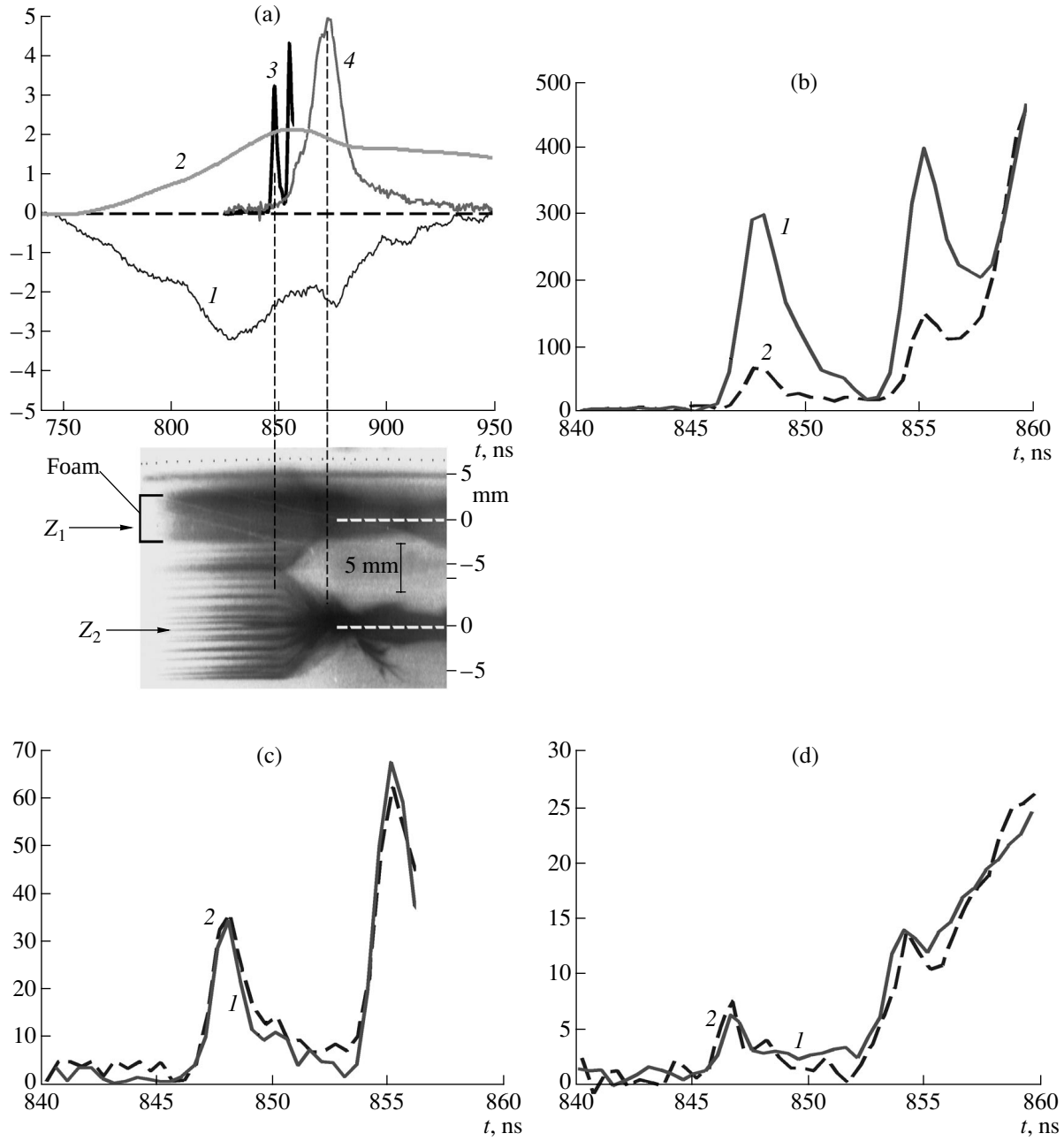

Fig. 9. Results of experiments with load 2: (a) waveforms of (*1*) the voltage across the interelectrode gap (in units of 100 kV), (*2*) the current within the region of radius r = 55 mm (in MA), (*3*) the X-pinch emission power (in arb. units), and (*4*) the power of SXR emission from the Z-pinch (in units of 0.34 TW) and (b)–(d) signals from the (*1*) reference and (*2*) measuring detectors (in arb. units) behind (b) a 10-μm Al foil, (c) a 20-μm Ti foil, and (d) a 26-μm Fe foil. A two-slit optical streak image of the liner is shown below plot (a) (the image is synchronized with the above waveforms). The distances of the slits from the liner cathode are Z_1 = 11 mm and Z_2 = 6 mm (see Fig. 8a). The curves in plots (b)–(d) present the signals from the detectors U_i multiplied by $U_i r_i^2$, where r_i is the distance between the X-pinch and the ith detector (i = 1, 2).

It can be seen from Fig. 4b that the agar–agar material itself ($\rho l_{AA} > 700$ μg/cm^2) is a strongly absorbing agent for radiation with photon energies from 1 to 1.5 keV (the absorption coefficient ranges from ~60 to ~90%). To determine which state the tungsten grains are in at the instant of an X-pinch burst, it is necessary to subtract the contribution of the agar–agar polymer base to the absorption of probing radiation. For this purpose, the object under study is probed with radiation with different photon energies, e.g., in the photon energy range of 3–7 keV, in which radiation is weakly absorbed by the agar–agar foam (the absorption coeffi-

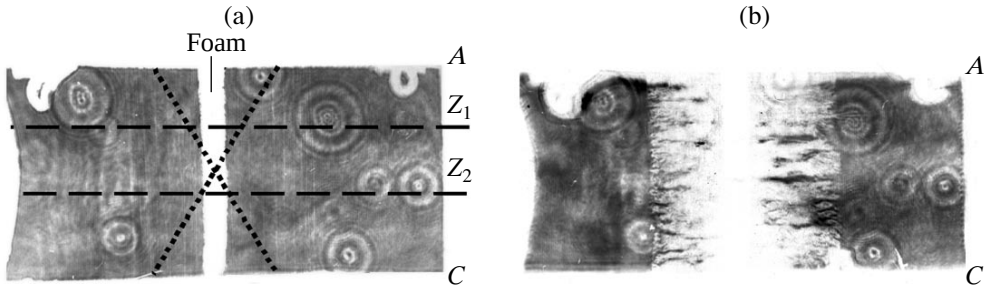

Fig. 10. Images of load 3: (a) laser shift interferogram of a multiwire liner with a solid agar–agar foam cylinder on its axis before the discharge (the dashed lines show the positions of the X-pinch and the slits of the streak camera monitoring the radial distribution of the optical emission intensity at distances of Z_1 = 11 mm and Z_2 = 6 mm from the liner cathode) and (b) laser shift interferogram of a multiwire liner at the 135th ns from the beginning of the discharge.

cient is lower than 10%; see Fig. 4b, curve *3*), whereas the absorption by completely evaporated tungsten ($\rho l_W > 1500$ μg/cm^2) exceeds 50% (Fig. 4a, curves *8* and *9*).

Such measurements will allow us to answer the question about the tungsten state in the foam: whether it is still in individual grains or uniformly fills the foam volume.

6. BACKLIGHTING OF THE LINER AXIAL REGION

Here, we present the results on X-ray backlighting of the axial region of the loads described in the table.

6.1. Experiments with Load 1

Figure 7a shows the waveforms of the voltage across the interelectrode gap, the current within the region of radius r = 55 mm, the X-pinch emission power, and the power of SXR emission from the Z-pinch. It can be seen that the X-pinch burst occurs at the 82nd ns after the beginning of the discharge, when the current through the liner reaches ≈2 MA.

The experimental results on the absorption of X-pinch emission in load 1 are shown in Figs. 7b–7d. It can be seen that the absorption coefficient is less than the measurement error in all three recording channels. This is proof that, at the instant of the X-pinch burst (t = 82 ns), the surface density of the tungsten plasma in the axial region of the liner is lower than 120 μg/cm^2. Hence, the contribution of the precursor plasma to the absorption of the probing X-ray emission from the X-pinch is negligibly small. This confirms the early results on the X-ray backlighting of the liner periphery at the same instant [10]. It was shown in [10] that the bulk of the wire mass (up to 70%) is concentrated in dense cores, whereas the rest of the mass is spread out toward the axis over a distance of ≈200 μm.

We note that the evaporating wire cores residing at the initial wire positions can fall into the viewing field of the measuring diodes. In some experiments, we observed the absorption of X-pinch radiation due to the partial overlap of the viewing field of the pin diodes by these cores.

6.2. Experiments with Load 2

In these experiments, a hollow agar–agar foam cylinder was placed on the liner axis. The cylinder resided on the anode side of the interelectrode gap and fell within the viewing field of all three measuring detectors, as is shown schematically in Fig. 8a. The pin diodes were adjusted so that the wire cores did not fall within the viewing field of the detectors. Figure 9a shows the waveforms of the voltage across the interelectrode gap, the current within the region of radius r = 55 mm, the X-pinch emission power, and the power of SXR emission from the Z-pinch. It can be seen that the X-pinch burst occurs at the 97th ns after the beginning of the discharge, when the current through the liner reaches ≈2 MA.

The experimental results on the absorption of the X-pinch emission in load 2 are shown in Figs. 9b–9d.

The dashed lines in Fig. 8a show the positions of the X-pinch and the slits of the streak camera monitoring the radial distributions of the optical emission intensity at distances of Z_1 = 11 mm and Z_2 = 6 mm from the cathode. At the instant of the X-pinch burst (t = 97 ns), the outer boundary of the liner has just begun to move toward the axis (see the streak image in Fig. 9a). It can be seen that, at t = 97 ns, the foam cylinder still retains its initial size and does not shrink during the liner implosion. This is also indirectly confirmed by an integral pinhole image shown in Fig. 8c, where the Z-pinch is clearly seen to form above the foam cylinder. It is seen from Fig. 8b that, at t = 110 ns, there is still some plasma at the liner periphery (at the initial wire positions).

The absorption coefficient of X-pinch emission recorded behind an Al foil was ≈80% (see Fig 9b). The absorption coefficient of X-pinch emission recorded behind Ti and Fe foils was less than the measurement error (<10–20%) (see Figs. 9c, 9d). The Al foil differs

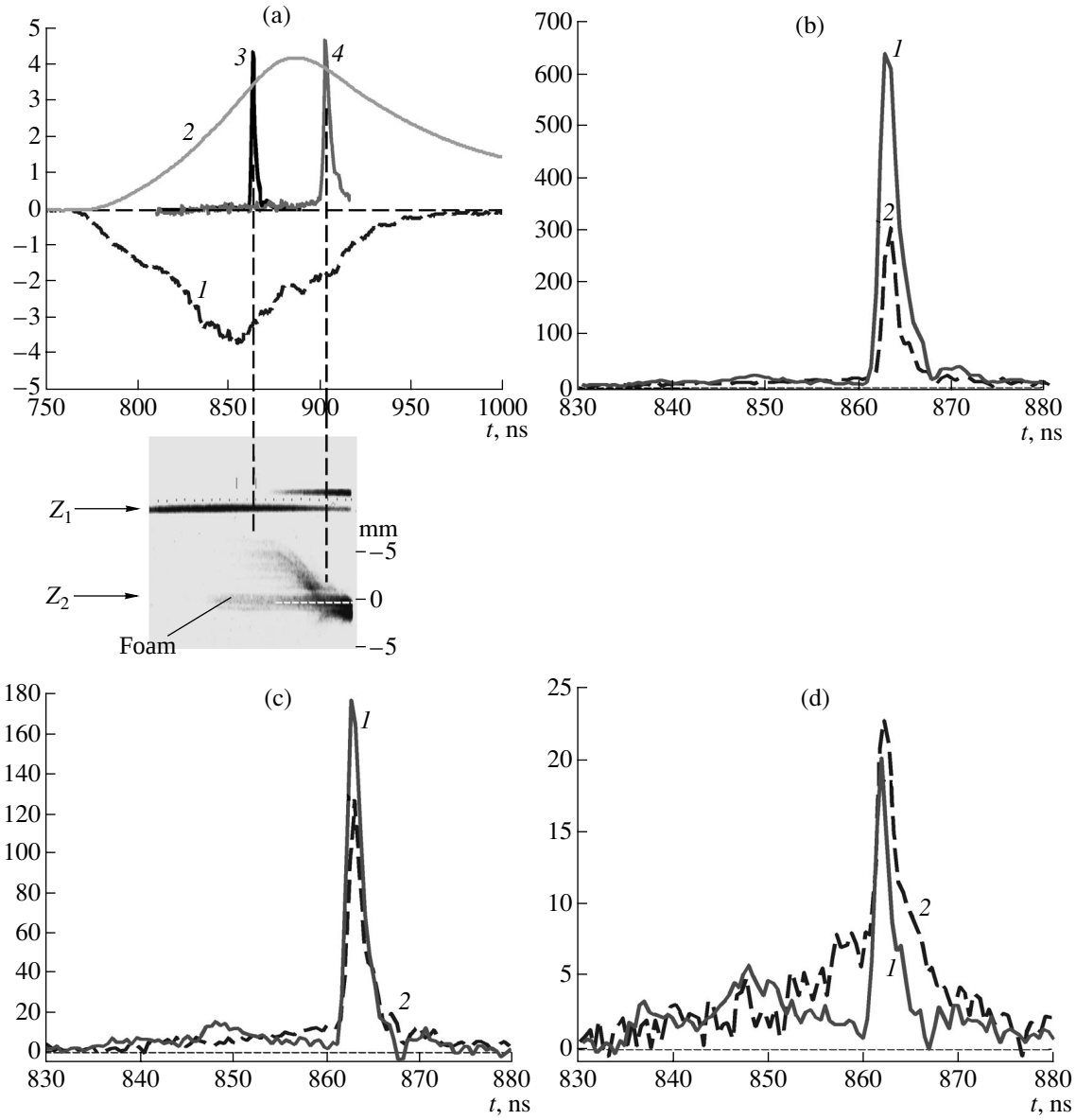

Fig. 11. Results of experiments with load 3: (a) waveforms of (*1*) the voltage across the interelectrode gap (in units of 100 kV), (*2*) the current within the region of radius $r = 30$ mm (in units of 0.4 MA), (*3*) the X-pinch emission power (in arb. units), and (*4*) the power of SXR emission from the Z-pinch (in arb. units) and (b)–(d) signals from the (*1*) reference and (*2*) measuring detectors (in arb. units) behind (b) a 10-μm Al foil, (c) a 20-μm Ti foil, and (d) a 26-μm Fe foil. Below plot (a), an optical streak image of the liner is shown (the image is synchronized with the above waveforms). The distance of the slit from the liner cathode is $Z_2 = 6$ mm (see Fig. 10a). The curves in plots (b)–(d) present the signals from the detectors U_i multiplied by $U_i r_i^2$, where r_i is the distance between the X-pinch and the *i*th detector ($i = 1, 2$).

from the other two in that its passband lies in the photon energy range 1–1.5 keV (Fig. 3, curve *1*). Consequently, a detector equipped with an Al foil monitors radiation mainly in the spectral range of 1–1.5 keV. The absorption of radiation with photon energies of >3 keV is low. This, indeed, should be the case because the agar–agar foam is almost transparent for photons in this energy range (Fig. 4b; curves *3*, *4*).

Nevertheless, photons with energies of >3 keV are present in the X-pinch emission. This is evidenced by the presence of signals from the detectors equipped with Ti (Fig. 9c) and Fe (Fig. 9d) foils. Photons with such energies contribute only slightly to the signal from the detector equipped with an Al filter. This radiation was taken into consideration by solving an ill-posed problem of the simultaneous reconstruction of the sought ρl value and the rough characteristics of the X-pinch emission spectrum. A similar method was used in the experiments on Z-pinches and the implosion of cascade liners in the Angara-5-1 facility [11].

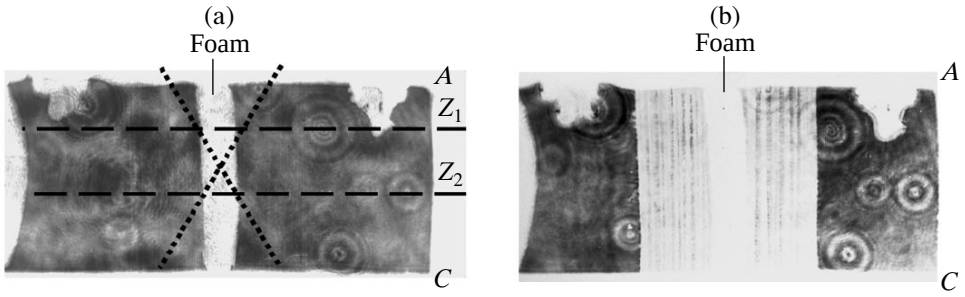

Fig. 12. Images of load 4: (a) laser shift interferogram of a multiwire liner with a solid agar–agar foam cylinder on its axis before the discharge (the dashed lines show the positions of the X-pinch and the positions of the streak camera monitoring the radial distribution of the optical emission intensity at distances of Z_1 = 11 mm and Z_2 = 6 mm from the liner cathode) and (b) laser shift interferogram of a multiwire liner at the 107th ns from the beginning of the discharge.

When processing the experimental data, the spectrum was divided into two intervals: 1.0–1.6 keV and 1.6–5.0 keV. The agar–agar surface density measured by the above method (ignoring the absorption in the tungsten plasma of the liner wires) is $\rho l_{AA} \approx 1900 \pm 220$ μg/cm^2, which is somewhat higher than the initial surface density of such a column. It follows from the optical streak images that the foam cylinder retains its initial size over the entire liner implosion. Therefore, the expected initial surface density of this column (provided that backlighting is performed along the diameter) should be $\rho l_{AA}^{in} \approx 1520 \pm 70$ μg/cm^2. The difference between the measured and initial agar–agar surface densities is related to the fact that, by the instant of backlighting, the tungsten plasma of the liner wires partially occupies the space between the agar–agar foam and the initial position of the wires. The corresponding surface density of the tungsten plasma is $\rho l_W \approx 80$–120 μg/cm^2. Taking into account the contribution of the tungsten plasma to the radiation absorption, we find that the surface density of agar–agar is $\sim 1600 \pm 220$ μg/cm^2. Thus, as was expected, the measured surface density of agar–agar coincides with its initial value within the experimental error.

6.3. Experiments with Load 3

In these experiments, a solid agar–agar foam cylinder was placed on the liner axis (Figs. 10a, 10b). The foam was filled with a micron-size tungsten powder. No special measures were undertaken to prevent the wire cores from falling within the viewing field of the pin diodes. Figure 11a shows the waveforms of the voltage across the interelectrode gap, the current within the region of radius r = 30 mm, the X-pinch emission power, and the power of SXR emission from the Z-pinch. It can be seen that the X-pinch burst occurs at the 98th ns after the beginning of the discharge, when the current through the liner reaches ≈1.3 MA.

The absorption coefficient of an X-pinch emission recorded behind an Al foil is ≈50% (Fig. 11b). The absorption coefficient recorded behind a Ti foil is ≈30%, whereas behind a Fe foil, it is less than the measurement error (<10%) (see Figs. 11c, 11d).

X-ray absorption recorded behind a Ti foil (see Fig. 11c) could be caused by

(i) the plasma of the wire cores residing at the liner periphery and partially falling into the viewing field of the detectors (the streak image in Fig. 11a shows that the outer boundary of the liner and, consequently, the cores themselves still remain at the initial wire positions),

(ii) the tungsten powder and the agar–agar foam itself ($\rho l_{AA} \approx 770$ μg/cm^2), and

(iii) the tungsten plasma of the liner wires (plasma precursor) existing at the moment in the axial region of the liner (as was shown above, this factor is negligibly small for photons with energies of >3 keV).

The agar–agar foam is almost transparent to photons with energies of >3 keV (the absorption coefficient is less than 10%). Hence, the absorption of X-pinch emission (≈30%) recorded behind a 20-μm Ti foil could not be caused by the absorption in the agar–agar foam.

Since no special measures were undertaken to prevent the wire cores from falling within the viewing field of the pin diodes, let us estimate the contribution of the wires to the absorption of X-pinch emission. By the instant of the X-pinch burst, the wire diameters increase threefold and become $d_s \approx 18$ μm [10]. The surface density of the wire core ($\rho l_s \approx 3900$ μg/cm^2) is sufficient for an almost complete (>90%) absorption of photons with energies of <5 keV. Thus, one can consider the cores of the evaporating wires (residing at their initial positions) to be a kind of a mesh on the probing beam path. There is possibility that one or two of the wire cores residing at the opposite ends of the wire array diameter will overlap (at least partially) the viewing field of one of three measuring pin diodes ($\Delta X' \approx 44$ μm).

In these experiments, the viewing field of the pin diodes behind a Ti foil was only partially overlapped by the wire cores, whereas behind a Fe foil, the viewing

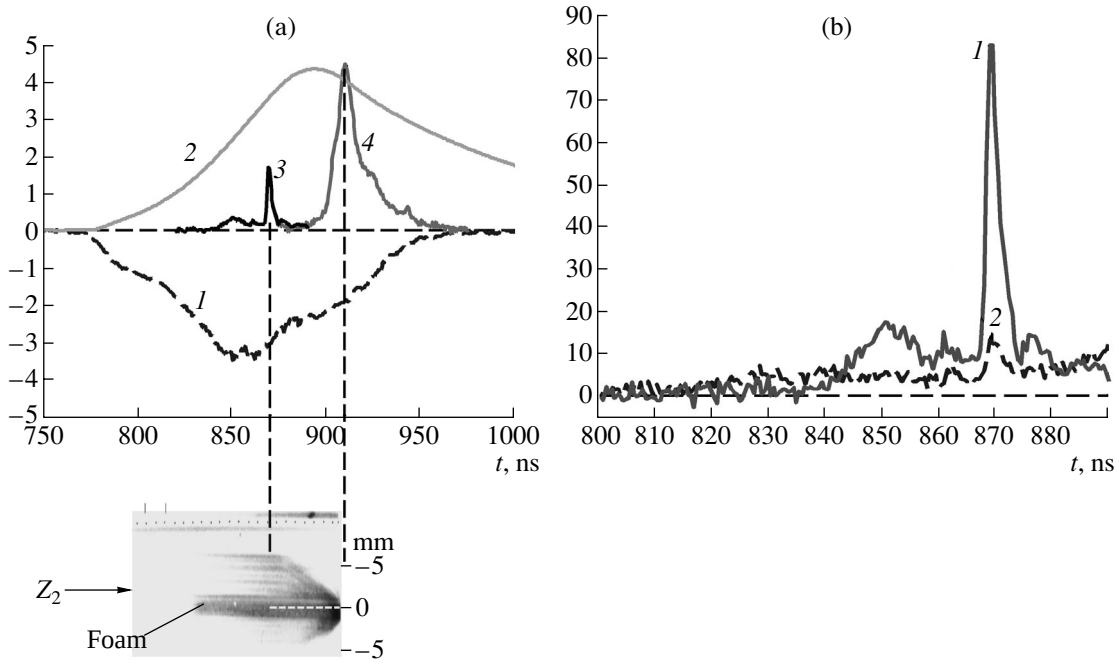

Fig. 13. Results of experiments with load 4: (a) waveforms of (*1*) the voltage across the interelectrode gap (in units of 100 kV), (*2*) the current within the region of radius $r = 30$ mm (in units of 0.4 MA), (*3*) the X-pinch emission power (in arb. units), and (*4*) the power of SXR emission from the Z-pinch (in TW) and (b) signals from the (*1*) reference and (*2*) measuring detectors (in arb. units) behind a 10-μm Al foil. Below plot (a), an optical streak image of the liner is shown (the image is synchronized with the above waveforms). The distance of the slit from the liner cathode is $Z_2 = 6$ mm (see Fig. 12a). The curves in plot (b) present the signals from the detectors U_i multiplied by $U_i r_i^2$, where r_i is the distance between the X-pinch and the *i*th detector ($i = 1, 2$).

field of the pin diodes was not overlapped at all and the detectors did not record radiation absorption.

Let us estimate the absorptivity of the tungsten powder ingrained in the agar–agar foam base, assuming that the grains (spheres with an average diameter of $d_{p0} \approx 6$ μm) uniformly occupy the entire volume of the foam column. The estimated number of the tungsten grains that fall into the viewing field of the detectors is

$$N_p^v = \frac{M_{pd}}{m_p}\frac{V_v}{V_{cl}} \approx 12.1,$$

where M_{pd} is the total powder mass; m_p is the mass of an individual grain; and V_v and V_{cl} are the volumes of the viewing field and the foam column, respectively. The absorptivity of the tungsten powder can then be estimated as

$$K_p^{\text{abs}} = N_p^v \frac{S_p}{S_v} \approx 0.22,$$

where $S_p = \pi(0.5d_{p0})^2$ is the cross-sectional area of a powder grain and $S_v = \pi(0.5\Delta X')^2$ is the area of the viewing field.

If the tungsten grains evaporate completely and tungsten uniformly occupies the entire volume of the agar-agar column ($\rho l_W \approx 1740$ μg/cm^2), then a detector behind an Al foil will record the ~99% absorption of X-pinch emission (for photon energies of 1–1.5 keV), a detector behind a Ti foil will record an ~75% absorption (for photon energies of 3–5 keV), and a detector behind a Fe foil will record an ~40% absorption (for photon energies of >5 keV). However, this was not the case in the experiments. This means that tungsten in the foam still remains in the form of grains.

The measured absorption coefficient of 1- to 1.5-keV X-ray emission in the agar–tungsten system (with allowance for the measurement errors) lies within the range $K_{\text{exp}}^{\text{abs}} \approx 0.71$–$0.81$ (Fig. 11b). The calculated absorption coefficient in this photon energy range is

$$K_{\text{calc}}^{\text{abs}} = K_{AA}^{\text{abs}} + (1 - K_{AA}^{\text{abs}})K_p^{\text{abs}} \approx (0.66\text{–}0.76),$$

where K_{AA}^{abs} is the absorption coefficient of the agar–agar foam and K_p^{abs} is the absorption coefficient of the tungsten powder. It can be seen that the calculated value agrees well with the measurement result.

The effective grain diameter corresponding to the maximum value of the measured absorption coefficient ($K_{\text{exp}}^{\text{abs}} \approx 0.81$) is $d_p \approx 7.7$ μm.

Thus, by the instant of the X-pinch burst, the fine tungsten powder in the foam still remains in the form of grains with an effective diameter of $d_p \approx (1\text{–}1.5)d_{p0}$.

6.4. Experiments with Load 4

In these experiments, the mass of the solid cylindrical foam column filled with a tungsten powder was increased by a factor of 2 as compared to the experiments with load 3. However, the specific density of the column was the same because of the corresponding increase in the column diameter. The mass composition of the column (agar–agar + tungsten) was also kept unchanged (see table). The agar–agar surface density was $\rho l_{AA} \approx 970$ μg/cm^2, which was higher by 20% than in the previous case. The arrangement of the foam column on the liner axis is shown in Fig. 12a.

Figure 13a shows the waveforms of the voltage across the interelectrode gap, the current within the region of radius r = 30 mm, the X-pinch emission power, and the power of SXR emission from the Z-pinch. It can be seen that the X-pinch burst occurs approximately at the same instant as in the previous case (at the 99th ns after the beginning of the discharge), when the current through the liner reaches ≈1.5 MA and the liner wires still reside at their initial positions (see the streak image in Fig. 13a and the laser shift interferogram in Fig. 12b).

The absorption coefficient of X-pinch emission recorded behind an Al foil is ≈85% (see Fig. 13b). The absorption coefficient behind Ti and Fe foils is less than the measurement error (<20%).

The number of tungsten grains within the viewing field of the detectors was approximately the same ($N_p^v \approx 10.1$) as in the experiments with load 3. Performing estimates similar to those described above, we find that the measured absorption coefficient of 1- to 1.5-keV X-ray emission in the agar–tungsten system (with allowance for the measurement errors) lies in the range $K_{\text{exp}}^{\text{abs}} \approx 0.79$–$0.83$. The calculated absorption coefficient in this photon energy range is $K_{\text{calc}}^{\text{abs}} \approx 0.70$–$0.81$.

In this case, the effective grain diameter corresponding to the maximum value of the measured absorption coefficient ($K_{\text{exp}}^{\text{abs}} \approx 0.83$) is $d_p \approx 6.8$ μm. Thus, tungsten is again in the form of grains and the absorption of X-ray emission in the photon energy range 1–1.5 keV is mainly related to the absorption by the agar–agar foam.

7. CONCLUSIONS

The results obtain can be formulated as follows:

At the 80th ns after the beginning of the discharge, the surface density of the tungsten wire plasma on the liner axis is less than 125 μg/cm^2. This fact confirms the results of previous experiments on the X-ray backlighting of the liner periphery at the same instant of discharge operation. According to those results, the bulk of the wire mass (up to 70%) is concentrated in dense cores, the rest being spread out toward the axis over a distance of ≈200 μm.

At the 100th ns, the fine tungsten powder ingrained in the foam still remains in the form of grains with an effective diameter of $d_p \approx (1$–$1.5)d_{p0}$, where $d_{p0} \approx 6$ μm is the initial average diameter of the grains.

ACKNOWLEDGMENTS

This study was supported by the Russian Foundation for Basic Research, project no. 01-02-17319.

REFERENCES

1. V. V. Aleksandrov, A. V. Branitskiĭ, G. S. Volkov, *et al.*, Fiz. Plazmy **27**, 99 (2001) [Plasma Phys. Rep. **27**, 89 (2001)].
2. S. V. Lebedev, F. N. Beg, S. A. Pikuz, *et al.*, Phys. Rev. Lett. **85**, 98 (2000).
3. G. S. Volkov, E. V. Grabovskiĭ, K. N. Mitrofanov, *et al.*, Preprint No. 0104A (Troitsk Institute for Innovation and Fusion Research, Troitsk, 2003).
4. S. V. Zakharov, V. P. Smirnov, and V. Ya. Tsarfin, in *Proceedings of the 14th International Conference on Plasma Physics and Controlled Nuclear Fusion Research, Wurzburg, 1992* (IAEA, Vienna, 1993), Vol. 3, p. 481.
5. R. H. Day and P. Lee, J. Appl. Phys. **52**, 6965 (1981).
6. I. Frolov, E. Grabovsky, K. Mitrofanov, *et al.*, in *Proceedings of the European Conference on Advanced Diagnostics for Magnetic and Inertial Fusion, Varenna, 2001*, Ed. by P. E. Stott, A. Wootton, *et al.* (Kluwer, New York, 2001), p. 257.
7. V. I. Derbilov, S. F. Medovshchikov, S. L. Nedoseev, *et al.*, Preprint No. 5157/7 (Kurchatov Institute of Atomic Energy, Moscow, 1990), p. 2.
8. S. F. Medovshchikov and S. L. Nedoseev, RF Patent No. 2075115 (1993).
9. A. E. Bugrov, I. N. Burdonskiĭ, V. V. Gavrilov, *et al.*, Zh. Éksp. Teor. Fiz. **111**, 903 (1997) [JETP **84**, 497 (1997)].
10. V. V. Alexandrov, M. V. Fedulov, I. N. Frolov, *et al.*, in *Proceedings of the 5th International Conference on Dense Z-Pinches, Albuquerque, 2002*; AIP Conf. Proc. **651**, 91 (2002).
11. A. V. Branitskiĭ and G. M. Oleĭnik, Prib. Tekh. Éksp., No. 4, 58 (2000).

Translated by N.N. Ustinovskiĭ